# THERMAL MODELING OF PHOTOVOLTAIC MODULES FOR RELIABILITY ASSESSMENT OF SINGLE-PHASE MODULE-INTEGRATED POWER ELECTRONICS IN TURKEY

A Thesis

by

MUHAMMED EMIN EKIN

Submitted to the Office of Graduate and Professional Studies of
Texas A&M University
in partial fulfillment of the requirements for the degree of

MASTER OF SCIENCE

| | |
|---|---|
| Chair of Committee, | Robert S. Balog |
| Committee Members, | Shankar P. Bhattacharyya |
| | Mehrdad Ehsani |
| | Ismail Capar |
| Head of Department, | Miroslav M. Begovic |

May 2018

Major Subject: Electrical Engineering

ABSTRACT

Renewable energy sources, especially those providing solar energy, are currently some of the fastest growing energy sources in the world. Both academia and the corporate world have invested in this technology to decrease the cost and increase the performance, efficiency, and reliability of photovoltaic (PV) modules. Though research is ongoing, there are certain meteorological parameters that affect the overall module temperature which may adversely impact the performance, efficiency, and reliability of the renewable energy system. Increases in temperature are responsible for many of the failures and degradations reported in PV modules. For many PV materials, like silicon-based PV cells which account for 90% of the current market, increasing the module temperature decreases the conversion efficiency, which decreases the amount of electrical energy produced. Thus, module temperature plays a crucial role in the overall photovoltaic energy conversion process. The datasheets for photovoltaic modules consider only a small range of operating conditions that are the standard test condition (STC) and the normal operating cell temperature (NOCT), despite the modules being required to function in an extensive range of conditions and variety of situations. Thus, accurately understanding PV module temperature via thermal modeling is essential to calculating module performance, efficiency, and reliability. In thermal modeling, environmental conditions affect electrical stresses and component thermal behavior, so reliable calculations are necessary to understand the operating points. In this regard, the broader impact of this research is to

model a methodology and tool by which users, researchers, and manufacturers can evaluate candidate PV technologies for power conversion, energy harvesting, and reliability determination. In the current research, this method has been applied to certain regions of Turkey. This avoided requiring expensive and time-consuming testbeds and long-term data logging. However, this improved methodology could be applied to other regions around the world.

DEDICATION

To my family

ACKNOWLEDGEMENTS

I would like to express my sincere gratitude to my advisor, Dr. Robert S. Balog, for the continuous support of my Master study and research, for his patience, motivation, enthusiasm, and immense knowledge.

I would like to thank my committee members, Dr. Shankar Bhattacharyya, Dr. Mehrdad Ehsani, Dr. Ismail Capar and, Dr.Behbood B. Zoghi for their advice and support throughout my master education.

I would also like to extend my appreciation to Dr. Bulent Akinoglu, Professor, Department of Physics in Center for Solar Energy Research and Application (GÜNAM), Middle East Technical University, for providing me his experience and knowledge about my research.

I am also indebted to my friends and colleagues at the REAPER laboratory for their support.

I would like to show my appreciation to the Department of Electrical and Computer Engineering to give me the opportunity to be an AGGIE, part of the well-organized program and provide me with many of the resources I acquired to complete my research.

Also, I would like to thank Turkish Ministry of National Education and Turkish Petroleum Corporation for their financial and emotional support during my master degree.

Last but not least, I would like to thank my parents, Husna Ekin and Abdulbaki Ekin, and my brothers Mustafa, Omer and his wife Deniz Didem and their daughter, my little friend Hayrunnisa. None of these accomplishments would have been possible without their sacrifices. They are the best family anyone could have wished for, and I dedicate this thesis to them.

## CONTRIBUTORS AND FUNDING SOURCES

This work was supervised by a thesis committee consisting of Professor Robert S. Balog of the Department of Electrical and Computer Engineering, Professor Bulent G. Akinoglu of the Department of Physics in Center for Solar Energy Research and Application (GUNAM), Middle East Technical University in Turkey, Professor Shankar P. Bhattacharyya, Professor Mehrdad Ehsani of the Department of Electrical and Computer Engineering, Professor Behbood Zoghi and Professor Ismail Capar of the Department of Engineering Technology and Industrial Distribution.

All work for the dissertation was completed independent by the student, under the advisement of Professor Robert S. Balog of the Department of Electrical and Computer Engineering and Professor Bulent G. Akinoglu of the Department of Physics in Center for Solar Energy Research and Application (GÜNAM), Middle East Technical University in Turkey.

There are no outside funding contributions to acknowledge related to the research and compilation of this document.

TABLE OF CONTENTS

Page

LIST OF FIGURES

Page

Page

LIST OF TABLES

Page

# 1. INTRODUCTION

## 1.1 Introduction

The demand for clean, low-cost, and sustainable energy sources has increased in recent years [1]. One of these energy sources is solar energy, which is transformed into electrical energy by PV modules. Because solar energy technology is growing rapidly, especially as compared to other energy sources, governments, many for-profit companies and academic institutions have made massive investments of time and money into solar energy projects. The Figure (1.1) shows the solar installed capacity by regions [2].

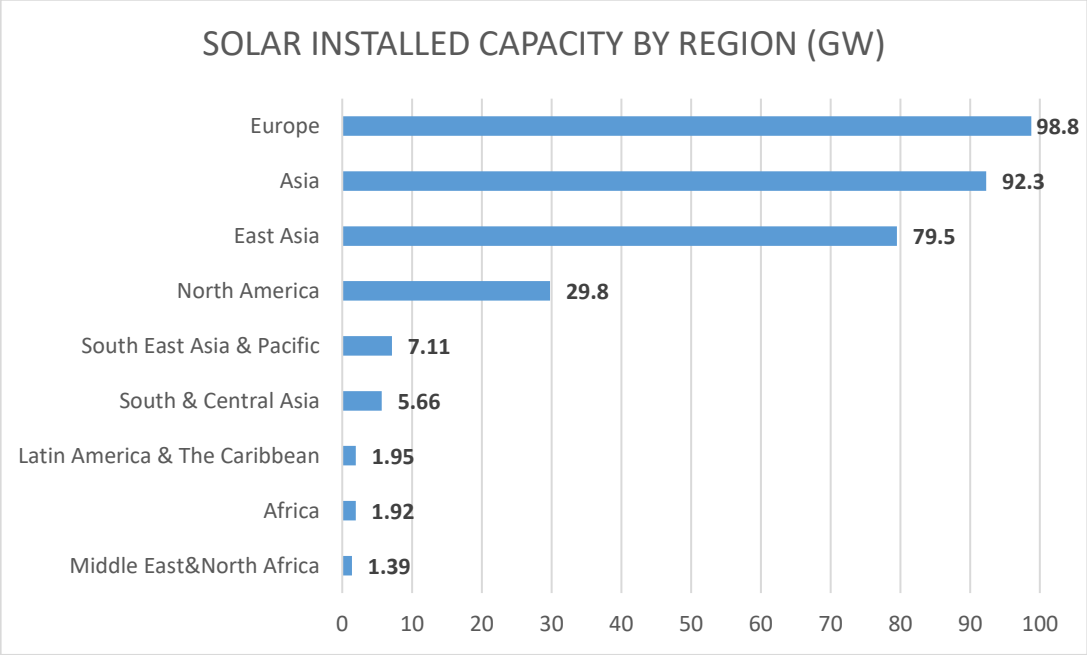


**Figure 1.1 Solar Installed Capacity by Region [2]**

Research and development (R&D) activities have focused on increasing efficiency and decreasing the costs associated with PV modules. Reliable thermal modeling is one of the most critical research aspects of PV modules specifically, and solar energy in general. To maximize the benefits obtainable from PV modules, accurately estimating PV module temperature is essential, since the PV module temperature and efficiency (i.e., generated power) are inversely proportional. At the same time, rising temperatures increase the likelihood of electrical failures. Hence, predicting and calculating PV module temperature through accurate thermal modeling is crucial to determining the reliability, safety, level of performance, stress distribution, and expected lifetime of the PV modules themselves, as well as whole system components. Correspondingly, PV module temperature also plays a significant role not only in voltage stress, but also in the amount of energy produced.

Because solar energy is a growing trend, sales of solar cells and PV modules around the world have increased in the last ten years [3]. However, many consumers are concerned with module lifetime and efficiency because both substantially affect the return on investment (ROI). Although the industry commonly gives customers 25 to 30 year electrical performance guarantees for the modules based on advanced tests, modules will not necessarily enjoy a constant level of efficiency. Also, the electrical performance warranty may not cover workmanship and materials if the module were completely fail. Additionally, the PV module energy production will decline every year at a degradation that depends on the specific module technology, such as silicon or cadmium telluride. A study by the National Renewable Energy Laboratory (NREL) found that PV module

energy production falls by 0.8% each year for all type of PV module, and 0.7% each year for silicon-based PV module only on average [4].

Moreover, though module manufacturers often offer lengthy guarantees, their estimates are frequently only accurate under specific test conditions, usually 25°C, and 1,000 W/m$^2$. For example, the working conditions of a PV module are written in the associated datasheet (e.g., 200,000 hours at 40°C). This estimation would be valid only at a constant operating temperature. The expected lifetime of the system and any of its components would decrease if the temperature grew to be higher than the standard test conditions, and increase if the temperature became lower [5]. As PV modules are expected to function over a wide range of temperatures and various levels of solar radiation (insolation), thermal modeling should be done to better understand module behaviors and critical operation limits in a spectrum of temperatures and solar radiation conditions. Consideration of the behaviors and limits (such as lifetime and safety lefel) of the entire PV system (i.e., the module, power electronics, and converter) should be consistently applied to all parts of the system; this will maximize both the life length and level of efficiency.

In this context, a thermal model was modeled to calculate PV module temperature, based on measured meteorological parameters, including: solar radiation (insolation), ambient temperature, wind speed, and dew point temperature. The measured meteorological parameters collected for this research are specific to different regions of Turkey. Although it is known that ambient temperature and solar irradiance have the most significant effects on PV module temperature, the above parameters were also used

in order to ensure more accurate results. The PV thermal model developed for the current research is valid for rooftop installations. As compared to conventional PV plants, the free installation offers certain advantages such as reducing residents electric bills and providing savings related to building costs. Despite certain advantages, though, the working temperature of roof-installed PV modules tends to be higher than conventional PV plants [6]. Since the working temperatures differ, so does the level of efficiency. In this research, the thermal model output allowed for the analysis of electrical and operating behaviors such as temperature limits and electrical stress levels, as well as the calculation of component reliability.

## 1.2 Literature Review

Many researchers have modeled thermal models of PV modules by considering energy balance equations that include convection, conduction, radiation heat transfer, and generated output power. In [7], the authors compared a number of proposed models. The Nominal Operating Cell Temperature (NOCT) approach and energy balance method were used in their models to calculate PV module temperature and electrical efficiency. The authors used solar irradiance, ambient temperature, and wind speed as environmental variables, and determined that the best model employed the energy balance method. In [6], the author determined the operating behavior of roof-installed PV modules. He conducted reverse ventilation analyses based on buoyancy forces and pressure loss mechanisms. Also, he made measurements by changing the distance between the roof and PV module, demonstrating that the effect of the distance between

the PV module and roof had a significant impact on operating conditions. However, if the distance was lower than 15 cm, no significant effect was found. Installation type was determined to be a critical parameter in the thermal calculations. In [8], the authors proposed mathematical and numerical models for PV cell steady-state temperatures in Egypt. They derived heat transfer equations by considering solar irradiation, convection, and radiation losses between the layers. In [1], the authors used energy balance equations and considered heat flow. They compared experimental and measured data, and found similar results. In [3], the researchers used an energy balance equation to theoretically calculate module temperature. The results showed that solar irradiance had more influence than other meteorological parameters on temperature. Moreover, the output temperature variation was higher on sunny days than on those that were cloudy. This demonstrated that sky cover was also a significant parameter for this type of model. Installation angle and ambient temperature were shown to be of secondary importance. In [9], the authors designed a thermal model using an energy balance equation. However, they did not take into consideration the actual wind speed because they did not have access to wind speed records. Finally, they compared different sky conditions. Their results showed their experimental and theoretical results to be very close in clear sky conditions. In [10], the authors conducted on energy analysis of silicon solar cells, which showed wind speed, solar irradiance, and ambient temperature to be the main factors in photovoltaic module temperature variations. The results specified that the PV module worked at a low level of efficiency as a result of the high temperature and solar irradiance levels at noon and in the afternoon. In [11], the authors created a dynamic thermal model

to predict PV module temperatures in variable climatic conditions. The results showed differences between the predicted and measured temperatures of 2°C, almost 80% of the time. In addition to module efficiency and temperature, environmental parameters also have a significant role in the electrical behavior of PV cells and the amount of electrical energy they generate. Since the output current and voltage of a PV module change with the level of solar radiation and cell temperature, thermal modeling output is crucial to understanding PV modules' behavior. In [7], the authors found that the output power decreased when the cell temperature increased at a rate of $0.401\%°C^{-1}$ and $0.563\%°C^{-1}$. They confirmed that these results agreed with the literature.

As can be seen from the above, there is a significant body of research on calculating PV module temperature and determining the effects of meteorological parameters.

## 1.3 Motivation for the Research

The motivation for this research is that Turkey has a significantly high solar energy potential, especially compared to other European countries (see Figure (1.2)) [12]. Turkey enjoys 2,737 hours of sunshine annually (7.5 hours per day), and 1,527 $kWh/m^2$ (4.2 $kWh/m^2$) of total incoming solar energy. A detailed map of Turkey, including some major cities, can be found in Figure (1.3) [13]. It shows the average annual sum amount of solar irradiation. Solar irradiation means energy delivered by the sun to the earth in the form of electromagnetic radiation. Although Turkey has more solar energy potential than any other European country, until 2016 it received little attention from the

authorities or solar energy companies. Although there was no installed photovoltaic capacity in 2006, this increased to 832.5 MW and 2,060 MW in 2016 and 2017, respectively [14]. Residential, commercial, and utility-scale photovoltaic investment has steadily increased; the goal is to reach 5 GW of installed capacity by the year 2023.

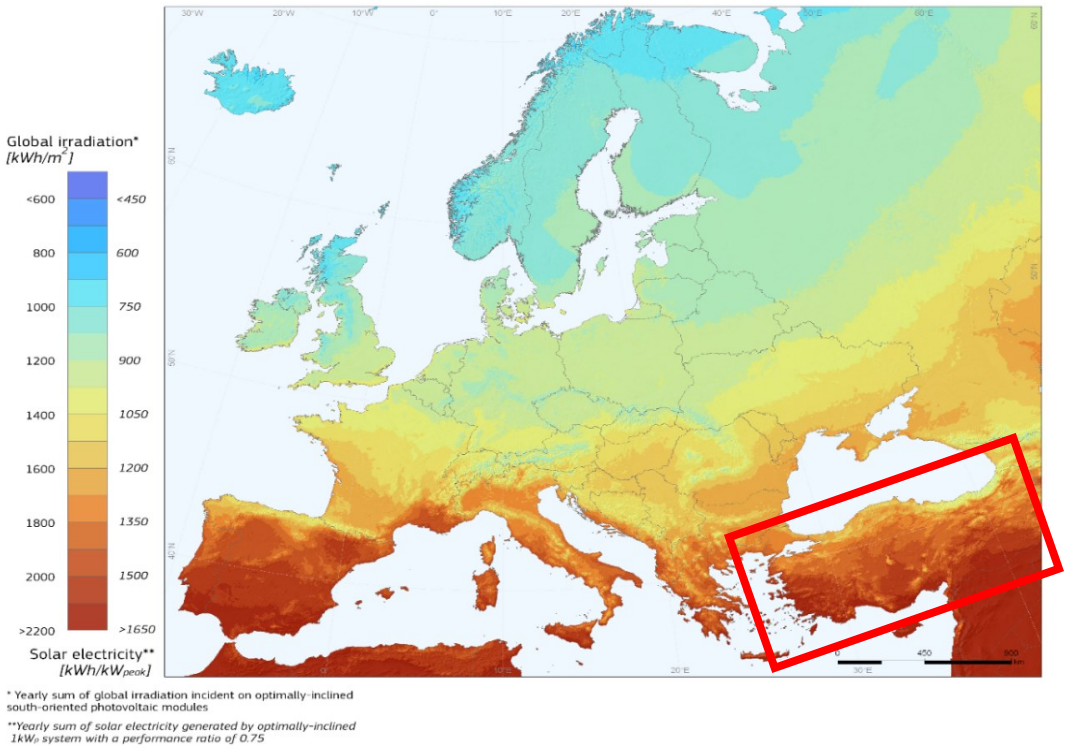


**Figure 1.2 Photovoltaic Solar Electricity Potential in European Countries, Reprinted from [12]**

Figure (1.3) shows a heat map of the direct normal insolation (DNI) for Turkey, overlaid with meteorological sites. The DNI means the quantity of received solar radiation on a

plane normal or perpendicular to the sun. The cities included span a diverse range of DNI levels. Moreover, there are a number of additional cities with similar annual DNI values in different climatic regions across Turkey as shown in Figure (1.4) [15].

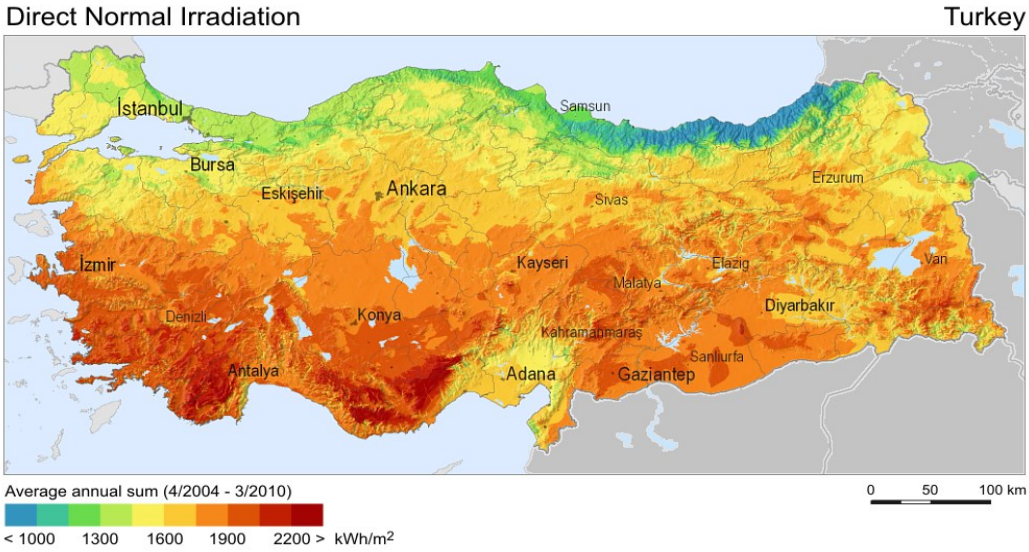


**Figure 1.3 Heat Map of Direct-Normal Insolation across Turkey, Reprinted from [13]**

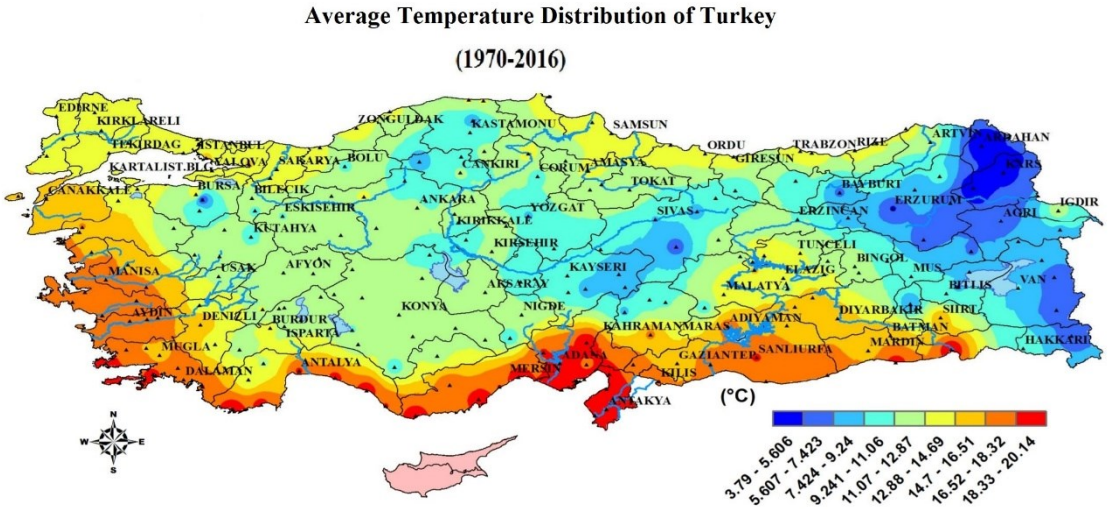


**Figure 1.4 Distribution of Annual Average Temperature between 1970 and 2016 in Turkey, Reprinted from [15]**

While comparing the Figure (1.3) and Figure (1.4), northeast of Turkey has moderate sun and cool temperature. It can be considered as a right place for solar installation, but this region is not flat land. Additionally, Konya is a flat area, relatively sunny and not too hot. Hence, Konya where the biggest solar plant of Turkey is establishing [16, 17] is a good choice to install multi-gigawatt projects. On the other hand, southeast of Turkey has good solar radiation. While this region has the harsh and cold climate, it receives most significant solar radiation in winter. The remarkable point of these two figures is that while Adana is at the same latitude with its surrounding cities, it has lower solar radiation and higher ambient temperature because of its low elevation and continentally.

## 1.4 Thesis Outline

This thesis research used thermal modeling to calculate PV module temperature and thermal modeling outputs in reliability calculations in order to determine the failure rate and mean time between failures (MTBF) of different candidate micro-inverter topologies. Additionally, this work calculated the minimum MTBF (i.e., the worst cases derived by maximum temperature), averaged MTBF (mean value of all ranges of MTBFs), and weighted MTBF (calculated by considering an operating point frequency). The outline of this thesis is as follows.

Chapter 2 offers details regarding thermal modeling and the use of thermal modeling equations in such models. Thermal models using total energy balance for the control volume are employed to help explain PV module behavior in response to certain meteorological parameters.

In Chapter 3, fundamental equations for photovoltaic cells that vary by temperature and solar radiation are given. Also, photon, diode, and saturation currents, and most importantly, output voltage, are all calculated for all operating points.

In Chapter 4, the reliability calculations for candidate micro-inverter topologies are described, based on the MIL 217 handbook [18]. Also, different inverter topologies are analyzed according to the placement of the capacitor and certain power decoupling techniques. Finally, MTBFs are calculated for each component; then, the whole-inverter failure rates are determined. The MTBF calculations are divided into three different categories: minimum MTBF, average MTBF, and weighted MTBF. Once the individual

component MTBFs are determined, the blameworthy components can also be found. The Figure (1.5) illustrates flowchart of this research process.

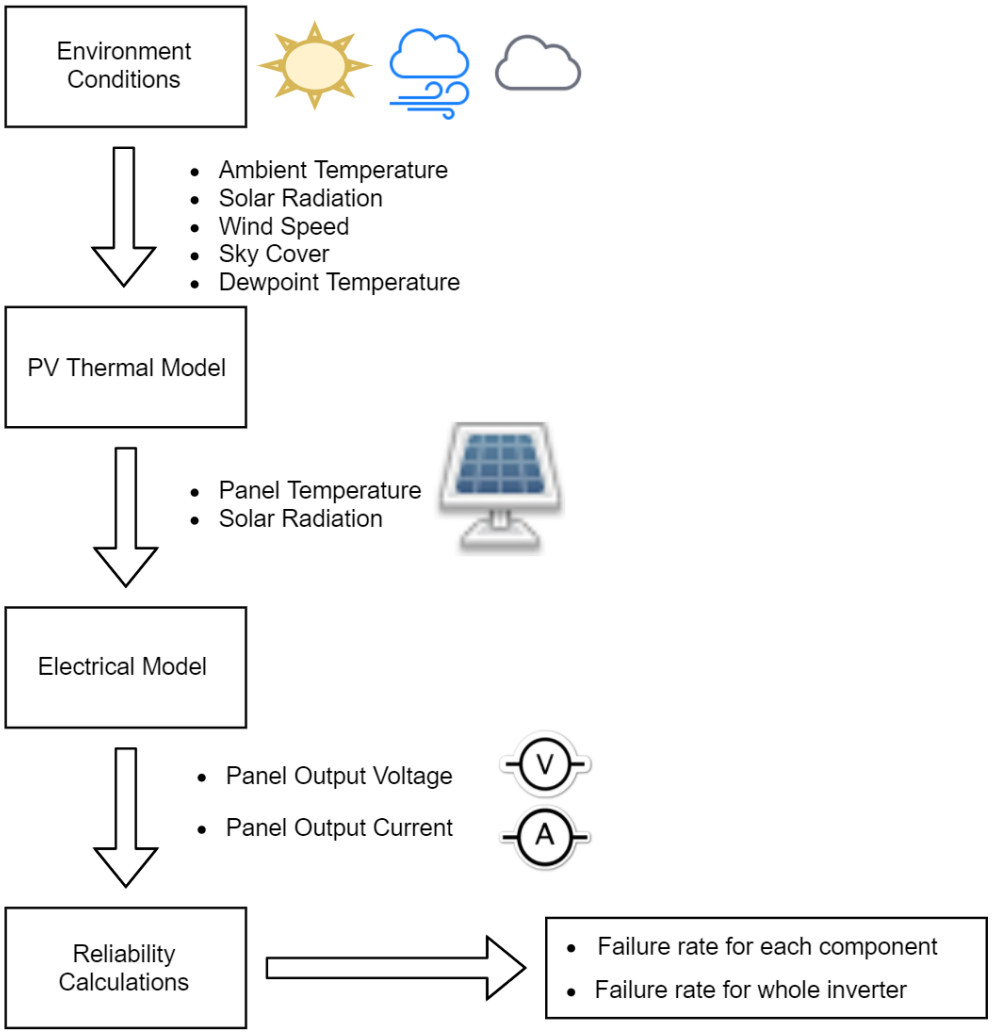


**Figure 1.5 Flowchart of the Process**

# 2. THERMAL MODELING OF PHOTOVOLTAIC MODULES

## 2.1 Introduction

As can be seen from the literature review, much research has been completed on the topic of thermal modeling. However, calculations of PV module temperatures should consider more meteorological parameters and the PV modules heat transfer. Because their thermal behavior and electrical performance can change with shifts in climatic conditions, climate variables (i.e., solar radiation, temperature of the surroundings, wind speed, sky cover, and dew point temperature) and certain heat transfer calculations should be taken into consideration; this will yield more accurate PV module temperatures. In addition, PV installation type affects module temperature. Wind direction can also be a factor, but the direction was neglected here to avoid computational complexity, since wind direction has less of an effect than wind speed [19].

The working principle of PV modules is that they absorb energy in the form of sunlight. As PV modules have a low rate of efficiency, only a small part (10%-15%) of absorbed sunlight can be converted into electricity; much of the remainder is converted into heat. The absorbed solar irradiance not transformed into electrical energy causes heat flow and temperature increases in the cells [7]. Consequently, the electrical efficiency decreases in response to the increasing module temperature.

The first goal of this study is to determine the effects of certain meteorological parameters on PV module temperature and electrical stress on the components. In this context, a thermal model was developed. The motivation for developing a model is to

create a tool to predict behavior and performance instead of relying on expensive and time-consuming field testbeds to log data. The models enable what-if scenarios to examine different options and designs. The thermal model was modeled by considering the equations described below.

## 2.2 Thermal Modeling Approach

PV module temperature is affected by the module physical characteristics (i.e., the material), weather conditions, surrounding environment, and installation type (i.e., position and angle) [11]. The method of thermal energy exchange with the module surroundings can be used to calculate the module temperature. Environmental effects cause a thermal energy exchange with the heat transfer mechanism. The structure of the thermal model employed in this research is based on total energy equality [11, 20]. In the modeling approach used herein, the thermal model embraces the PV module as a total energy equilibrium. Since the energy equilibrium approach takes into consideration more parameters than the standard method of calculation, it is more suitable and produces more accurate results [21]. The main rule is that the absorbed energy is equal to the sum of the energy loss and converted energy (i.e., the output power) [21]. Solar insolation, the electrical transformation ratio, and longwave radiative transfer with the rooftop, earth, and sky all play vital roles as meteorological parameters, and are used here to calculate the PV module temperature [20]. The structure of the thermal model can be found in equation (2.1).

$$\frac{dT_s}{dt} = \frac{q_{ef}\ A\ -\ P_{out}\ -\ \left(q_{lw}\ +\ q_{cond}\ +\ q_{conv}\right) A}{c_{\mathrm{mod}}\ A} \tag{2.1}$$

$$\begin{cases} q_{ef}, & \text{Effective Incident Radiation } \left[W/m^2\right] \\ P_{out}, & \text{Output Power } [W] \\ q_{lw}, & \text{Longwave Radiation Loss } \left[W/m^2\right] \\ q_{cond}, & \text{Conductive Heat Loss} \left[W/m^2\right] \\ q_{conv}, & \text{Convective Heat Loss} \left[W/m^2\right] \\ c_{\mathrm{mod}}, & \text{Heat Capacity} \left[J/m^2 K\right] \\ A, & \text{Module Area} \left[m^2\right] \\ T_s, & \text{Module Surface Temperature} \left[^{\circ}C\right] \end{cases}$$

The variable $q_{ef}$ is the effective solar radiation (insolation) reaching the front face of the PV module. The effective incoming solar radiation is a part of solar radiance (G) and PV module absorptivity (α). It is calculated as in equation (2.2) [9, 22].

$$q_{ef} = \alpha\ G \tag{2.2}$$

The total heat flux for the module has three main parts: longwave radiation, conductive heat, and convection heat losses.

$$q_{loss} = q_{lw} + q_{cond} + q_{conv} \tag{2.3}$$

Additionally, convection heat loss is defined as the sum of the forced and free convective heat losses. Hence, the equation for total heat flux for the module is written as in equation (2.4) [20].

$$q_{loss} = q_{lw} + q_{cond} + q_{convfree} + q_{convforced} \tag{2.4}$$

$$\begin{cases} q_{convfree}, & \text{free convection heat loss} \left[ W/m^2 \right] \\ q_{convforced}, & \text{forced convection heat loss} \left[ W/m^2 \right] \end{cases}$$

### 2.2.1 Heat Transfer

Solar radiation is absorbed or transformed by solar cells. The generated electrical power changes in response to the amount of absorbed solar radiation and the PV module operating temperature, both of which affect efficiency. The absorbed energy has two parts. One is converted to electrical power, and the remainder generates heat by definition, heat is a flow of thermal energy. The thermal energy is rejected by the PV module into the environment by way of three types of heat losses: radiation, conduction, and convection. In other words, the PV module exchanges thermal energy with its environment in the form of the above-mentioned heat transfers [1].

In this research, heat transfer equations for a module and the environment were theoretically modeled and the heat losses were calculated. The heat transfer directions to and from the module are as shown in Figure (2.1).

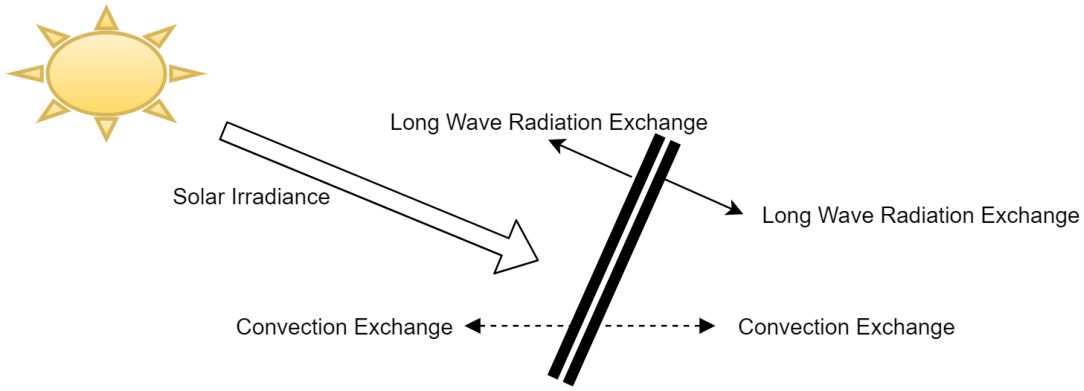


**Figure 2.1 Directions of Heat Transfer**

#### 2.2.1.1 Longwave Radiation

Longwave radiation describes the heat exchanged between the PV module and the surrounding environment. The Stefan-Boltzmann law calculates the longwave energy emission for a per unit area of a surface at a specific temperature [22]. It is given below.

$$q_{lw} = A\ \sigma\ \varepsilon\ T^4 \tag{2.5}$$

When longwave radiation is calculated for residential PV module installations, it is necessary to consider sky, ground, roof, and PV module factors. Hence, the rate of longwave radiation for residential installation is derived from the following equation, according to the Stefan-Boltzmann law [3, 23].

$$q_{lw\_top} = \sigma \varepsilon_g F_{mst}\left(T_s^4 - T_{sky}^4\right) + \sigma \varepsilon_g F_{me}\left(T_s^4 - T_{earth}^4\right) \quad (2.6)$$

$$q_{lw\_bottom} = \sigma \varepsilon_b F_{msb}\left(T_s^4 - T_{sky}^4\right) + \sigma \varepsilon_b F_{mr}\left(T_s^4 - T_{roof}^4\right) \quad (2.7)$$

$$q_{lw} = q_{lw\_bottom} + q_{lw\_top} \quad (2.8)$$

In the above equations, σ symbolizes the Stefan-Boltzmann constant for radiative heat transfer ($5.67 * 10^8$ W/ ($m^2 * K^4$)). The absorptive capacity or emissivity of the module upper and back surfaces are indicated as $\varepsilon_g$ and $\varepsilon_b$, respectively. The variable $\varepsilon_b$ was considered equal to $\varepsilon_g$ [20]. Emissivity provides information about the absorption properties of a material. For example, a black body has a maximum emissivity value of 1, and a white body that has perfect reflector characteristics has a minimum emissivity of 0. The emissivity value is typically between 0.9 and 1.0 for PV modules [20]. The variables $F_{mst}$, $F_{me}$, $F_{msb}$, and $F_{mr}$ are view factors from top-to-sky, top-to-earth, bottom-to-sky, and bottom-to-roof, respectively. The variable β is the tilt angle of the PV module (see Figure (2.2)); it should be $0 \le \beta \le \pi$. The view factor parameters are derived based on the tilt angle as follows.

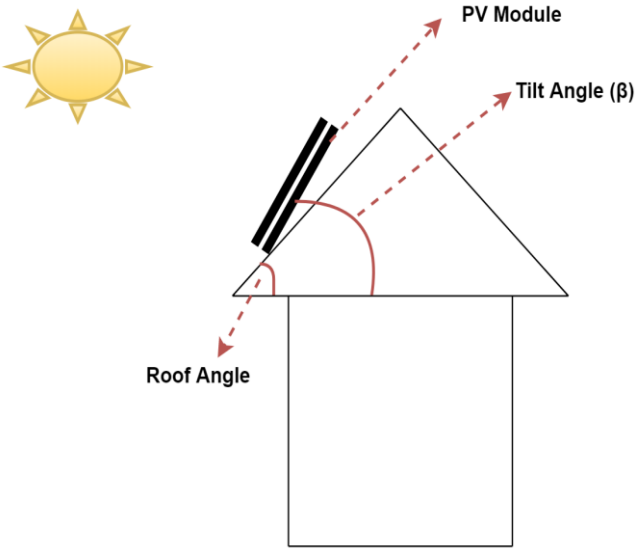


**Figure 2.2 Roof and Tilt Angle Demonstration**

$$F_{mst} = \frac{1}{2}\left(1+\cos(\beta)\right) \tag{2.9}$$

$$F_{me} = \frac{1}{2}\left(1-\cos(\beta)\right) \tag{2.10}$$

$$F_{msb} = \frac{1}{2}\left(1+\cos(\pi-\beta)\right) \tag{2.11}$$

$$F_{mr} = \frac{1}{2}\left(1-\cos(\pi-\beta)\right) \tag{2.12}$$

In equations (2.6-2.8), $T_s$ is the surface temperature of the module in °C, and $T_{earth}$ is the ground temperature in °C. In my thesis, it was considered the earth surface temperature, $T_{earth}$, to be equal to the ambient temperature, $T_{ambient}$, but the model is general enough to include an earth temperature model, if needed in the future. The values for $T_{ambient}$ were

taken from the Turkish State Meteorological Service database [15, 24], hourly. Moreover, although knowing the roof temperature is essential to calculating the overall longwave radiation losses, no exact calculations are possible because they are related to building type, roof structure, roof material, the warming rate of that material, ambient temperature, and the solar heating coefficient. Thus, in this research, roof temperature was assumed to be equal to the ambient temperature. On the other hand, although $T_{sky}$ has in some studies been considered equal to the ambient temperature [25], calculating it without making any assumptions yield more accurate results. In this research, it was calculated as a function of ambient temperature, as in [26, 27].

$$T_{sky} = (\varepsilon_{sky}(T_{ambient})^4)^{0.25} \tag{2.13}$$

In equation (2.13), the emissivity of the sky, $\varepsilon_{sky}$, is related to the dew point temperature, which changes depending on if it is daytime or nighttime. Thus, two equations, one each for daytime and nighttime, are derived based on the dew point temperature [20, 21].

$$\varepsilon_{sky} = \begin{cases} 0.727 + 0.0060 \cdot T_{dew}, & \text{during daytime} \\ 0.741 + 0.0062 \cdot T_{dew}, & \text{during nighttime} \end{cases} \tag{2.14}$$

where $T_{dew}$ is in °C, while $T_{sky}$ and $T_{ambient}$ are in Kelvin, [K].

The following equations are used to calculate the conductive and convective heat losses of the PV module. Finally, the heat transfer solution is obtained numerically.

#### 2.2.1.2 Conductive Heat Losses

Temperature differences between the PV module and other materials in contact with the PV module result in conductive heat losses. In this study, conductive heat losses were neglected; the small contact area of the frame and large surface PV module means that the contact area is tiny [3, 9, and 20].

$$q_{cond} = 0 \tag{2.15}$$

#### 2.2.1.3 Convective Heat Losses

Contact between the PV module surface and the air causes convective heat losses. Ambient temperature and wind speed are the origins of these losses. Convective losses are comprised of two parts: those resulting from free (i.e., the natural buoyancy of hot air) convection and those resulting from forced (i.e., wind speed) convection [20]. Convection losses are defined according to Newton's law of cooling, which states that convection losses are commensurate with the temperature difference between the fluid and the PV module surface [3, 28]. The general equation for convective heat transfer is as follows.

$$q_{conv} = h_{conv}\left(T_s - T_{ambient}\right) \tag{2.16}$$

In most research, only the dominant convection type is calculated, and others are neglected. However, in this study, although one may make only a small contribution to heat transfer, both free and forced convection transfer were calculated to obtain more accurate results. The coefficients of free and forced convection greatly affect temperature prediction. Thus, free and forced convection heat transfer calculations are necessary to find $h_{conv}$. The following subsections explain determining the convection heat transfer parameters.

#### 2.2.1.3.1 Free Convection Heat Losses

The free convection heat losses are calculated using equation (2.17-2.18). As heat transfer was assumed to be equal for the bottom and top surfaces, the equation was multiplied by two to find the total free convection heat loss like in equation (2.19). However, it was considered that PV module is placed flush mounted namely there is no air gap between module and roof, so 2 factor was eliminated [20].

$$q_{convfree,total} = q_{convfree,top} + q_{convfree,bottom} \tag{2.17}$$

$$q_{convfree,total} = h_{free,top} T_{diff} + h_{free,bottom} T_{diff} \tag{2.18}$$

$$q_{conv,free} = 2\, h_{free}\, T_{diff} \tag{2.19}$$

The free convection heat transfer coefficient is as indicated below.

$$h_{free} = \frac{N_{UL,\,free}\ k}{L} \tag{2.20}$$

As the PV module is considered to be a plate, the Nusselt number ($N_{UL}$) is calculated using equation (2.21) [20, 21, and 22].

$$N_{UL,free} = 0.68 + 0.67 \left( Ra_L \left( 1 + \left( \frac{0.492}{\mathrm{Pr}} \right)^{\frac{9}{16}} \right)^{\frac{-16}{9}} \right)^{0.25} \tag{2.21}$$

Since $\mathrm{Ra_L} = \mathrm{Gr_L} * \mathrm{Pr}$, the Grasshof and Prandtl numbers are needed to calculate the Rayleigh number. The Grasshof number has been defined as the proportion of buoyancy (i.e., lifting force) to viscous force (i.e., frictional force) acting on a fluid. The Prandtl number describes the ratio of the momentum diffusivity (i.e., diffusion) to the thermal diffusivity. Both are dimensionless numbers. The Grasshof number is calculated by using the standard definition.

$$Gr_L = \frac{9.81 \cos(\alpha)\, T_{diff}\, L^3}{\eta^2\, T_{avg}} \tag{2.22}$$

where α is the angle between the vertical surface and PV module, and $T_{diff}$ is the temperature difference between the PV module temperature and the ambient temperature. Average temperature, characteristic length, and temperature differences are determined by equation (2.23-2.25)

$$T_{avg} = \frac{T_s + T_{ambient}}{2} \tag{2.23}$$

$$L = \frac{A}{2(H + W)} \tag{2.24}$$

where H is the height, and W is the width of the PV module.

$$T_{diff} = T_s - T_{ambient} \tag{2.25}$$

The η (kinematic viscosity), k (thermal conductivity), and Prandtl number were curve-fitted by interpolating the air properties in Table (2.1) [29]. The derived equations depended on the ambient temperature.

**Table 2.1 Air Properties [29]**

| Temp. (°C) | Density ρ,kg/m$^3$ | Specific Heat $c_p$, J/kg.K | Thermal Conductivity k, W/m.K | Thermal Diffusivity α, m$^2$/s | Dynamic Viscosity μ, kg/m.s | Kinematic Viscosity η, m$^2$/s | Prandtl Number Pr |
|---|---|---|---|---|---|---|---|
| **-20** | 1.394 | 1005 | 0.02211 | $1.578x10^{-5}$ | $1.630x10^{-5}$ | $1.169x10^{-5}$ | 0.7408 |
| **-10** | 1.341 | 1006 | 0.02288 | $1.696x10^{-5}$ | $1.680x10^{-5}$ | $1.252x10^{-5}$ | 0.7387 |
| **0** | 1.292 | 1006 | 0.02364 | $1.818x10^{-5}$ | $1.729x10^{-5}$ | $1.338x10^{-5}$ | 0.7362 |
| **5** | 1.269 | 1006 | 0.02401 | $1.880x10^{-5}$ | $1.754x10^{-5}$ | $1.382x10^{-5}$ | 0.7350 |
| **10** | 1.246 | 1006 | 0.02439 | $1.944x10^{-5}$ | $1.778x10^{-5}$ | $1.426x10^{-5}$ | 0.7336 |
| **15** | 1.225 | 1007 | 0.02476 | $2.009x10^{-5}$ | $1.802x10^{-5}$ | $1.470x10^{-5}$ | 0.7323 |
| **20** | 1.204 | 1007 | 0.02514 | $2.074x10^{-5}$ | $1.825x10^{-5}$ | $1.516x10^{-5}$ | 0.7309 |
| **25** | 1.184 | 1007 | 0.02551 | $2.141x10^{-5}$ | $1.849x10^{-5}$ | $1.562x10^{-5}$ | 0.7296 |
| **30** | 1.164 | 1007 | 0.02588 | $2.208x10^{-5}$ | $1.872x10^{-5}$ | $1.608x10^{-5}$ | 0.7282 |
| **35** | 1.145 | 1007 | 0.02625 | $2.277x10^{-5}$ | $1.895x10^{-5}$ | $1.655x10^{-5}$ | 0.7268 |
| **40** | 1.127 | 1007 | 0.02662 | $2.346x10^{-5}$ | $1.918x10^{-5}$ | $1.702x10^{-5}$ | 0.7255 |
| **45** | 1.109 | 1007 | 0.02699 | $2.416x10^{-5}$ | $1.941x10^{-5}$ | $1.750x10^{-5}$ | 0.7241 |
| **50** | 1.092 | 1007 | 0.02735 | $2.487x10^{-5}$ | $1.963x10^{-5}$ | $1.798x10^{-5}$ | 0.7228 |
| **60** | 1.059 | 1007 | 0.02808 | $2.632x10^{-5}$ | $2.008x10^{-5}$ | $1.896x10^{-5}$ | 0.7202 |
| **70** | 1.028 | 1007 | 0.02881 | $2.780x10^{-5}$ | $2.052x10^{-5}$ | $1.995x10^{-5}$ | 0.7117 |
| **80** | 0.9994 | 1008 | 0.02953 | $2.931x10^{-5}$ | $2.096x10^{-5}$ | $2.097x10^{-5}$ | 0.7154 |
| **90** | 0.9718 | 1008 | 0.03024 | $3.086x10^{-5}$ | $2.139x10^{-5}$ | $2.201x10^{-5}$ | 0.7132 |
| **100** | 0.9458 | 1009 | 0.03095 | $3.243x10^{-5}$ | $2.181x10^{-5}$ | $2.306x10^{-5}$ | 0.7111 |

The Figure (2.3) and (2.4) show the curve-fitting for kinematic viscosity and conductivity respectively.

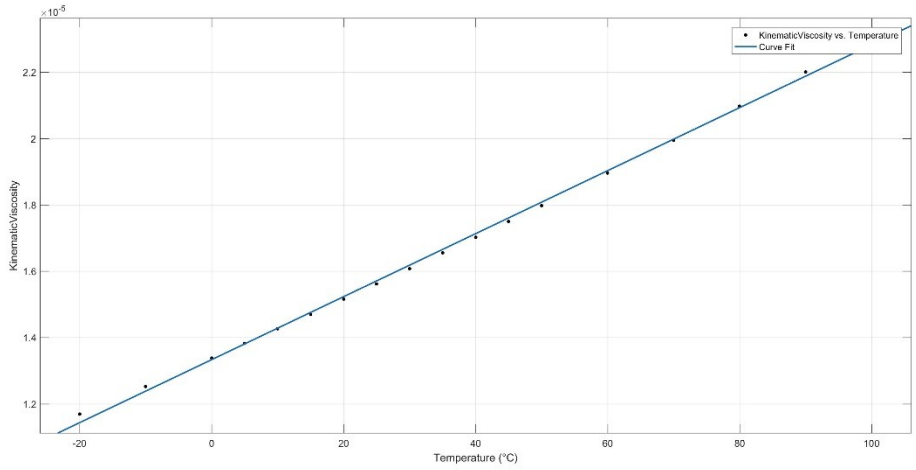


**Figure 2.3 Curve-Fitting for Kinematic Viscosity**

$$\eta = 1.333*10^{-5} + 9.469*10^{-8} * T_{avg} \quad (2.26)$$

R-square value for obtained kinematic viscosity curve is 0.9987.

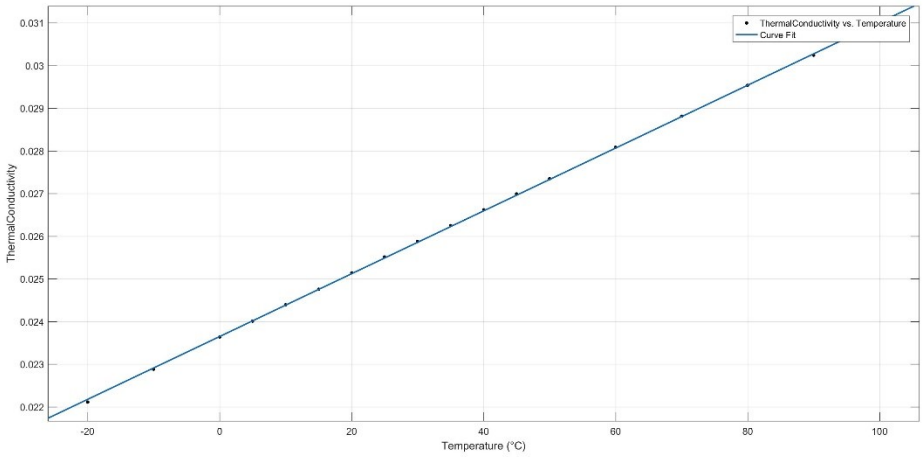


**Figure 2.4 Curve-Fitting for Thermal Conductivity**

$$k=0.02365+7.361*10^{-5}* T_{avg} \quad (2.27)$$

R-square value for obtained thermal conductivity curve is 0.9999.

The Figure (2.5) shows the curve-fitting for Prandtl Number.

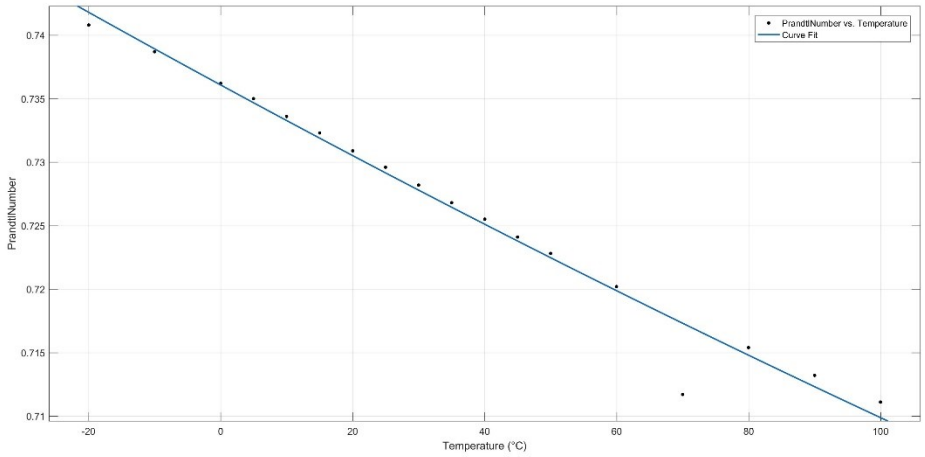


**Figure 2.5 Curve-Fitting for Prandtl Number**

$$Pr=0.7361-0.0002822* T_{avg}+2.012*10^{-7}* T_{avg}^{2} \quad (2.28)$$

R-square value for obtained Prandtl Number curve is 0.9747.

#### 2.2.1.3.2 Forced Convection Heat Losses

Since the PV module is a square plate, the forced heat transfer coefficient for the bottom of the PV module could be found using equation (2.29) [10, 20]. Heat transfer

for the bottom and top surfaces were assumed to be equal, but 2 factor was eliminated as was the case for free convection.

$$q_{conv,\,forced} = h_{forced} T_{diff} \tag{2.29}$$

The forced heat transfer coefficient is found by using wind speed, kinematic viscosity (η), the Prandtl number (Pr), characteristic length (L) of the PV module, specific heat ($c_p$), and density (ρ) [20].

$$h_{forced} = \frac{(c_p \rho) 0.931 \left( \frac{wind * \eta}{L} \right)^{0.5}}{\Pr^{\frac{2}{3}}} \tag{2.30}$$

The kinematic viscosity (η) and Prandtl number (Pr) were derived using a MATLAB curve-fitting when calculating the free convection heat transfer. An equation for ($c_p$ ρ) was developed in the same way. The Figure (2.6) shows the curve-fitting for ($c_p$ ρ). Wind speed was taken from the Turkish State Meteorological Service database [15, 24], hourly.

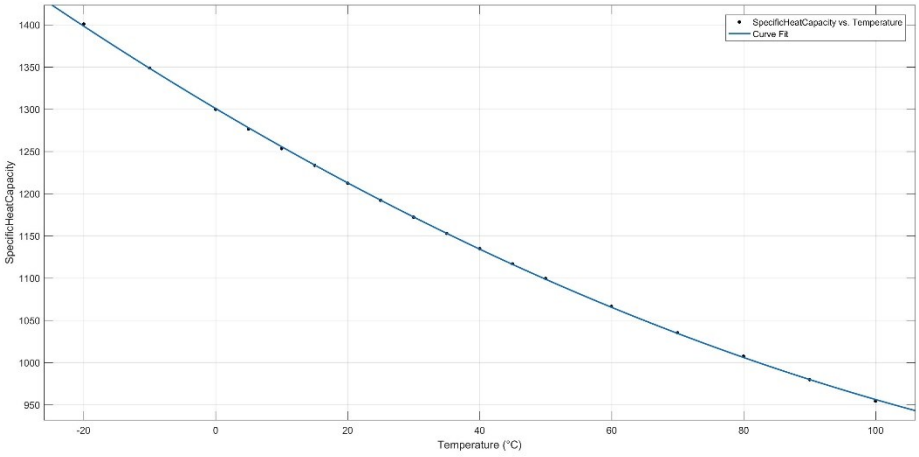


**Figure 2.6 Curve-Fitting for ($c_p$ ρ)**

$$c_p \rho = 1301 - 4.642 * |T_{avg}| + 0.01194 * T_{avg}^2 \quad (2.31)$$

R-square value for obtained kinematic viscosity curve is 0.9999.

Finally, the sum of the forced and free convection heat losses are combined to obtain the total convection heat loss.

$$q_{conv} = q_{conv,\,free} + q_{conv,\,forced} \quad (2.32)$$

### 2.2.2 PV Module Heat Capacity

The heat capacity of a PV module describes the quantity of energy needed by the module to increase its temperature. Since the PV module in this research has multiple laminate layers, the quantity is a combination of the heat capacities of the layers of laminate [20].

$$c_{\text{mod}} = \sum_{m}^{N} A d_m \ \rho_m c_m, \ \text{ for } n = 1...N \text{ layers} \tag{2.33}$$

$$\begin{cases} d_m, & \text{tickness of the m}^{th} \text{ layer } [m] \\ \rho_m, & \text{density of the m}^{th} \text{ layer} \left[ kg/m3 \right] \\ c_m, & \text{specific heat capacity of the m}^{th} \text{ layer} \left[ J/kg-K \right] \\ A, & \text{Module Area} \left[ m^2 \right] \end{cases}$$

Table (2.2) gives typical values for a PV laminate with material properties [20]. In this study, a silicon-based PV module was used and a $c_{mod}$ parameter was employed from the PV module datasheet.

**Table 2.2 PV Material Properties [20]**

| PV Module Element | Density ρ [kg/m$^3$] | Specific Heat c [J/kg-K] | Thickness of Layer d [m] | $d_m$*ρ*c [J/m$^2$K] | $d_m$*ρ*c [WH/m$^2$K] |
|---|---|---|---|---|---|
| **PV cells (Silicon)** | 2330 | 677 | 0.0003 | 473 | 0.13 |
| **Polyester (Tedlar Trilaminate)** | 1200 | 1250 | 0.0005 | 750 | 0.21 |
| **Glass** | 3000 | 500 | 0.003 | 4500 | 1.25 |
| **TOTAL** | | | | **5723** | **1.59** |

### 2.2.3 PV Module Electrical Power

A thermal model can provide assistance with determining the random electrical transformation efficiency of incoming shortwave radiation [20]. The electrical transformation efficiencies for commercial PV modules are approximately 10% to 14%. This was considered to be a constant value in this research. The electrical output power generated by the PV module is calculated as below [30].

$$P_{out} = E * A = \left( G\delta \left[ 1 - T_{coefficient} \left( T_S - 25 \right) \right] \right) * A \tag{2.34}$$

where E is the electrical power ($W/m^2$), A is the module area, δ is the electrical efficiency at a standard condition (25°C and 1,000 $W/m^2$), and $T_{coefficient}$ is the temperature coefficient for the output power.

## 2.3 Application

The theoretical model was developed based on the meteorological parameters, heat transfer, and energy balance equation. The final equation (2.35) is a nonlinear and time-varying ordinary differential equation (ODE) with regards to module temperature, $T_s$. For calculations with large numbers, the Euler method is both suitable and straightforward [3]. The differential equation for module temperature, which varies with the meteorological parameters, was solved numerically by using the Euler method in Matlab for each operating point.

$$\frac{dT_s}{dt} = \frac{q_{ef} A - P_{out} - \left(q_{lw} + q_{cond} + q_{conv}\right) A}{c_{\text{mod}} A} \tag{2.35}$$

Figure (2.7) includes a flowchart of the thermal modeling simulation. The input into the model is hourly solar insolation and other meteorological data collected from the Turkish State Meteorological Service. Although solar insolation values can vary between 0 and 1,000 W/m$^2$, a minimum insolation level is needed to generate sufficient electrical power. In [5], the measurements showed that 10 to 15 W/m$^2$ of solar irradiation is sufficient to begin generating power from a 100 W PV module. Because a 265 W PV module was used in this study, 50 W/m$^2$ solar irradiation (almost 5% of the 1,000 W/m$^2$ that would be full solar irradiation) was needed to generate sufficient electrical energy.

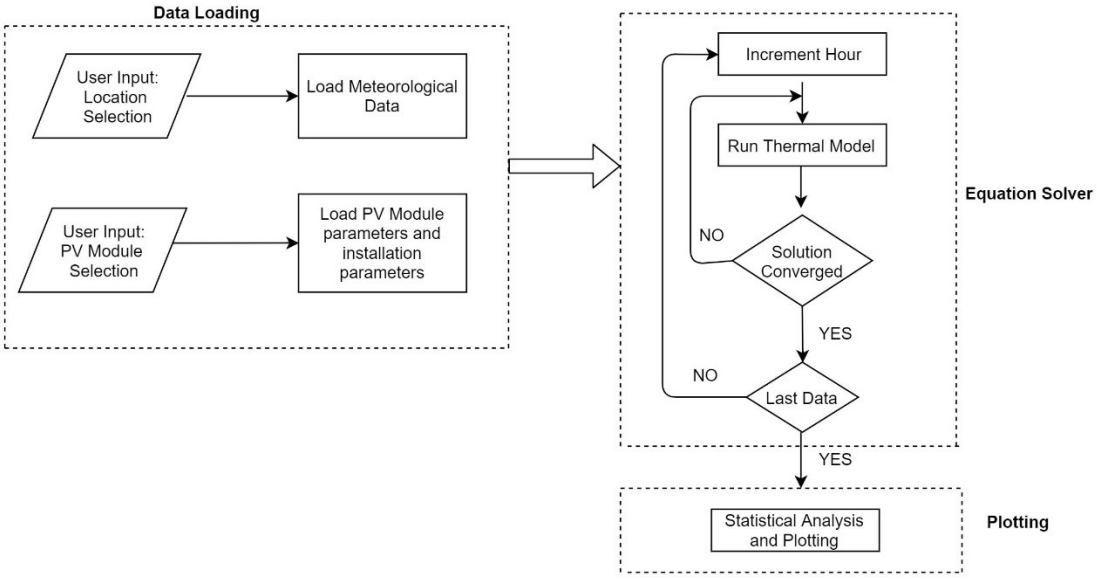


**Figure 2.7 Workflow of the Thermal Modeling Simulation**

## 2.4 Results

PV module output temperature was calculated for Ankara, which is located in the middle of Turkey. The latitude and longitude of Ankara are 39°55' north and 32°51' east, respectively. Figures (2.8) and (2.9) show the global radiation and sunshine duration for Ankara and overall Turkey [31]. The Figures below illustrate that Ankara shares a similar solar characteristic with overall Turkey based on the geography. In other words, Ankara represent average region in Turkey. Hence, although the research methodology could be applied to all cities in Turkey, figures of the model results demonstrate specifically to Ankara. Additionally, thermal and electrical model outputs for the other cities can be found at the Appendix.

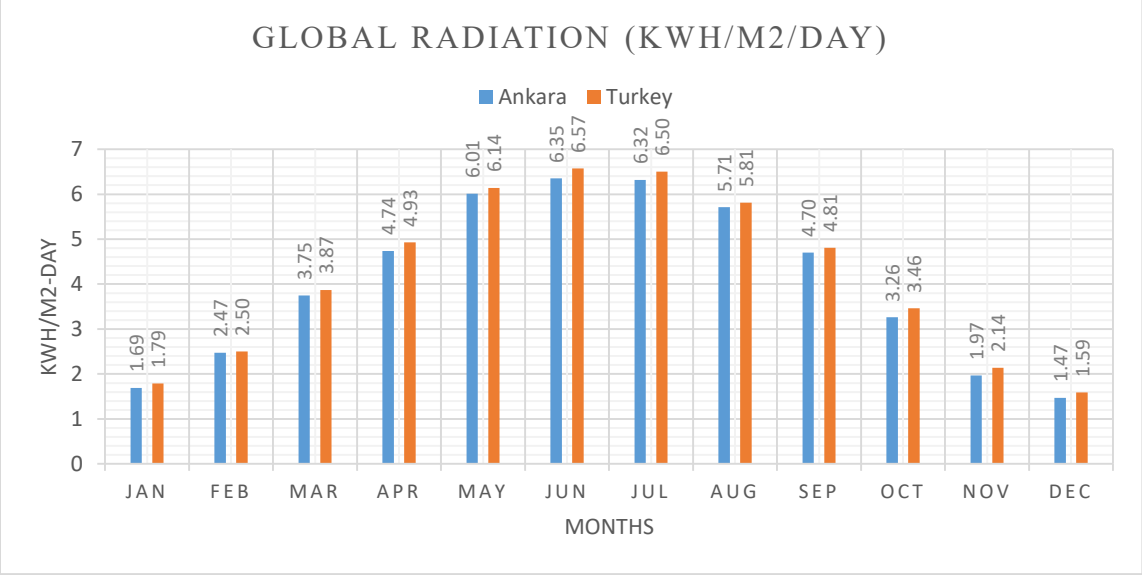


**Figure 2.8 Comparison of Mean Global Radiation for Ankara and Turkey Average**

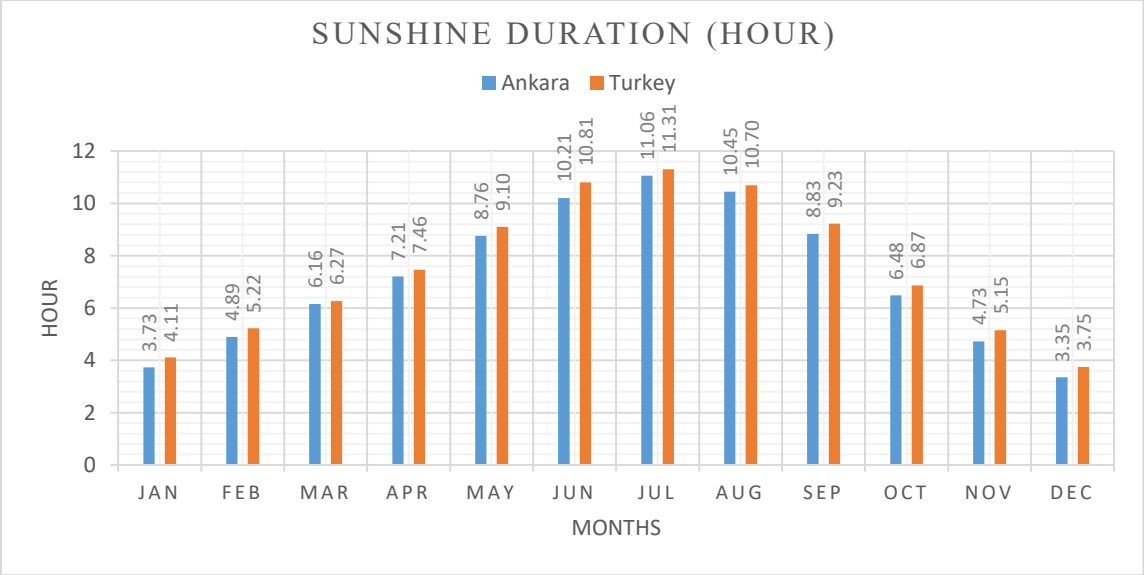


**Figure 2.9 Comparison of Mean Sunshine Duration for Ankara and Turkey Average**

Finally, a simulation was executed for some of the cities in Turkey. The Figures below include the simulated meteorological data for Ankara for five years (i.e., 2012-2016). The results were derived based on the HANWHA QCELL Q.PRO BFR-G4 265 Watt PV module [32] with a roof pitch of 14° and a panel tilt of 14.3°. Figure (2.10) shows the example output of PV module simulation. From this, it can be seen that the module temperature was calculated at 64.4 °C during the measured five years; when the module reached the maximum temperature, the ambient and sky temperatures were measured at 40.8°C and 16.4°C, respectively.

```
Study Date:     2018_01_28
Study Filename: 2018_01_28_Ankara_0001
Study Location: Ankara
Study Panel data:   HANWHA_QCELLS_QPRO_BFR_G4_265W__v001
Simulation:     PVthermal_v1

Panel Parameters:
  Area:      1.67 [m^2]
  Efficiency:   15.9 [%]
  Specific heat:    1.59 [WH/m^2]

Mounting Parameters:
  Roof pitch:   14.0 [deg]   3.0/12 [rise/run]
  Panel tilt:   14.3 [deg]

Starting analysis:
..................................... DONE

Elapsed time is 23.688997 seconds.

Panel Temperature:  Ambient Temperature:    Sky Temperature:
Max:      64.4 [C]  Max:      40.8 [C]  Max:      28.0 [C]
Min:     -19.9 [C]  Min:     -15.9 [C]  Min:     -45.0 [C]
Max Hour:     5003      Max Hour      5003      Max Hour:     5005
Min Hour:    26502      Min Hour     26502      Min Hour:    26501
At Panel max:             40.8 [C]            16.4 [C]
At Panel min:            -15.9 [C]           -42.3 [C]
```

**Figure 2.10 Example Output of PV Module Simulation**

Figure (2.11) shows the available data obtained from the Turkish State Meteorological Service dataset for Ankara during the measured five years (2012-2016). The first four traces are the following input data: solar insolation, ambient temperature, sky cover, and wind speed. The bottom trace shows the calculated PV module temperature. The module temperature fluctuates between -20°C to 64°C across the five years.

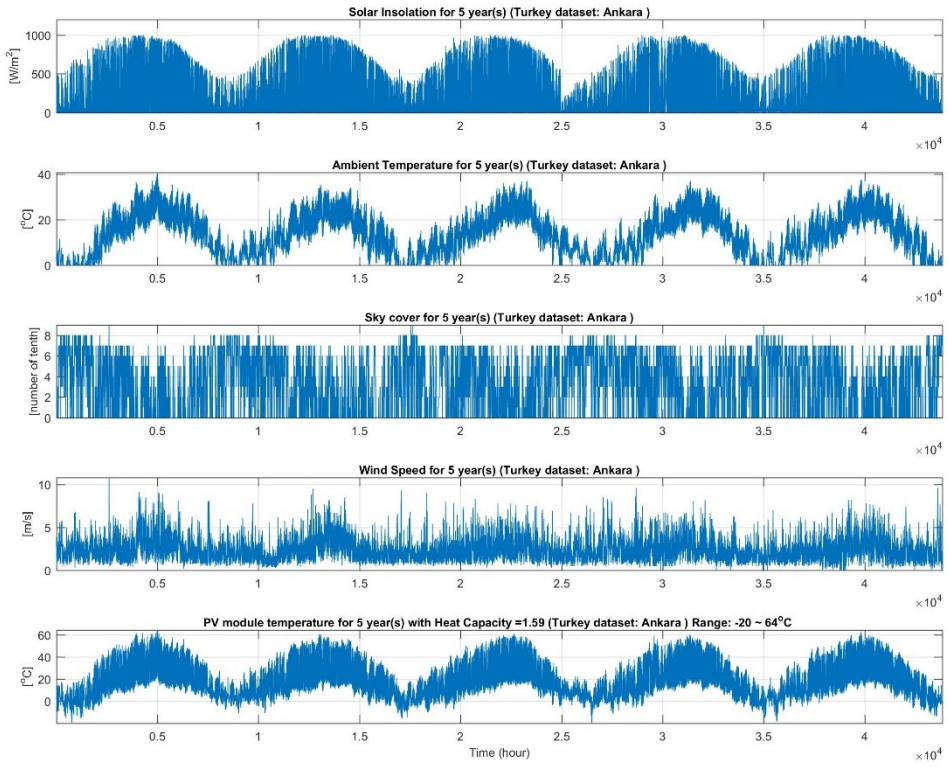


**Figure 2.11 Five Years of Time Trace for Ankara**

Figure (2.12-a) shows a histogram of the ambient temperature in Ankara during operational hours, when the solar insolation was higher than 50 W/m$^2$. The top graphic is the ambient temperature histogram for the five years when the inverter was working. The Figure (2.12-b) illustrates the cumulative distribution function. For example, 30°C corresponds to 0.9 in the Figure (2.12-b). This means that the ambient temperature was less than 30°C during the 16,972 operating hours (18858 * 0.9 = 16972). The Figure (2.12-c) focuses on the high temperature in the top graphic.

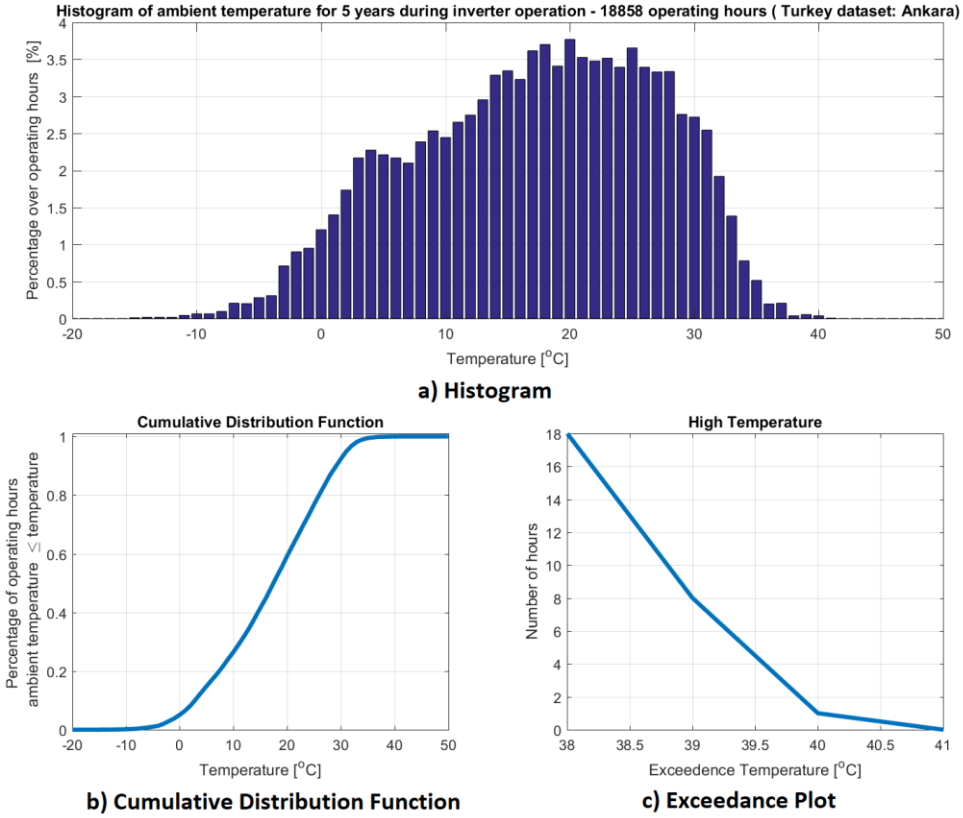


**Figure 2.12 Five-Year Histogram of Ambient Temperature**

Figure (2.13) includes the histogram of the PV module temperature for five years. Particularly, Figure (2.13-c) shows the histogram for the operating hours occurring while the temperature was at its highest. Although the maximum PV module temperature was found to be 64.4°C, the temperature was only at that maximum for a limited period of time. The bottom figure on the right indicates the number of hours during which the PV module was at its maximum temperature. From Figure (2.13-c), it can be seen that the module temperature exceeded 60°C for almost 52 hours of the 18,858 total operating

hours. This represented 0.28% of the total operating hours, suggesting that the PV module integrated inverter should be designed to work at nearly 65°C.

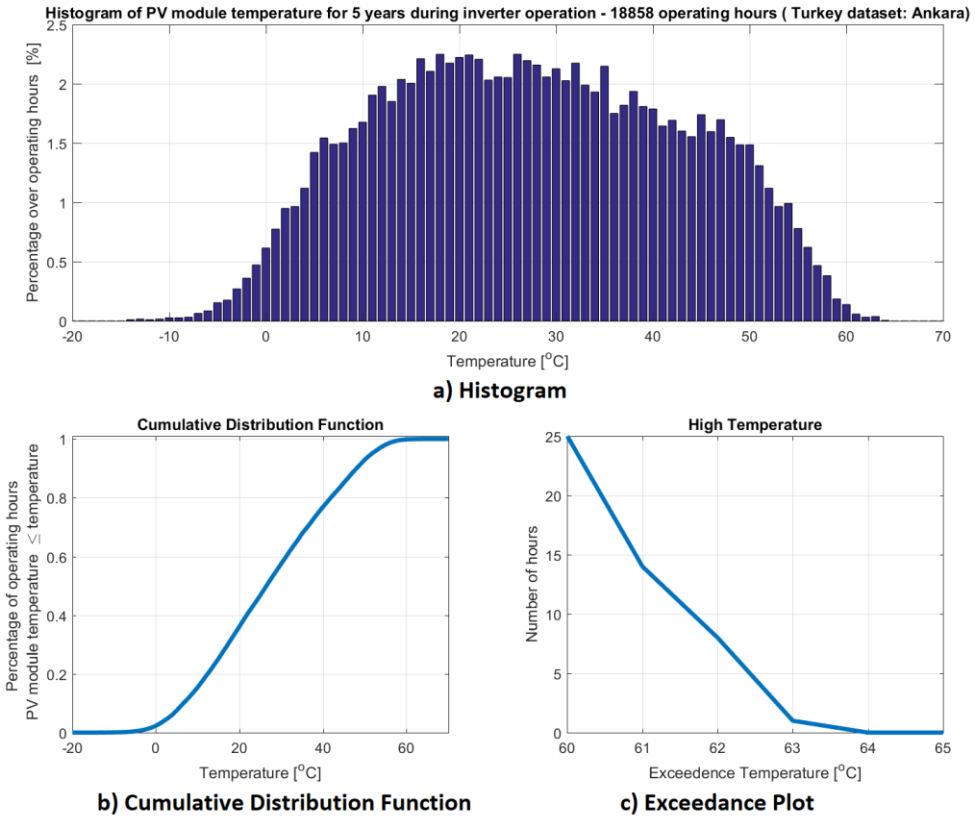


**Figure 2.13 Five-Year Histogram of the PV Module Temperature**

## 2.5 Conclusion

When the thermal model was run for different cities, it indicated that hot ambient air temperatures did not necessarily mean hot PV module temperatures. Meteorological parameters, and PV module properties and installation types (such as tilt and roof angle)

affected the PV module temperature. The simulation can be re-run in the future by changing the PV module properties, installation type, and angles so that they match specific PV modules and locations. The Figure (2.14) and Table (2.3) below indicate the locations and maximum module temperatures of different cities in Turkey, respectively. The detailed results for these cities can be found in the Appendix.

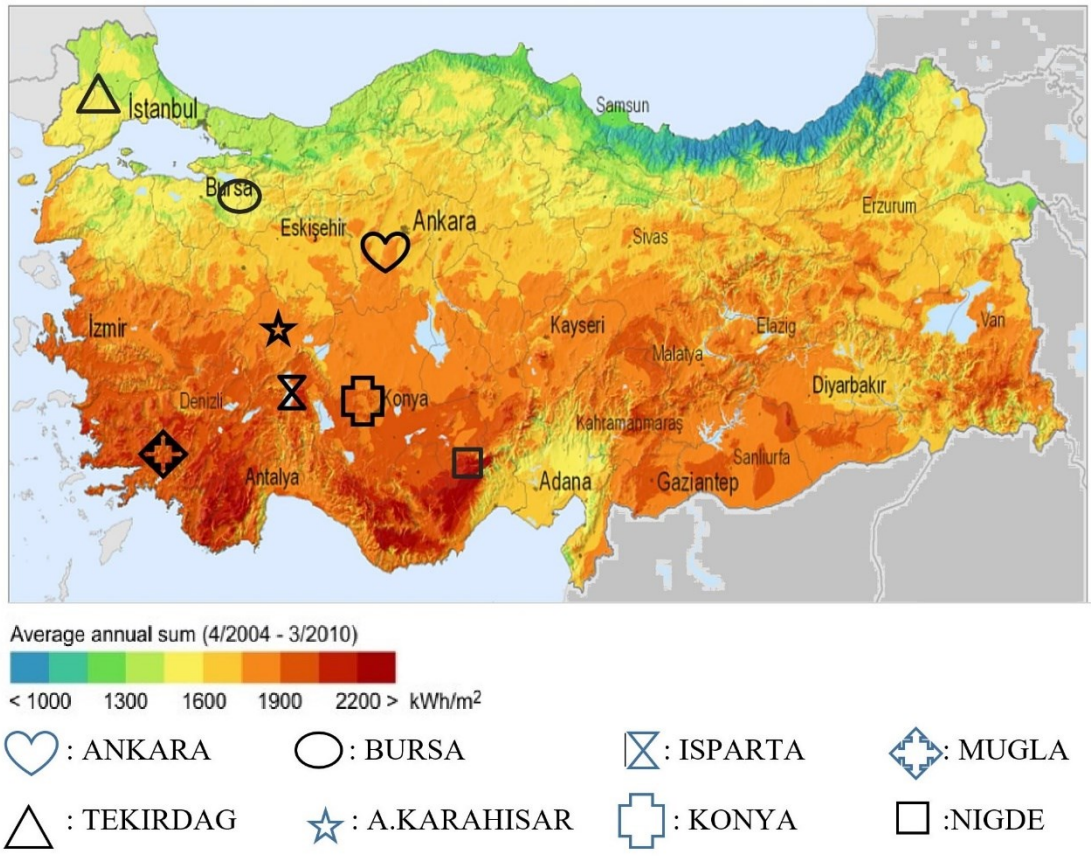


**Figure 2.14 Map of Direct-Normal Insolation for Turkey Showing the Location of the Evaluated Cities, Adapted from [13]**

**Table 2.3 Thermal Model Results for Different Cities**

| | **Maximum PV Module Temperature (°C)** | **Simulated Time Period (total hours/operational hours)** | **Duration at high temperature ( >=60 °C ) (%-minutes)** | |
|---|---|---|---|---|
| **MUGLA** | 70.1 | 43848/18242 | 3.65% | 665 hour |
| **ISPARTA** | 65.7 | 43848/19474 | 0.57% | 111 hour |
| **KONYA** | 65.7 | 26304/11664 | 0.04% | 5 hour |
| **AFYONKARAHISAR** | 64.8 | 26304/11536 | 0.52% | 60 hour |
| **ANKARA** | 64.4 | 43848/18858 | 0.28% | 52 hour |
| **BURSA** | 62.3 | 35064/13560 | 0.27% | 36 hour |
| **TEKIRDAG** | 61.8 | 43848/19726 | 0.07% | 14 hour |
| **NIGDE** | 61.3 | 26304/11652 | 0.06% | 7 hour |

The Figure (2.15) shows the PV module temperature, average ambient temperature, and maximum ambient temperature comparison for different cities.

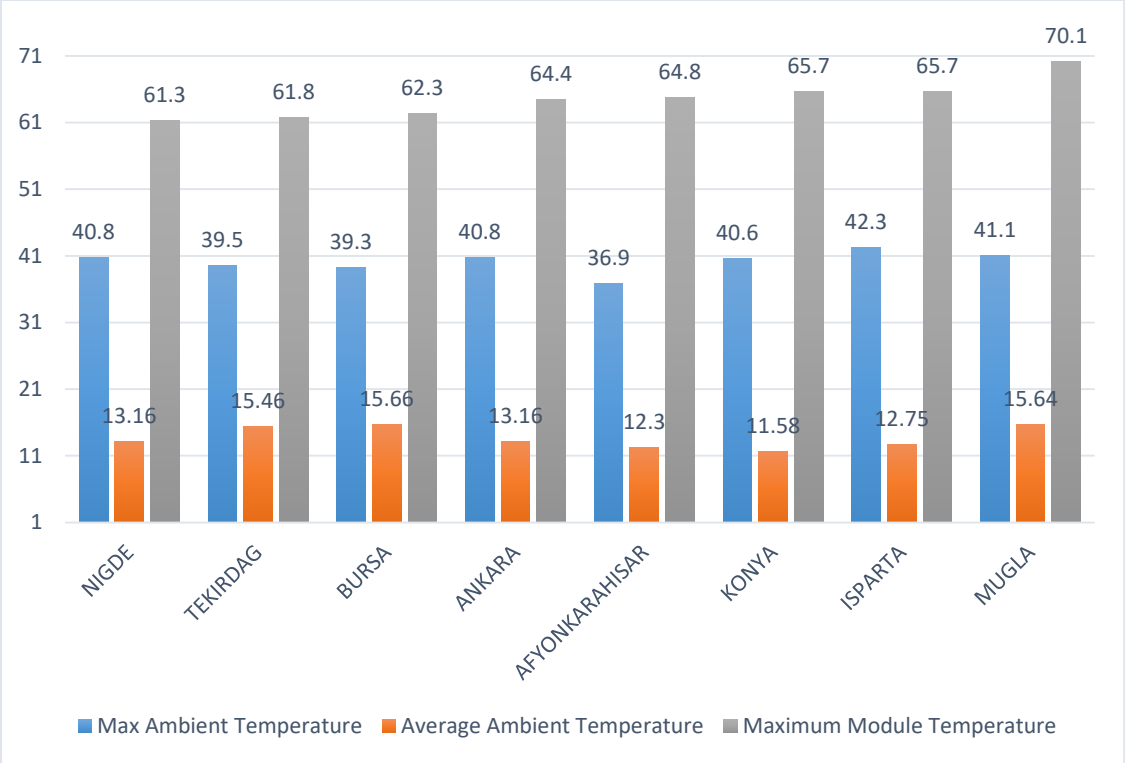


**Figure 2.15 PV Module and Ambient Temperature Comparison for Evaluated Cities**

# 3. ELECTRICAL MODELING

## 3.1 Introduction

A PV module consists of a group of PV cell. Without loss of generality, this chapter will consider silicon-based PV cells, but the concepts apply to other cell technologies by suitably changing the technology-specific relationships and parameters. The temperature of each cell depends on the band gap in the junction. If the band gap is reduced, meaning that more photons participate in the electron-hole pairs, the cell temperature increases [8]. Increasing the cell temperature causes a reduction in the open circuit voltage and slight increase in the short circuit current [8]. Short circuit current, $I_{SC}$, and open-circuit voltage, $V_{CO}$, are two relevant parameters of the I-V curve for a PV module [7]. PV module temperature and solar radiation affect the short-circuit current, $I_{SC}$, and open-circuit voltage, $V_{CO}$. When the insolation rises, the open-circuit voltage, $V_{CO}$, slightly increases. In addition, module temperature, which impacts short circuit current, $I_{SC}$, and open-circuit voltage, $V_{CO}$, is relevant to the ambient temperature, as calculated in the thermal model. Hence, meteorological parameters such as ambient temperature and insolation play a key role in understanding a PV module behavior.

Although PV modules work across an extensive operating range, their datasheets reflect parameters only applicable at standard test conditions (i.e., 25°C and 1,000 W/m$^2$). As calculated in the previous section, operating temperature and solar radiation are not constant values, as they are on the datasheet (i.e., 25°C and 1,000 W/m$^2$). Since operating temperature and solar radiation fluctuate (as can be seen in Figure (2.11)), output current,

output voltage, and maximum power also fluctuate, depending on the meteorological parameters. Hence, it is important to consider PV module behavior in various temperatures and levels of insolation. Electrical modeling helps with obtaining current-voltage (I-V) and power-voltage (P-V) characteristics curves. The model also can assist designers with creating more efficient and reliable design for different locations where the climate may vary.

In this regard, the output voltage of a PV module can be calculated by incorporating the various meteorological variations. In this research, the calculations were completed based on the fundamental PV cell equations [33]. After the thermal and electrical modeling were completed, the outputs were used to determine performance, module lifetime, and reliability calculations. These are described in the following chapter.

## 3.2 Photovoltaic Cells and Modules

The most basic model of a PV cell is an electrical circuit containing a diode and current source such that the current source provides the photo-current. The current is based on insolation, and the diode provides current voltage relation. A simplified equivalent circuit is shown in Figure (3.1). In order to fully comprehend the circuit model of a PV cell, it is crucial to understand the behavior and electrical characteristics of its components in response to light and temperature. A PV cell is similar to a p-n junction diode, which is a semiconductor device that works with charge carrier availability. When insolation reaches a photovoltaic cell, some parts are absorbed, others are reflected, and the rest goes through the cell. Electric power is produced by the photons that are absorbed

by the photovoltaic cell. After insolation is absorbed by the junction, the existing energy in the photons transfers to the electron system. Hence, charge carriers are created. Charge carriers depend on flux incident light and absorption capacity. This is why the output of a PV module changes with fluctuations in temperature and level of insolation.

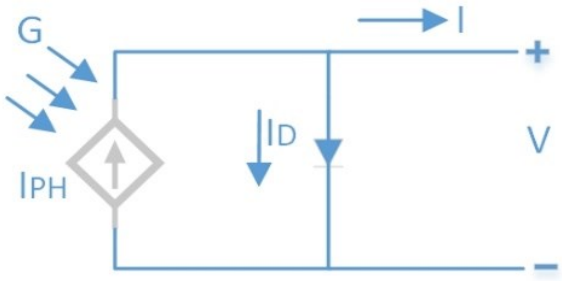


**Figure 3.1 Ideal Single Diode Model**

## 3.3 Mathematical Model of a PV Cell

The mathematical equations for an ideal single diode model are derived by considering the diode equation and Kirchhoff law. The output current is derived by using Kirchhoff law, as in Figure (3.1).

$$I = I_{ph} - I_d \tag{3.1}$$

where $I_{ph}$ is the photo-current and $I_d$ is the diode current.

Equation (3.2) represents the ideal diode equation. The output current of the ideal single diode model is then calculated by substituting equation (3.2) into equation (3.1) [34].

$$I_d = I_s\left(\exp\left(\frac{qV_{PV}}{N_S kAT}\right)-1\right) \tag{3.2}$$

$$I = I_{ph} - I_s\left(\exp\left(\frac{qV_{PV}}{N_S kAT}\right)-1\right) \tag{3.3}$$

where $I_s$, q, $V_{PV}$, $N_s$, k, A, and T represent the saturation current, electron charge ($1.602*10^{-19}$ C), module output voltage, number of series cell in PV module, Boltzmann constant ($1.381*10^{-23}$ J/K), diode ideality factor and cell temperature (Kelvin) respectively.

The current source generates a photocurrent ($I_{ph}$) that is proportion to the incoming solar radiation; this is calculated by the following equation (3.4) [35].

$$I_{ph} = G(I_{sc} + \alpha\Delta T) \tag{3.4}$$

Obviously, solar irradiance (G ($kW/m^2$)), short-circuit current ($I_{sc}$), and the current temperature coefficient (α) all influence the photon current. While the short circuit current ($I_{sc}$) and current temperature coefficient (α) are available from the module

datasheet, solar irradiance and temperature differences were used through the meteorological dataset.

As mentioned above, increasing the cell temperature causes a reduction in open circuit voltage ($V_{OC}$) at the rate of the voltage temperature coefficient (β) [33, 35].

$$V_{oc}(G,T) - V_{oc}(G,T_0) = -|\beta|\Delta T \tag{3.5}$$

In the above equation, $V_{OC}$ (G, T) and $V_{OC}$ (G, $T_0$) represent the open-circuit voltage at a specific temperature (T) and temperature at a standard test condition ($T_0$), respectively. The $V_{OC}$ at a specific temperature is calculated as follows [36].

$$V_{oc} = \frac{N_s kTA}{q} \ln\left(\frac{I_{ph}}{I_s} + 1\right) \tag{3.6}$$

When equation (3.6) is applied to equation (3.5) for $V_{OC}$ (G, T) and $V_{OC}$ (G, $T_0$), equation (3.7) is derived.

$$\frac{N_s kA}{q}\left[T \ln\left(\frac{G(I_{sc} + \alpha\Delta T)}{I_s} + 1\right) - T_0 \ln\left(\frac{GI_{sc}}{I_{rs}} + 1\right)\right] = -|\beta|\Delta T \tag{3.7}$$

Finally, after rearranging equation (3.7), the saturation current, $I_s$, is determined, as below.

$$I_s = \frac{\exp\left(\frac{|\beta|\Delta Tq}{N_s kTA}\right) G(I_{sc} + \alpha\Delta T)}{\left(\frac{GI_{sc}}{I_{rs}} + 1\right)^{\frac{T_0}{T}} - \exp\left(\frac{|\beta|\Delta Tq}{N_s kTA}\right)} \tag{3.8}$$

In equation (3.8), $I_{rs}$ indicates the saturation current at standard test conditions; it is calculated with the following equation [33].

$$I_{rs} = \frac{I_{sc}}{\exp\left(\frac{qV_{oc}}{N_S kAT_0}\right) - 1} \tag{3.9}$$

Equation (3.3) produces the output current at a specific temperature. The output current at a maximum power point ($I_{mpp}$ and $V_{mpp}$) is determined, as below.

$$I_{mpp} = I_{sc} - I_{rs}\left(\exp\left(\frac{qV_{mpp}}{N_S kAT_0}\right) - 1\right) \tag{3.10}$$

where $I_{mpp}$, $V_{mpp}$, $I_{sc}$, and $T_0$ represent output current and output voltage at the maximum power point, short circuit current, and cell temperature at standard test condition.

The other unknown parameter, diode ideality factor (A), which is typically between 1 and 2 according to the literature, applies via equations (3.9) and (3.10) [33, 35].

$$\frac{I_{mpp}}{I_{sc}} = \exp\left(\frac{qV_{mpp}}{N_S kAT_0}\right) - \left(\frac{I_{sc} - I_{mpp}}{I_{sc}}\right)\left[\exp\left(\frac{qV_{oc}}{N_S kAT_0}\right)\right] \tag{3.11}$$

**Table 3.1 Electrical Characteristics of the PV Module [32]**

| | | |
|---|---|---|
| **Power at MPP [W]** | $P_{mpp}$ | 265 |
| **Short Circuit Current [A]** | $I_{sc}$ | 9.23 |
| **Open Circuit Voltage [V]** | $V_{OC}$ | 38.01 |
| **Current at MPP [A]** | $I_{mpp}$ | 8.62 |
| **Voltage at MPP [V]** | $V_{mpp}$ | 30.75 |
| **Efficiency [%]** | $\eta_{ef}$ | >=15.9 |
| **Temperature coefficient of $I_{SC}$ [%/K]** | $\alpha$ | 0.04 |
| **Temperature coefficient of $V_{OC}$ [%/K]** | $\beta$ | -0.30 |
| **Temperature coefficient of $P_{MPP}$ [%/K]** | $\gamma$ | -0.41 |

Table (3.1) includes the used module parameters at standard test conditions (1,000 W/m2 and 25°C). In this research, a HANWHA QCELL Q.PRO BFR-G4 265 Watt PV module was used [32]. The PV module I-V and P-V curves were derived by using the given equations and datasheet parameters. Figure (3.2) was derived by applying a constant level of solar irradiation (G = 1 kW/m$^2$) and temperature (T = 25°C). The result is that the power generation reaches its maximum only at a specific voltage and current. This maximum power point (MPP), then, become the goal operating point to obtain maximum energy production.

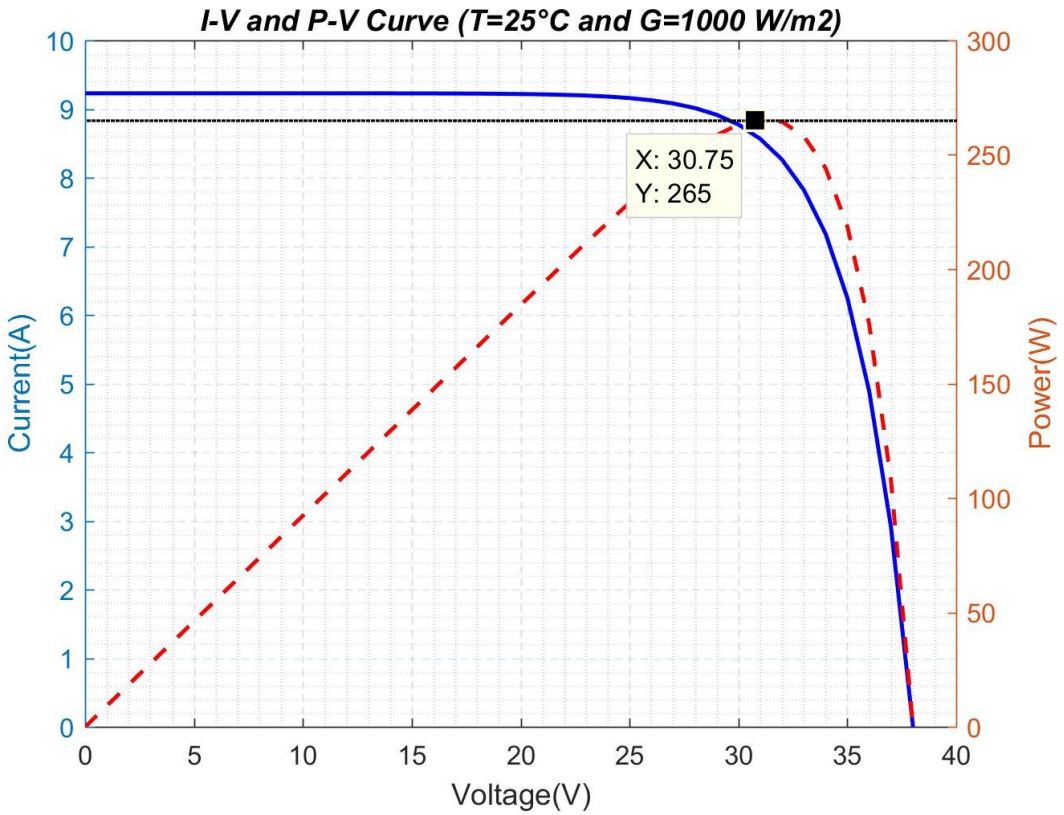


**Figure 3.2 I-V and P-V Curves for the Used PV Module**

Figure (3.3) was obtained by applying a variable insolation and constant cell temperature (25°C). It was found that while decreasing the solar irradiation decreased the module current, the output voltage changed only slightly. The output power decreased while insolation decreased as illustrated in the graph on the left.

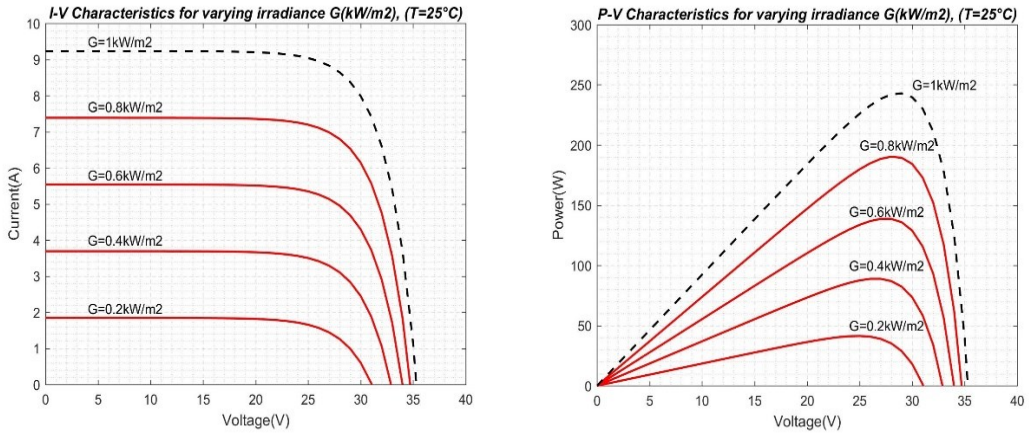


**Figure 3.3 I-V and P-V Curves for the PV Module with Varying Solar Irradiance**

Figure (3.4) was derived by applying a variable temperature and constant level of solar irradiation (G = 1 kW/m$^2$). It was found that while decreasing the temperature increased the module output voltage, the current was almost unchanged. The output power decreased while temperature increased as seen in the graphic on the left.

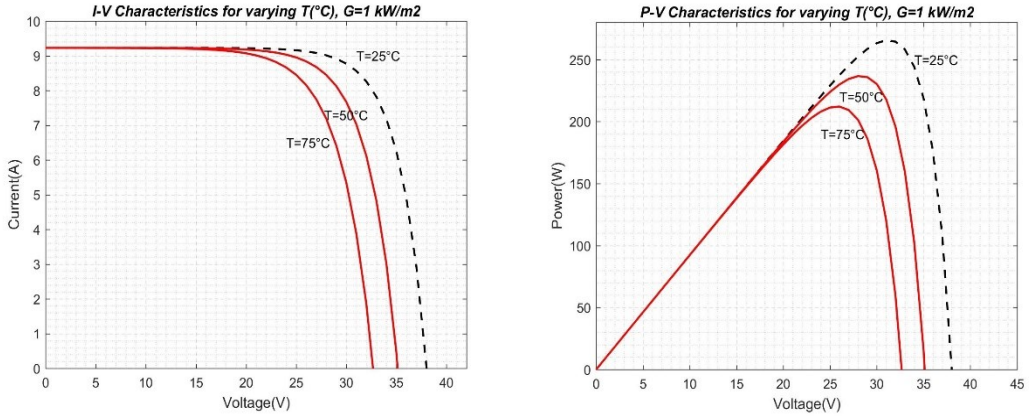


**Figure 3.4 I-V and P-V Curves for the PV Module with Varying Tempeature**

As a result, both Figures (3.3) and (3.4) show that environmental conditions have a substantial influence on a PV module output voltage, current, and power. The effects of environmental conditions were then confirmed via mathematical equations, as is described below.

## 3.4 Electrical Model Output via Actual Meteorological Datasets

In the previous section, mathematical equations for the PV module were given and used to calculate output voltage and current under standard test conditions. However, a PV module functions across a wide range of operating points, so an actual meteorological data set was used to determine the PV module actual behavior in response to variable meteorological parameters. As described in this section, the PV module output voltage was derived using actual meteorological datasets taken from the Turkish State Meteorological Service.

In order to calculate the PV module output, it was assumed that the PV module system worked at the maximum power point (MPP). Thus, the following equations were derived using the power law equation.

$$P_{PV} = V_{PV} I = V_{PV} I_{ph} - I_s V_{PV} \left( \exp\left( \frac{q V_{PV}}{N_S kAT} \right) - 1 \right) \tag{3.12}$$

The maximum operating voltage is obtained by setting equal to zero derivative of the power in equation (3.12), with respect to module output voltage $V_{PV}$.

$$0 = \frac{dP_{PV}}{dV_{PV}} = I_{ph} + I_s \left( 1 - \left( 1 + \frac{q V_{PV}}{N_S kAT} \right) \exp\left( \frac{q V_{PV}}{N_S kAT} \right) \right) \tag{3.13}$$

Solving equation (3.13) by taking into consideration $V_{PV}$ gives the voltage across the PV module. Figure (3.5) indicates the module temperature, insolation and PV module output voltage. In this way, the impacts of the module temperature and solar radiation are clear. The figure was created for Ankara period of 2012 to 2016.

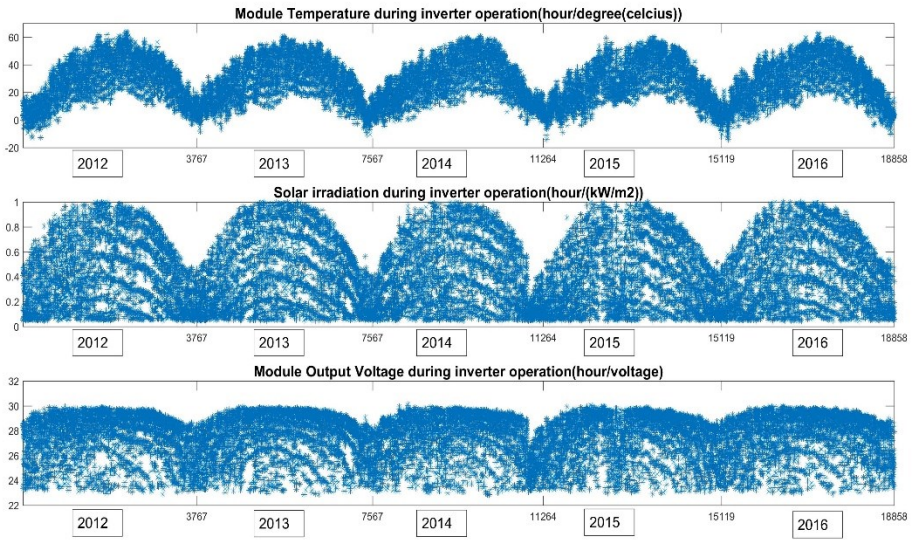


**Figure 3.5 Electrical Model Output for Ankara**

Figure (3.6) shows a histogram of the PV module output voltage for five years in Ankara. The output voltage is 29 V almost 27% of the time. In addition, Figure (3.7) includes a histogram of the PV module output voltage for additional city simulations. It can be seen that although the percentages are different, the PV module voltage for all cities is 29 V almost most of the time. The results will be used to calculate the electrical stress on the module components.

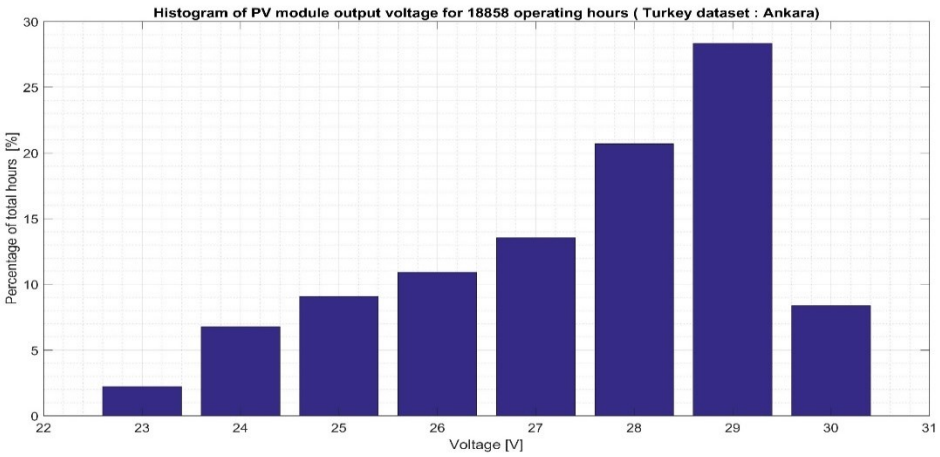


**Figure 3.6 Histogram of the PV Module Output Voltage for Ankara**

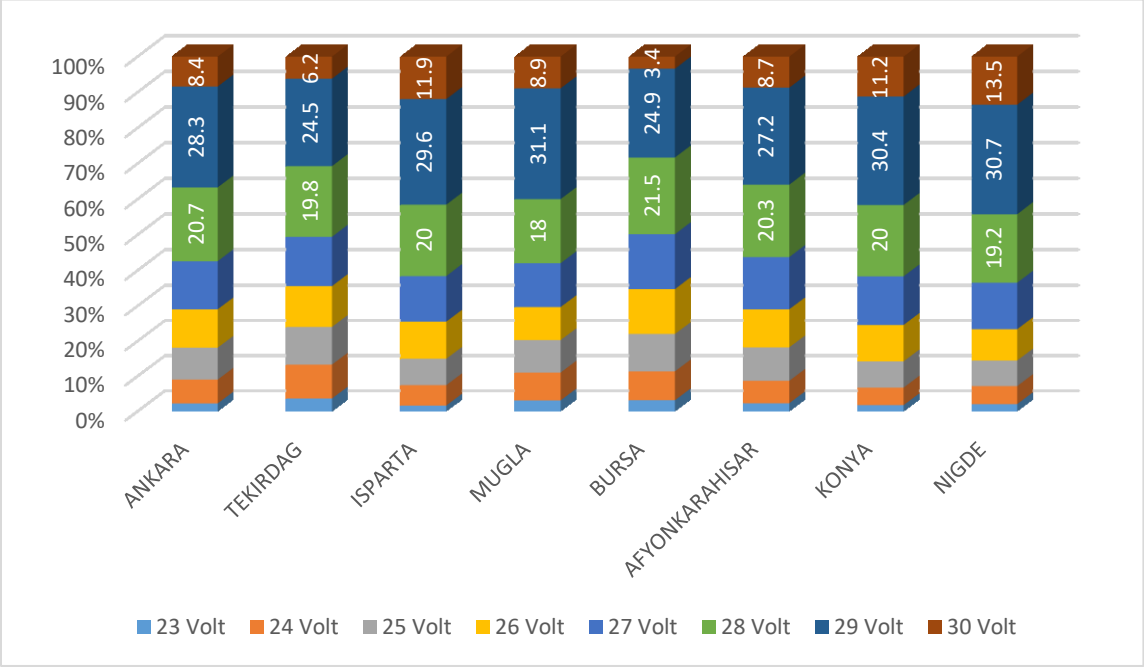


**Figure 3.7 Histogram of the PV Module Output Voltage for Different Cities**

## 3.5 Conclusion

Although PV module datasheets offer the parameters only for specific conditions, the parameters can be determined for all operating points, with the help of actual datasets and mathematical equations for the PV cell. In this chapter, the PV module output voltage was determined by using an actual meteorological data set and considering the maximum power point. It was calculated for different cities and it is seen that module voltage stress are different for different cities. These results will be used in next chapter for reliability calculation.

# 4. RELIABILITY CALCULATIONS

## 4.1 Introduction

Power electronics circuits and devices are widely used in both industry and daily life. In a grid-connected PV system inverter, as the module integrated microinverter is placed on, behind, or near to PV module, the components used in the inverter are exposed to harsh climate conditions [37]. Hence, the reliability of the PV module and power electronics are an essential element that should be taken into consideration when determining the benefits and lifetime of a PV system. Although a PV module lifetime is usually between 20 and 25 years [38], the life of the power electronics (such as an integrated microinverter) can be shorter [39]. Therefore, the lifetime and reliability of power electronics can restrict the lifetime of the whole system, in addition to creating the need for replacements and increasing repair costs. As a result of this lifetime mismatch between the inverter and PV module, the total lifetime cost of the system increases; the inverter must be replaced at least once, and sometimes more, before the end of the PV module lifespan. Consequently, this causes an undesirable increase in energy cost.

In this context, the reliability of the components used in the candidate micro-inverter topologies, as well as the reliability of the micro-inverter as a whole, were calculated as described in this chapter. The reliability of the components and PV module depend on the operating temperature, ambient temperature, and voltage stress. The calculation approach used in this research took into consideration different cities with

different climatic conditions, so that the impact of the meteorological parameters on the unit reliability and lifetime could be efficiently evaluated.

The reliability calculation is based on the MIL 217 handbook [18], which is widely used in electronics systems and equipment. Even though companies and countries often declare the self-reliability of their prediction methods, prediction models are often very similar. Reliability calculations based on the MIL 217 handbook take into consideration different stress factors such as the surrounding temperature, voltage, and current of the components [39]. In this research, the calculations were completed with a large dataset that included the PV module temperature derived from meteorological data (see Chapter 2) and the PV module output voltage derived by using a mathematical modeling of the PV module (see Chapter 3). It is crucial to complete these calculation with a wide dataset. If the reliability calculations were completed for only one operating point, the results would have been unrealistic. For example, the failure rate, which is calculated using either maximum or minimum temperature, bring undesirable and desirable results, respectively. Hence, instead of the employing the Mean Time Between Failures (MBTF), which is the most widely used reliability index, for only one operating point, a wide range of measured and calculated data were used to calculate the MTBFs at all operating points. The results helped to determine the minimum MTBF, averaged MTBF, and weighted MTBF. In this regard, the operating temperature and operating voltage histograms discussed in previous sections of this research were shown to significantly influence the reliability of the power electronics.

## 4.2 Methods of MTBF Calculations

There are different ways to calculate the failure rate and MTBF. After calculating the MTBF, the minimum, average, and weighted MTBFs could be derived by using the calculated failure rate. The weighted MTBF was calculated by taking into consideration the temperature frequency of the operating points. The methods of calculations are included below [40].

a) The failure rate was calculated at each operating point.

b) The failure rate was calculated at a maximum temperature to determine the minimum MTBF (or maximum failure rate), which was the worst-case scenario.

$$MTBF_{\min} = \frac{1}{\lambda_{Tmax}} \tag{4.1}$$

c) The calculated failure rated at each operating point was used to determine the mean value, which was the averaged MTBF.

$$MTBF_{avg} = \frac{1}{L}\left( \sum_{i=1}^{L} MTBF_i \right) \tag{4.2}$$

where L indicates the number of operating points.

d) Since the inverter works at some operating points more often than others, as seen in Figure (4.1), the weighted failure rate was calculated. Weighted MTBF approach offers more realistic results.

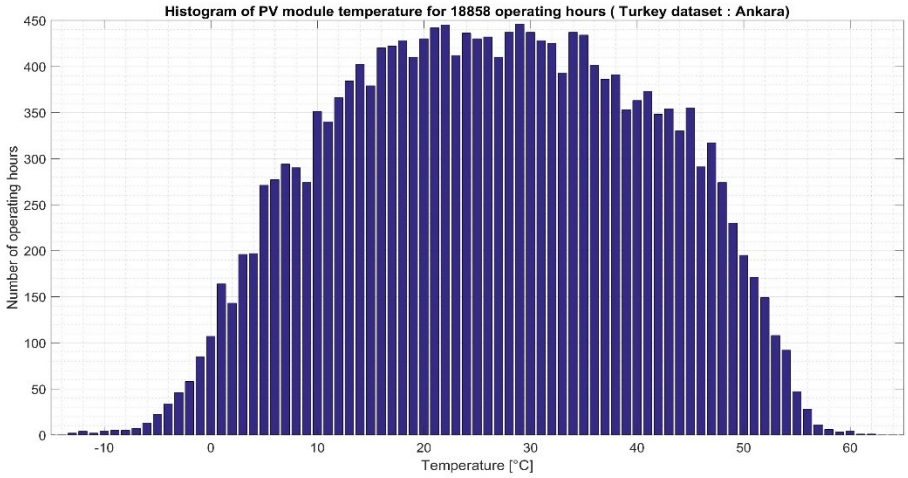


**Figure 4.1 Histogram of Module Temperature for Ankara**

The weighted failure rate was calculated by considering the operating point temperature frequency. It was calculated by using the following equations [37].

$$MTBF_{weighted} = \sum_{k=1}^{N_n} MTBF\left(T_k\right) * W_k \tag{4.3}$$

$$\text{where } T_k = \frac{T_i + T_{i+1}}{2} \qquad \{k = 1, 2, .... N_n\} \tag{4.4}$$

The upper limit of the total sequence in equation (4.3) was calculated as in equation (4.5).

$$N_n = round\left(\frac{T_{\max} - T_{\min}}{S}\right) \tag{4.5}$$

where S is a step in the temperature range.

$W_k$ is the weight factor, which is calculated as in (4.6).

$$W_k = \frac{N_i}{N_T} \qquad \{i = 1, 2, ...., N_n\} \tag{4.6}$$

$$\begin{cases} N_i, & \text{number of the operating temperature at i}^{th} \text{ temperature range} \\ N_T, & \text{total number of the operating temperature points} \end{cases}$$

The above methods were used to find the failure rate of each individual component. The total failure rate was found by using equations (4.7) and (4.8) [41]. The *n* indicates the number of components.

$$\lambda_{inverter} = n_{mos} * \lambda_{mos} + n_{diode} * \lambda_{diode} + n_{cap.} * \lambda_{cap.} + n_{tr}\lambda_{tr} + n_{ind.}\lambda_{ind.} \tag{4.7}$$

$$MTBF = \frac{1}{\lambda_{inverter}} = \frac{1}{n_{mos} * \lambda_{mos} + n_{diode} * \lambda_{diode} + n_{cap.} * \lambda_{cap.} + n_{tr}\lambda_{tr} + n_{ind.}\lambda_{ind.}} \tag{4.8}$$

In a PV system, the components of the power electronics are the primary contributors to the system failure rate. The Table (4.1) listed below includes the failure rate equations for the components used in the power electronics of the candidate micro-inverter system. After the component types and parameters were identified in the MIL 217 handbook [18], it was determined that a stress factor calculation was needed for the diode and capacitor. As it is different for each circuit, basic circuit analyses needed to be employed, as follows. While the stress factor depended on the electrical model output (voltage), the reliability equations relied on the thermal (temperature) and electrical (voltage) model outputs.

$$\begin{cases} \lambda_b, & \text{Base Failure Rate} \\ \pi_T, & \text{Temperature Factor} \\ \pi_E, & \text{Environmental Factor} \\ \pi_Q, & \text{Quality Factor} \\ \pi_A, & \text{Application Factor} \\ \pi_{CV}, & \text{Capacitance Factor} \\ \pi_S, & \text{Electrical Stress Factor} \\ \pi_C, & \text{Contact Construction Factor} \end{cases}$$

**Table 4.1 Component Failure Rates [18]**

| Failure Rate ($\lambda_P$) / $10^6$ Hours | | |
|---|---|---|
| MOSFET | $\lambda_{mosfet} = n\lambda_b \pi_T \pi_A \pi_Q \pi_E$ | $\pi_T = \exp\left(-1925\left(\frac{1}{T_J + 273} - \frac{1}{298}\right)\right)$<br>$\lambda_b = 0.012 \quad \pi_A = 10 \quad (Power \geq 250W)$<br>$\pi_Q = 5.5$ (Lower Quality) |
| DIODE | $\lambda_{diode} = n\lambda_b \pi_T \pi_S \pi_C \pi_Q \pi_E$ | $\pi_T = \exp\left(-3091\left(\frac{1}{T_J + 273} - \frac{1}{298}\right)\right)$<br>$\lambda_b = 0.025 \quad \pi_Q = 5.5$ (Lower Quality)<br>$\pi_S = \begin{cases} 0.054 & V_S \leq 0.3 \\ V_S^{2.43} & 0.3 < V_S \leq 1 \end{cases}$ |
| CAPACITOR (Electrolytic Aluminum Capacitor) | $\lambda_{capacitor} = n\lambda_b \pi_{CV} \pi_Q \pi_E$ | $\lambda_b = 0.00254\left(\left(\frac{S}{0.5}\right)^3 + 1\right)\exp\left(5.09\left(\frac{T_J + 273}{378}\right)^5\right)$<br>$\pi_{CV} = 0.34\left(C^{0.18}\right) \quad \pi_Q = 10$ (Lower Quality) |
| CAPACITOR (Film Capacitor) | $\lambda_{capacitor} = n\lambda_b \pi_{CV} \pi_Q \pi_E$ | $\lambda_b = 0.00099\left(\left(\frac{S}{0.4}\right)^5 + 1\right)\exp\left(2.5\left(\frac{T_J + 273}{398}\right)^{18}\right)$<br>$\pi_{CV} = 1.1\left(C^{0.085}\right) \pi_Q = 10$ (Lower Quality) |
| TRANSFOMER &INDUCTOR | $\lambda_{transformer} = n\lambda_b \pi_T \pi_Q \pi_E$<br>$\lambda_{inductor} = n\lambda_b \pi_T \pi_Q \pi_E$ | $\pi_T = \exp\left(\frac{-0.11}{8.617 * 10^{-5}}\left(\frac{1}{T_J + 273} - \frac{1}{298}\right)\right)$<br>$\pi_Q = 3$ (Lower Quality)<br>$\lambda_{b\_tr} = 0.019 \quad \lambda_{b\_ind} = 0.00003$ |

According to above formula obtained from the MIL 217 handbook [18], the transformer and inductor do not depend on the voltage stress factor. They are affected by the temperature. Also, the MOSFETs do not depend on the voltage stress factor, but since they have a power factor, the power rating is an effect of the MOSFETs. Since the capacitor and diodes are affected by the voltage stress factor and temperature, the voltage stress factors for both were calculated while analyzing the inverter topologies.

## 4.3 Candidate Module Integrated Micro-Inverter (MII) Topologies for Photovoltaic Systems

As solar energy has been common in recent years, residential PV systems have shown a tendency to use module-integrated inverters with power levels ranging from 150 to 300 Watts [42]. Micro-inverters are widely used in domestic PV systems because MII offers certain advantages, such as increased system efficiency, improved energy harvest, and lower installation costs. Moreover, micro-inverters can be charge the battery and eliminate the central inverter. Also, these kinds of inverters can be connected directly to the PV module, so that level of completion increases [1]. They also have individual MPPT control, which improves the performance of PV arrays. Each PV module has a single phase micro-inverter in the micro-inverter system, so if an inverter fails, only one PV module is affected and remainder continue to supply a load so they are more efficient than a string inverter system. Another advantage is that they reduce the high DC voltage in solar systems.

Although they offer certain advantages, they can heat along with PV module because they are located behind or near it. Hence, the reliability of micro-inverters should be considered in order to maximize the unit efficiency and lifetime. Another disadvantage is the power mismatch between load and source. While the PV side has constant power in order to obtain the maximum energy harvest, the grid side power flow varies by time. This leads to a power mismatch between the load and source. The reason for this is explained by the equations below.

Equations (4.9) and (4.10) are used to expressed voltage and current on the grid, respectively.

$$V = V_m \cos(wt) \tag{4.9}$$

$$I = I_m c\,\mathrm{os}(wt + \varphi) \tag{4.10}$$

$$\begin{cases} V_m, & \text{voltage amplitude } [V] \\ I_m, & \text{current amplitude } [A] \\ \varphi, & \text{phase difference} [radian] \end{cases}$$

Instantaneous power on the grid side is calculated by multiplying equations (4.9) and (4.10).

$$P = P_0 + P_0 \cos(2wt + \varphi) \tag{4.11}$$

While the grid-side instantaneous power is equal to equation (4.11), equation (4.12) shows the power on the PV side by considering the PV-side voltage.

$$P_{PV} = V_{MPP} I_{MPP} \tag{4.12}$$

It can clearly be seen that while the power has constant and double frequency terms on the load (grid) side, the PV-side power has only a constant term. This is called a power mismatch between the load and source, as mentioned above. Unless this issue is resolved, the current on the PV side will not remain constant [43], as a result, it will deteriorate the MPPT operating points for the PV module and reduce the generated power. Hence, different power decoupling techniques have been proposed in the literature to solve power mismatch between PV side and load side, based on the location of the decoupling capacitor. The proposed techniques were used in this research to solve the power mismatch between the load and source by employing an energy storage element that filtered the double-frequency ripple [37]. Thus, the decoupling capacitor needed to be wide enough to hold the voltage ripple [43]. The decoupling capacitor used in this research is an energy storage element; it was located between the PV and utility sides. The required decoupling capacitor value is determined using equation (4.13) [44].

$$C_D = \frac{P_{PV}}{W_0 V_{DC} \Delta V} \tag{4.13}$$

$$\begin{cases} V_{DC}, & \text{DC Bus Voltage } [V] \\ \Delta V, & \text{Desired Voltage Ripple } [V] \end{cases}$$

The following sections are categorized by type (i.e., aluminum or film capacitor) and location of the decoupling capacitor, either PV-side or DC-link. Although in the literature there are many single-phase micro-inverters for PV applications [42, 45, and 46], six different topologies, some commercially available, were analyzed here for their reliability [40]. After analyzing the circuit topologies, the effects of the capacitor technology are discussed in terms of their reliability. In this research, a module-integrated micro-inverter rated for 265 W was used to connect the PV module to the AC utility grid ($V_0 = 230\ V_{rms}$ and f = 50 Hz).

### 4.3.1 PV-Side Electrolytic Capacitor with MII

Since a low ripple value across the PV module provides the maximum power point, a small ripple voltage is desirable on the PV side. Hence, the capacitor value required was determined to be 18,000 μF by applying the system specifications (265 W, 30 V, 1.5 V voltage ripple (5%)) to equation (4.13). As the required capacitor is very large, it leads to a large-sized micro-inverter.

Figure (4.2) shows a commercial inverter [40]. The position of the decoupling capacitor is across the PV module terminals. There are three power stages that push-pull converter, H-bridge, and full-bridge voltage inverter. As the push-pull converter amplifies the module voltage at the rate of the turns ratio, the voltage across the diode,

$NV_{PV}$, could be determined. The H-bridge rectifies the output current on the transformer secondary side. Since only two switches carry the current, the inverter has a high level of efficiency as a result of little conduction loss [45].

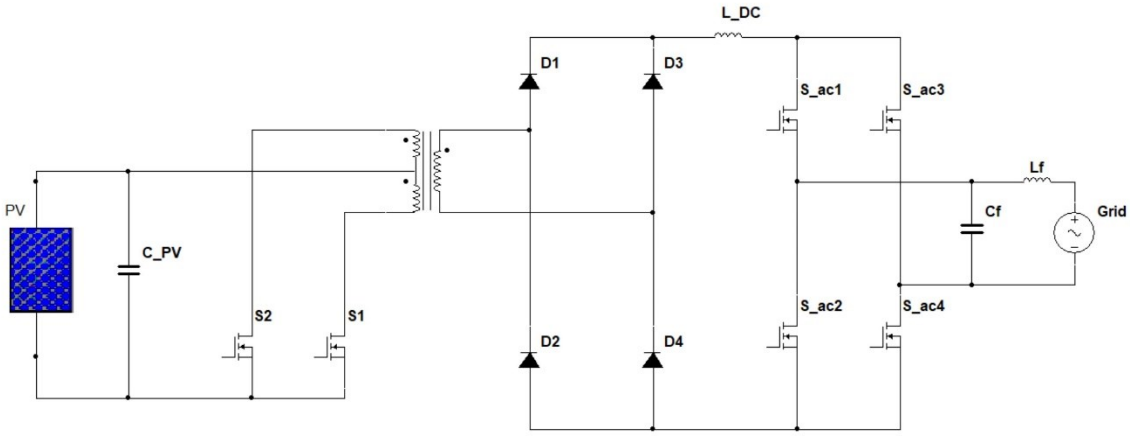


**Figure 4.2 Commercial Inverter Topology (Topology 1)**

The figure (4.3) is a flyback inverter with a center-tapped transformer [47]. The topology is different from the previous, as there are two identical secondary windings. This topology is used to transfer energy from PV side to the AC grid by using two identical windings. Each alternately transfers energy to the AC side during the negative and positive half-cycles in order to generate output. This alternation is provided by the secondary side switches $S_{ac1}$ and $S_{ac2}$. As $S_{ac1}$ and $S_{ac2}$ are placed between the secondary windings and grid, they could be controlled by the grid voltage. The input and output voltage are isolated from one another using a high-frequency transformer, which is also used to increase the PV module voltage to the AC grid level. Moreover, switch $S_1$

operates at a high frequency. As a result, a low pass filter is used on the output to address the limited high-frequency harmonics [48, 49]. Although the same decoupling techniques are used with the previous inverter topology, this topology uses fewer components. The effect of the number of components, then, is also evaluated.

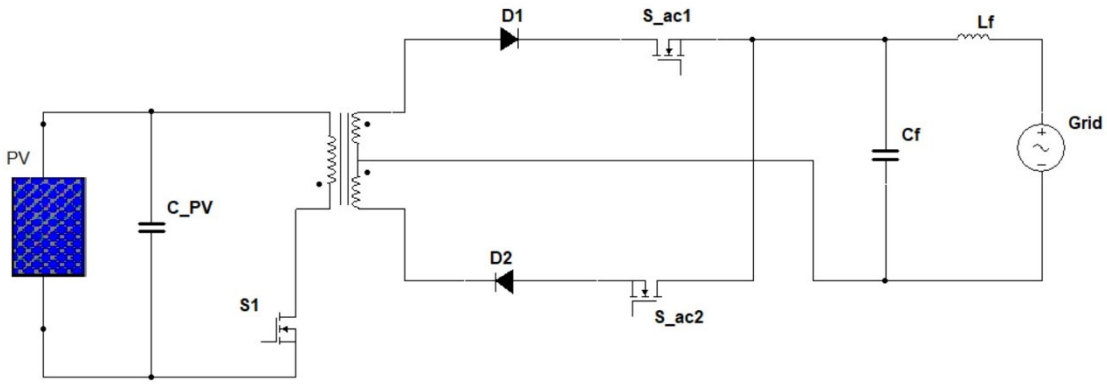


**Figure 4.3 Flyback Current Source Inverter Topology with a PV-side Electrolytic Capacitor (Topology 2)**

### 4.3.2 DC-Link Electrolytic Capacitor with MII

DC-bus voltage is controlled and retained in the DC link. A double-frequency power ripple is stored in the DC link. As the DC-link voltage is higher than the PV-side voltage, the required voltage ripple should be high as well. Hence, the required capacitance value decreases as the voltage ripple and DC-link voltage increase. According to equation (4.13), the required capacitance value is 120 μF.

Figure (4.4) shows three power conversion stages. In this topology, a full-bridge rectifier and voltage source inverter are used. Also, a high-frequency transformer is used to provide isolation.

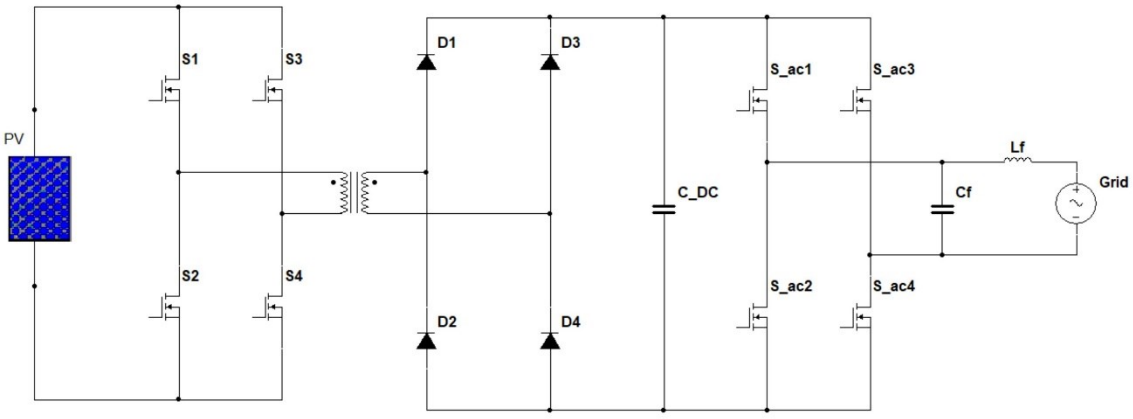


**Figure 4.4 Commercial Inverter Topology with an Electrolytic DC-link Capacitor (Topology 3)**

Figure (4.5) has two stages. The first is a flyback converter that raises the PV module voltage. The second is a full-bridge voltage inverter that can generate a sine form current at the output. Sinusoidal modulation in output current and voltage conversion are completed by the full-bridge converter. In this inverter, the input is the voltage source and output is the current source, so the full bridge and flyback could be connected together to produce a sinusoidal current at the output [50]. Also, the transformer in the flyback converter provides galvanic isolation, meaning greater safety between the load and source. As the decoupling techniques are the same and the number of components

different from the previous topology, the effect of the components number could be evaluated, in terms of reliability.

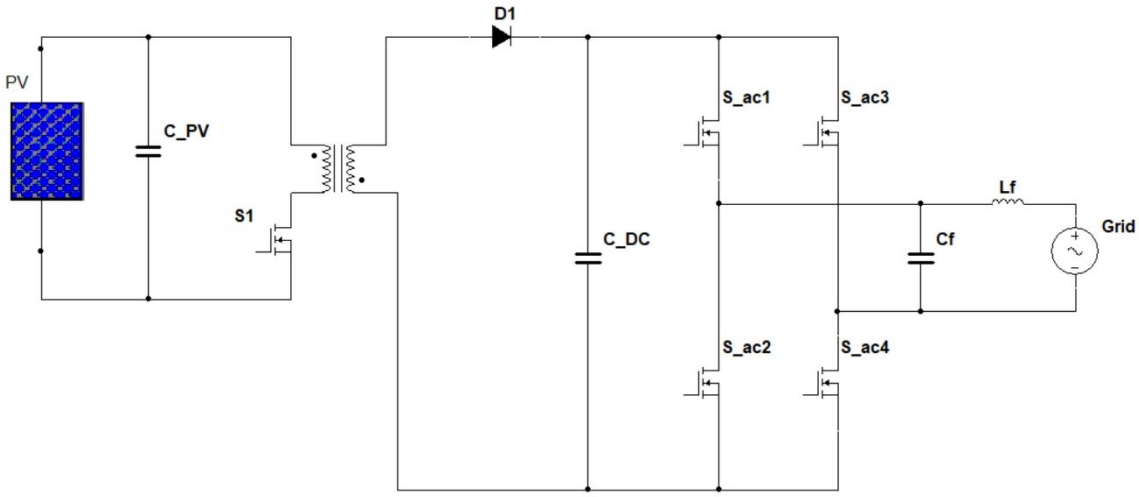


**Figure 4.5 Flyback Inverter Topology with an Electrolytic DC-link Capacitor (Topology 4)**

### 4.3.3 PV-Side Film Capacitor with MII

In the previous topologies, a large capacitor was used so that the inverter would become bulky. However, a film capacitor can also be used to reduce the required capacitor value and inverter size. As seen in equation (4.13), the only way to reduce the required capacitor is to increase the voltage across the capacitor and allow ripple voltage. Hence, in following topologies, the decoupling capacitor was placed on the PV-side by using an auxiliary circuit. The auxiliary circuit is connected between the PV module and micro-inverter so that the pulsating AC power could be decoupled. As a result, the MPP voltage remained constant [42].

The working principle of the power decoupling method with the auxiliary circuit can be found in Figure (4.6); the power decoupling circuit is an auxiliary part and independent from the inverter. This leads to unlimited decoupling capacitor voltage. Since $P_C = C_D V_D \frac{dV_D}{dt}$, increasing $V_D$ or voltage fluctuation $\left(\frac{dV_D}{dt}\right)$ on the decoupling capacitor serves to decrease the capacitor value. While $P_{in}$ is higher than $P_{out}$ in the first mode, it become the reverse during the second stage. This means that an excess or lack of power needs to be stored in the decoupling capacitor. Figure (4.7) shows the power flow directions for both stages. In the first mode ($P_{in}$>$P_{out}$), the output power is transferred from the input power so that the remaining power, $P_{in}$-$P_{out}$, is stored at the decoupling capacitor. In the second stage ($P_{in}$<$P_{out}$), $P_{out}$-$P_{in}$ should have been provided from the stored energy in the decoupling capacitor. In that case, $P_{in}$ is transferred to the secondary side and $P_{out}$-$P_{in}$ is supplied from the decoupling capacitor [51].

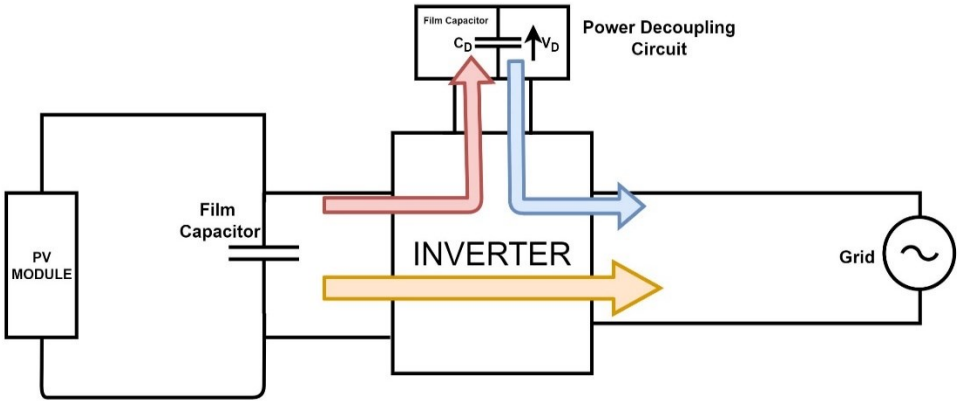


**Figure 4.6 Power Flow of the Power Decoupling Method**

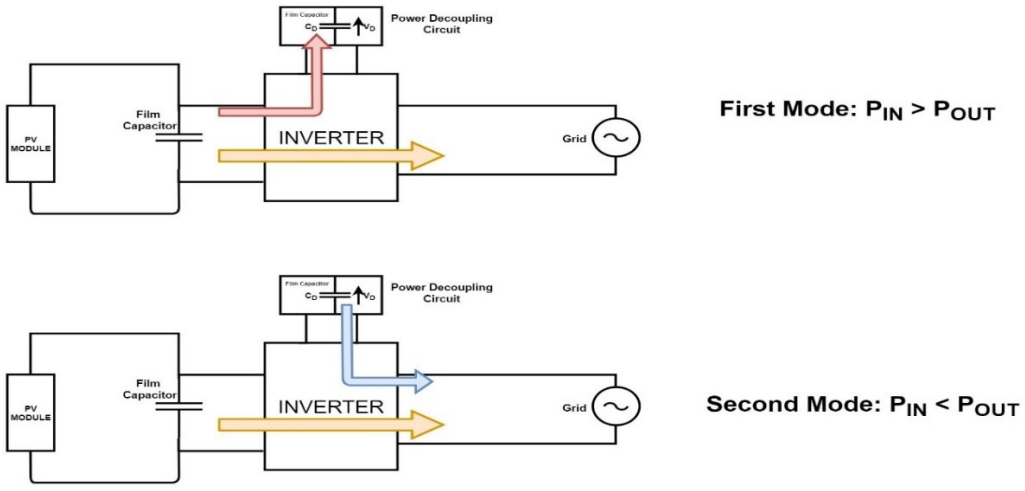


**Figure 4.7 Power Flow for Two Different Modes**

In the topology depicted below, a constant input power from the PV module is first charged the transformer, and then transferred to the decoupling capacitor. Next, it is sent out to the AC grid in a rectified sine wave. Although the process provides a smaller capacitor, the efficiency of the inverter is lower than in the previous topologies [42].

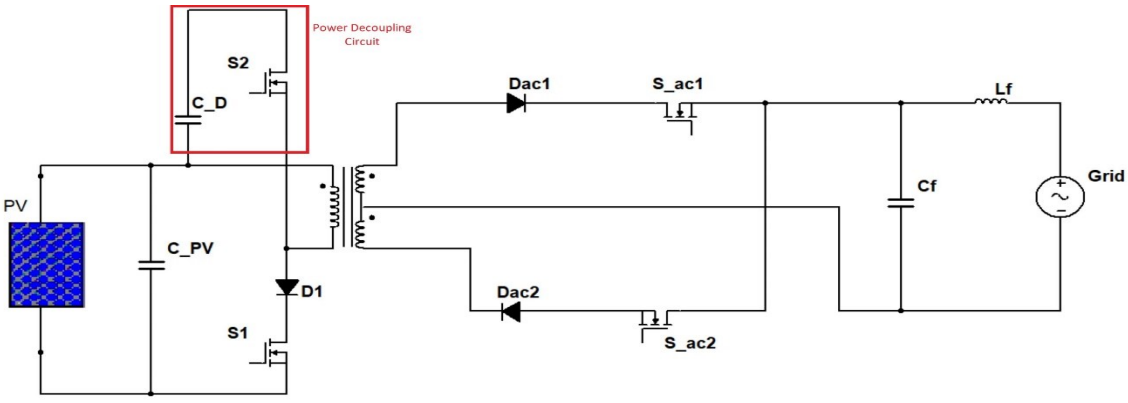


**Figure 4.8 Flyback Inverter with a Film Capacitor (Topology 5)**

Figure (4.9) shows the modified version of Figure (4.8). A dual-switch flyback converter is used to recycle the energy [42]. The difference in this topology is that the energy from the PV module is first charged to the transformer when $S_{SYNC}$ and $S_{BB}$ are ON, synchronically. Then, when $S_{SYNC}$ and $S_{BB}$ are OFF, the energy is transferred to the decoupling capacitor over $D_1$ and $D_2$. Lastly, when $S_1$ and $S_2$ are ON, the energy stored in the decoupling capacitor is transferred to the transformer, and the sinusoidal waveform is supplied to the AC grid.

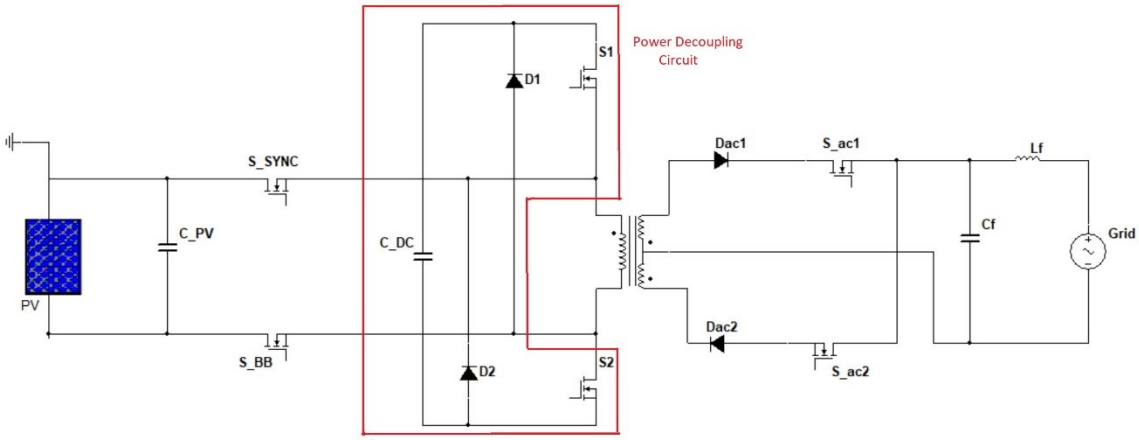


**Figure 4.9 Modified Flyback Inverter with a Film Capacitor (Topology 6)**

Finally, the electrical stress on the capacitor and diode are determined for each circuit. As the equations in Table (4.1) require electrical stress on the capacitor and diode, they are calculated by considering a basic circuit analysis. Table (4.2) shows the voltage stresses on the diode and capacitor.

**Table 4.2 Voltage Stresses of the Components**

| Worst Case Voltage Stresses | | |
|---|---|---|
| | **Diode** | **Capacitor** |
| **Topology 1 (Figure 4.2)** | $V_{D1}= V_{D2}= V_{D3}= V_{D4}=NV_{PV}$ | $V_{decoupling}=V_{OC}$ |
| **Topology 2 (Figure 4.3)** | $V_{D1}= V_{D2}= NV_{PV}+V_{grid\_peak}$ | $V_{decoupling}=V_{OC}$ |
| **Topology 3 (Figure 4.4)** | $V_{D1}= V_{D2}= V_{D3}= V_{D4}=$ $NV_{PV}+V_{DC}$ | $V_{decoupling}=V_{DC}$ |
| **Topology 4 (Figure 4.5)** | $V_{D1}= NV_{PV}+V_{DC}$ | $V_{decoupling}=V_{DC}$ |
| **Topology 5 (Figure 4.8)** | $V_{Dp}=V_{PV}+V_{decoupling}$ $V_{Dac}= NV_{PV}-V_{grid\_peak}$ | $V_{decoupling}= V_{DCmax}$ |
| **Topology 6 (Figure 4.9)** | $V_{Df}=V_{decoupling}-V_{PV}$ $V_{Dac}= NV_{PV}+V_{grid\_peak}$ | $V_{decoupling}= V_{DCmax}$ |

## 4.4 Results

The calculated MTBF values for each component and the whole inverter can be found in Table (4.3-4.4-4.5) for Ankara, Mugla, and Nigde. The calculations were done for the city of Mugla that has the highest failure rate, Nigde that has lowest failure rate and Ankara for comparison. However, although commercial inverter topology has higher

failure rate than modified or special design inverters, there is no big difference among cities as their climatic characteristics are close to each other.

**Table 4.3 MTBFs of Different Inverter Topologies for Ankara**

| Mean Time Between Failures (Million Hours) | | | | | | | | |
|---|---|---|---|---|---|---|---|---|
| | INDIVIDUAL COMPONENTS | | | | | WHOLE INVERTER | | |
| | MOSFETs | Capacitor | Diode | Inductor | Transformer | Min MTBF | Averaged MTBF | Weighted MTBF |
| **Topology 1 (Figure 4.2)** | 0.1187 | 0.2456 | 1.5917 | 6736 | 10.63 | 0.0757 | 0.1924 | 0.1922 |
| **Topology 2 (Figure 4.3)** | 0.2374 | 0.2456 | 0.9196 | 6736 | 10.63 | 0.1057 | 0.2960 | 0.2950 |
| **Topology 3 (Figure 4.4)** | 0.0890 | 0.4193 | 0.3738 | 6736 | 10.63 | 0.0610 | 0.1521 | 0.1515 |
| **Topology 4 (Figure 4.5)** | 0.1425 | 0.4193 | 1.4953 | 6736 | 10.63 | 0.0984 | 0.2430 | 0.2428 |
| **Topology 5 (Figure 4.8)** | 0.1781 | 19.48 | Dac 40.1 / Dp 14.9 | 6736 | 10.63 | 0.1709 | 0.3669 | 0.3675 |
| **Topology 6 (Figure 4.9)** | 0.1187 | 19.48 | Dac 1.79 / Df 20.1 | 6736 | 10.63 | 0.1090 | 0.2407 | 0.2407 |

## Table 4.4 MTBFs of Different Inverter Topologies for Mugla

| Mean Time Between Failures (Million Hours) | | | | | | | | |
|---|---|---|---|---|---|---|---|---|
| | INDIVIDUAL COMPONENTS | | | | | WHOLE INVERTER | | |
| | MOSFETs | Capacitor | Diode | | Inductor | Transformer | Min MTBF | Averaged MTBF | Weighted MTBF |
| **Topology 1 (Figure 4.2)** | 0.1080 | 0.1912 | 1.4221 | | 6327 | 9.99 | 0.0654 | 0.1753 | 0.1752 |
| **Topology 2 (Figure 4.3)** | 0.2161 | 0.1912 | 0.8107 | | 6327 | 9.99 | 0.0893 | 0.2684 | 0.2679 |
| **Topology 3 (Figure 4.4)** | 0.0810 | 0.3264 | 0.3289 | | 6327 | 9.99 | 0.0593 | 0.1384 | 0.1381 |
| **Topology 4 (Figure 4.5)** | 0.1297 | 0.3264 | 1.3155 | | 6327 | 9.99 | 0.0859 | 0.2215 | 0.2215 |
| **Topology 5 (Figure 4.8)** | 0.1621 | 18.62 | Dac 34.45 | Dp 12.96 | 6327 | 9.99 | 0.1555 | 0.3368 | 0.3375 |
| **Topology 6 (Figure 4.9)** | 0.1080 | 18.62 | Dac 1.57 | Df 17.32 | 6327 | 9.99 | 0.0990 | 0.2206 | 0.2207 |

## Table 4.5 MTBFs of Different Inverter Topologies for Nigde

| Mean Time Between Failures (Million Hours) | | | | | | | | |
|---|---|---|---|---|---|---|---|---|
| | INDIVIDUAL COMPONENTS | | | | | WHOLE INVERTER | | |
| | MOSFETs | Capacitor | Diode | | Inductor | Transformer | Min MTBF | Averaged MTBF | Weighted MTBF |
| **Topology 1 (Figure 4.2)** | 0.1252 | 0.2801 | 1.7455 | | 6978 | 11.01 | 0.0818 | 0.1931 | 0.1929 |
| **Topology 2 (Figure 4.3)** | 0.2505 | 0.2801 | 1.0058 | | 6978 | 11.01 | 0.1156 | 0.2970 | 0.2964 |
| **Topology 3 (Figure 4.4)** | 0.0939 | 0.4782 | 0.4087 | | 6978 | 11.01 | 0.0655 | 0.1526 | 0.1522 |
| **Topology 4 (Figure 4.5)** | 0.1503 | 0.4782 | 1.6350 | | 6978 | 11.01 | 0.1058 | 0.2439 | 0.2438 |
| **Topology 5 (Figure 4.8)** | 0.1879 | 19.87 | Dac 43.67 | Dp 16.33 | 6978 | 11.01 | 0.1802 | 0.3684 | 0.3685 |
| **Topology 6 (Figure 4.9)** | 0.1252 | 19.87 | Dac 1.95 | Df 21.83 | 6978 | 11.01 | 0.1152 | 0.2416 | 0.2415 |

The topologies that have higher MTBF value mean that the probability of the topology work and complete successfully all necessary job during its useful lifetime [37]. In the first four inverter topologies, a large capacitance necessity was provided via a large electrolytic aluminum capacitor. However, when an electrolytic aluminum capacitor is exposed to a high-temperature environment in the summer, its life is shortened and, consequently, the inverter lifetime is reduced. Thus, as the electrolytic aluminum capacitor is not the best choice in terms of size and lifetime, Topology 5 and Topology 6 used film capacitors instead of aluminum capacitors. It was expected that replacing an aluminum capacitor with a film capacitor improves the lifetime of the component and the entire module as film capacitor has long lifetime individually. However, as MOSFETs failure rate is higher than capacitor, MOSFETs become limited component in the circuit. Also, using a film capacitor creates energy storage issue. Film capacitors have lower capacitance in terms of energy storage; thus, the advantage of a longer lifetime can be eliminated by this energy storage issue. Table (4.6) shows the datasheets information for the capacitors used in this research, and the information employed to calculate their lifetimes and levels of energy storage [52, 53, and 54].

**Table 4.6 Parameter Comparison of Used Capacitors**

| | PV-side electrolytic aluminum capacitor | DC-link electrolytic aluminum capacitor | PV-side film capacitor |
|---|---|---|---|
| **Capacitance(C)** | 18000 µF | 120 µF | 100 µF |
| **Rated Voltage ($V_{rated}$)** | 50 Volt | 450 Volt | 450 Volt |
| **Reference Temperature($T_r$)** | 85 °C | 105 °C | 85 °C |
| **Base Lifetime ($L_b$)** | 3,000 Hour | 10,000 Hour | 100,000 Hour |
| **Cost / Stored Energy ($/Joule)** | **0.236 $/Joule** | **0.468 $/Joule** | **2.32 $/Joule** |

Figure (4.10) lists the lifetimes of the capacitors used in this research, which were derived by applying the values in Table (4.6) to equation (4.14) [55]. Equation (4.14) shows that a lifetime projection is not affected by capacitance value, so the same operating conditions give the same estimated lifetime for any decoupling technique [55].

$$Lifetime = \frac{L_b \left( 2^{\frac{\left(T_r - T\right)}{10}} \right)}{\left( \frac{V_{op}}{V_{rated}} \right)^{2.6087 \left( \frac{V_{op}}{V_{rated}} + 0.5167 \right)}} \tag{4.14}$$

$$\begin{cases} V_{op}, & \text{Operating Voltage}[\text{V}] \\ V_{rated}, & \text{Rated Voltage}[\text{V}] \\ T, & \text{Operating Temperature}[^{\circ}\text{C}] \\ T_r, & \text{Reference Temperature}[^{\circ}\text{C}] \end{cases}$$

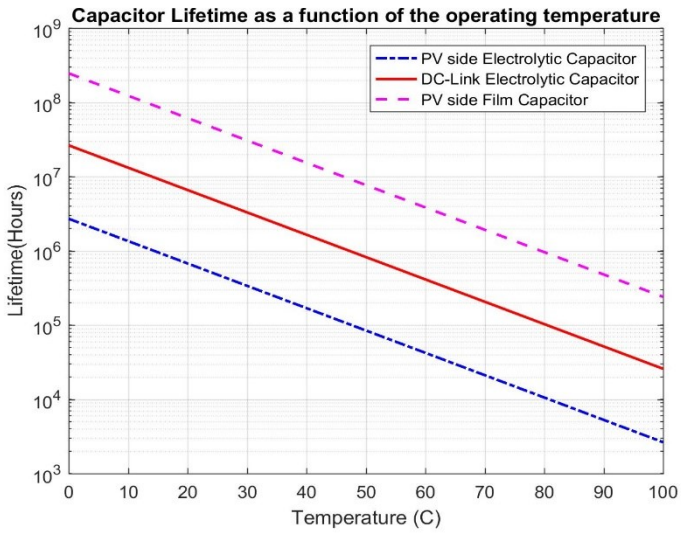


**Figure 4.10 Capacitor Lifetime as a Function of the Operating Temperature**

Tables (4.3-4.5) and (4.6) emphasize the following critical points.

- Although it is difficult to determine if one of these six topologies is better than the others, it is possible to affirm that number of components directly affects the failure rate. For example, while comparing Topology 1 and Topology 2, it can be seen that Topology 2 has a lower failure rate because it has fewer components.

- Temperature factor ($\pi_T$) contributes the most to failure rate. The Figure (4.11) shows the MTBFs as a function of the operating temperature. The effect of the temperature is such that as the temperature increases, the MTBF decreases thus, the failure rate increases. Hence, thermal design is an aspect that should be considered by designers.

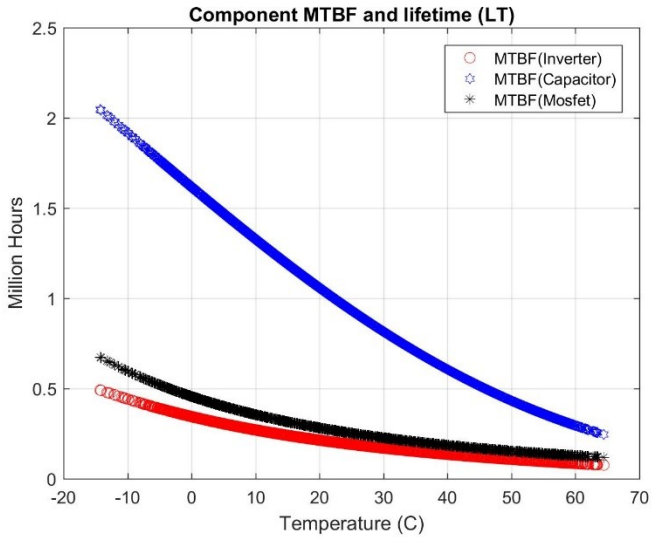


**Figure 4.11 MTBFs as a Function of the Operating Temperature**

- The Figure (4.12) illustrates the contributions of all of the components to the failure rate in Topology 1. This figure indicates that the transformer and inductor did not make a significant contribution to the failure rate.

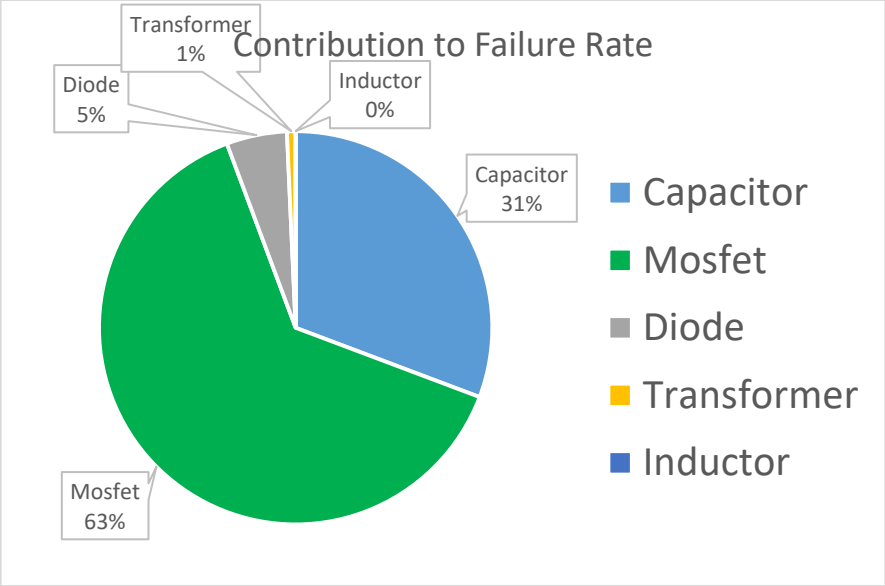


**Figure 4.12 Component Contributions to the Failure Rate**

- It can be seen that the MOSFET failure rate is higher than the others, so ideally circuits should have fewer MOSFETs. Hence, designing new control techniques with fewer MOSFETs would decrease the failure rate. The Figure (4.13) shows the MOSFETs MTBF for different cities and different inverter topologies. The commercial inverter topologies which are topology 1 and topology 3 have a higher failure rate. Additionally, it shows that different cities failure rates are close to each other.

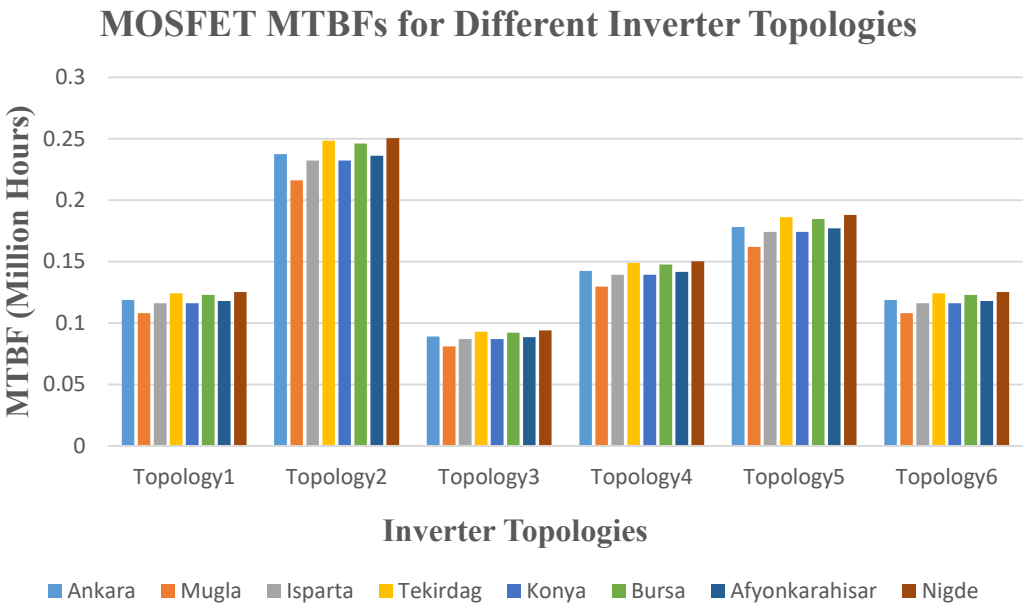


**Figure 4.13 MOSFET MTBFs for Different Inverter Topologies**

- Although capacitors are considered the most failure-prone components, capacitors and MOSFETs have the highest failure rates among all components. The equation for the capacitor shows that its failure rate is affected by voltage stress. Hence, component stress reduction would improve the reliability of the components, and the entire inverter. One means of reduction would be to connect equal-value capacitors in a series, so that the voltage is reduced. The Figure (4.14) illustrates the impact of electrical stress factors on the MTBF for capacitors. As can be seen, electrical stress is directly proportional to the failure rate.

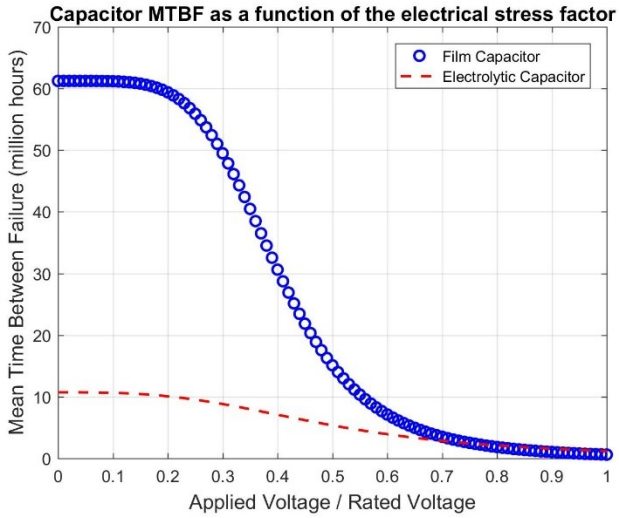


**Figure 4.14 Capacitor MTBFs as a Function of the Electrical Stress Factor**

- The MOSFET failure rate depends on the temperature and power harnessed by the PV module. Figure (4.15) shows the power ratings effect on the MTBF.

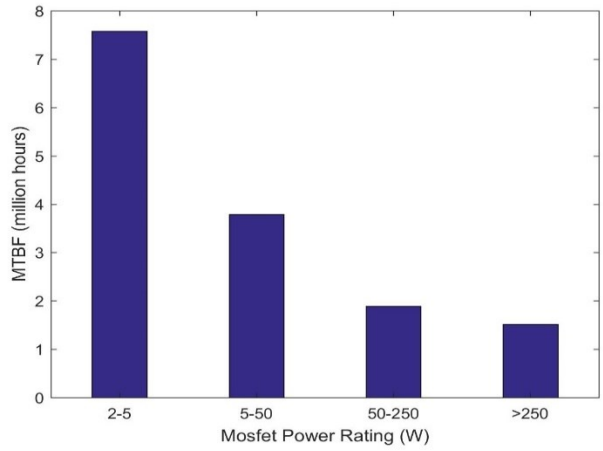


**Figure 4.15 Power Rating Effects on MOSFET MTBFs**

- The Figure (4.16) shows the electrical stress factor on diode. The failure rate is directly proportional to voltage stress. It helps to choose a diode when design a circuit.

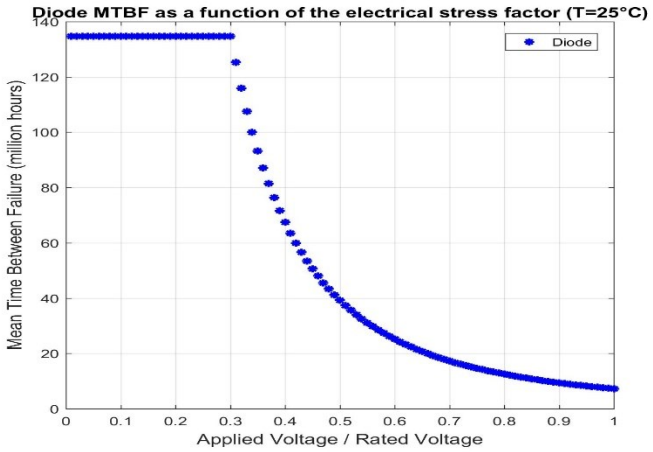


**Figure 4.16 Diode MTBFs as a Function of the Electrical Stress Factor**

- Some topologies could yield MTBFs lower than 130,000 hours (almost 15 years). This is an important criterion for people who intend to install the PV system in a hot weather area. Hot weather and sunshine do not necessarily mean the more solar energy. Such conditions also bring reliability problems. Hence, it is necessary to conduct a cost-benefit analysis before installing a module in this type of climate.
- Using a film capacitor instead of an electrolytic aluminum capacitor was expected to decrease the system failure rate because film capacitors are more reliable than other components. However, although film capacitors have longer lifetimes individually, they do not affect the whole-system failure rate significantly, since the

MOSFET failure rate is a limited factor. Also, when considering their lower energy storage capacity and higher cost, film capacitors are not a practical solution, even if we can eliminate MOSFET factor.

- While comparing the cities, Mugla and Nigde have the highest and lowest failure rates for all inverter topologies, respectively. Figure (4.17) shows the insolation and average temperature map together. It is seen that Nigde and Mugla have different climatic characteristic while their solar characteristics are similar.

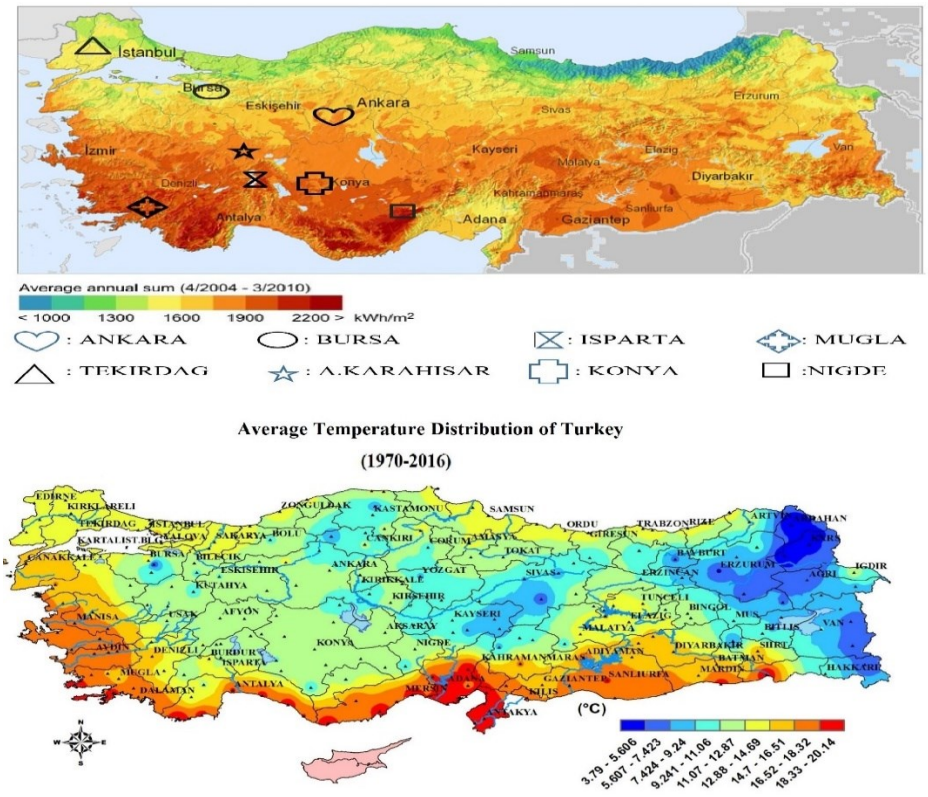


**Figure 4.17 Direct Normal Insolation and Average Temperature Map of Turkey, Adapted from [13, 15]**

The Figure (4.18) shows the MOSFET MTBFs which has the highest failure rate for Nigde and Mugla for 6 different topologies.

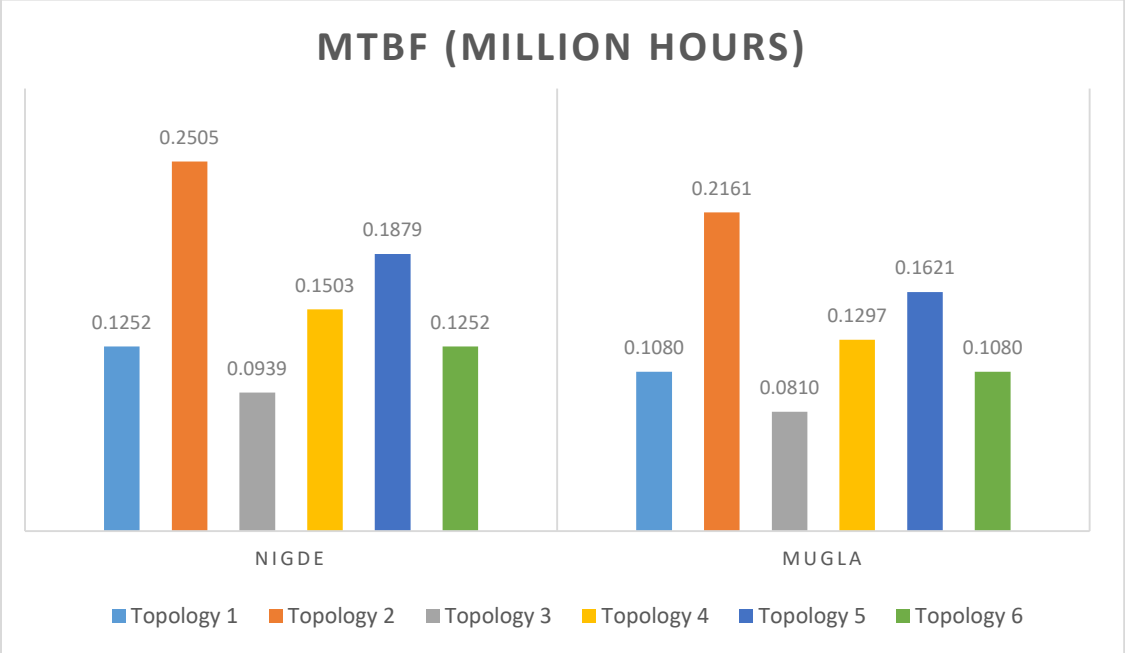


**Figure 4.18 MOSFET MTBFs for Nigde and Mugla**

As can be seen in above figure, MOSFET MTBFs are between 0.0810 million hours to 0.2505 million hours. They correspond to 9 years to 25 years.

- The same analysis can be done for capacitors. Integrated microinverter needs at renew during the PV module lifetime because of the electrolytic aluminum capacitor.

Hence, though the PV module lifetime is almost 20 to 25 years, the microinverter can be needed to renew at least two times because of the MOSFET failure during system lifespan. As a result, it brings shutdown and renewal cost.

All the results help us to decrease the failure rate when create a design. Some tips are listed in below.

- It is advised that use possible least number of components since the number of components has an effect on failure rate.
- The created design needs to a cooling system such as heat sink, fans, and heat spreaders.

## 4.5 Conclusion

The thermal and electrical model outputs were applied to the reliability calculation, so that the MTBF could be found for the MOSFETs, capacitor, diodes, inductor, and transformer at each operating point. Then, the minimum, averaged, and weighted MTBFs were calculated for each whole inverter topology. This process was followed for all the studied cities. The MTBFs for each component and the whole inverter were different for different cities, in response to their variable climatic conditions. As a result, the capacitor and MOSFETs were found to be the two most vulnerable components in the candidate micro-inverter topologies.

# 5. CONCLUSION

In this thesis, thermal modeling was developed to calculate PV module temperatures, after considering meteorological parameters, heat transfer, and energy balance. The results of calculated PV module temperatures showed that maximum PV module temperature is different for evaluated cities. Unfortunately, there is no meteorological data for other cities to calculate PV module temperature. However, results of calculated cities gave an idea that as maximum PV module temperature is changed by region and installation parameters (i.e., roof and tilt angle), the developed model helps us to estimate maximum PV module temperature. The maximum PV module temperature has an impact on module output voltage as calculated in chapter 3. The output voltage of the PV module is crucial as it effects the voltage stress on power electronic components. As thermal model results are different for different cities, voltage stress on components is varied for different locations. After the module temperature and output voltage were obtained, the reliability calculations were completed using the MIL 217 reliability handbook. The reliability results showed the most failure prone component in the candidate micro-inverter and expected lifetime for different cities. Interestingly, commercial inverter topologies in analyzed topologies were found most failure prone inverters for all evaluated cities.

As a result, this thermal model can be applied to anywhere in the world, and it helps to determine failure rates of power electronic components in different climatic regions. Thus, specific inverters can be designed to work longer life in those different

climatic areas. In addition to these, the model is suitable to change PV module parameters and installation parameters. Hence, parameter effects are observed easily. It eliminates the expensive and time-consuming test beds.

# REFERENCES

[1] M. Ačanski, J. Popović-Gerber and J. A. Ferreira, "Thermal modeling of the module integrated DC-DC converter for flexible thin-film PV modules," Proceedings of the 2011 14th European Conference on Power Electronics and Applications, Birmingham, 2011, pp. 1-10.

[2] World Energy Council. [Online].
Available: https://www.worldenergy.org/data/resources/resource/solar/.
[Accessed on February 8, 2018].

[3] B. Zhao et al., "Photothermal performance of an amorphous silicon photovoltaic panel integrated in a membrane structure," Journal of Physics D: Applied Physics, vol. 49, no. 39, 2016.

[4] Jordan, D. C. and Kurtz, S. R. (2013), Photovoltaic Degradation Rates—an Analytical Review. Prog. Photovolt: Res. Appl., 21: 12–29.

[5] H. Oldenkamp, I. J. de Jong, C. W. A. Baltus, S. A. M. Verhoeven and S. Elstgeest, "Reliability and accelerated life tests of the AC module mounted OKE4 inverter," Conference Record of the Twenty Fifth IEEE Photovoltaic Specialists Conference - 1996, Washington, DC, 1996, pp. 1339-1342.

[6] W. Knaupp, "Operation behaviour of roof installed photovoltaic modules," Conference Record of the Twenty Fifth IEEE Photovoltaic Specialists Conference - 1996, Washington, DC, 1996, pp. 1445-1448.

[7] M. Mattei, G. Notton, C. Cristofari, M. Muselli, and P. Poggi, "Calculation of the polycrystalline PV module temperature using a simple method of energy balance," Renewable Energy, vol. 31, no. 4, pp. 553-567, 2006.

[8] H. Fahmy, "Mathematical and numerical model for PV cell steady state temperature distribution," in Proc. Int. Solar Energy Conf., Albuquerque, NM, USA, 1998, pp.225-231.

[9] Jones, A.D. & Underwood, C.P.. (2001). A Thermal model for photovoltaic systems. Solar Energy. 70. 349-359.

[10] Z. H. Lu and Q. Yao, "Energy analysis of silicon solar cell modules based on an optical model for arbitrary layers," Solar Energy, vol. 81, no. 5, pp. 636-647, 2007.

[11] D. Torres Lobera and S. Valkealahti, "Dynamic thermal model of solar PV systems under varying climatic conditions," Solar Energy, vol. 93, pp. 183-194, 2013.

[12] JRC Photovoltaic Geographical Information System (PVGIS) – European Commission, "JRC Photovoltaic Geographical Information System (PVGIS) European Commission, " [Online]. Available: http://re.jrc.ec.europa.eu/. [Accessed on December 15, 2017].

[13] Solargis.com. (2018). Bankable solar data for better decisions. [Online]. Available: https://solargis.com/. [Accessed on December 10, 2017].

[14] TEİAŞ, "Turkish Electricity Transmission Company- Türkiye Elektrik İletim A.Ş," [Online]. Available: https://www.teias.gov.tr/. [Accessed on January 8, 2018].

[15] Turkish State Meteorological Service. [Online]. Available: https://mgm.gov.tr. [Accessed on August 10, 2017].

[16] "Hanwha Q-Cells to inaugurate Turkey panel factory in November," PV Magazine, August 15, 2017. [Online],
Available: https://www.pv-magazine.com/2017/08/15/hanwha-q-cells-to-inaugurate-its-turkey-panel-factory-in-november/. [Accessed on February 15, 2018].

[17] "Turkey's biggest solar plant to be built by Kalyon-Hanwha Co.," Daily Sabah Energy, March 20, 2017. [Online],
Available: https://www.dailysabah.com/energy/2017/03/20/turkeys-biggest-solar-plant-to-be-built-by-kalyon-hanwha-co. [Accessed on February 15, 2018].

[18] United State Dep. of Def., "Military Handbook MIL-HDBK-217F, Reliability Prediction of Electronic Equipment," Washington, DC, 1991.

[19] E. Skoplaki and J. A. Palyvos, "Operating temperature of photovoltaic modules:A
survey of pertinent correlations," Renewable Energy, vol. 34, no. 1, pp. 23-29, 2009.

[20] R. S. Balog, Yingying, Kuai, Uhrhan, G., "A Photovoltaic Module Thermal Model Using Observed Insolation and Meteorological Data to Support a Long Life, Highly Reliable Module-integrated Inverter Design by Predicting Expected Operating Temperature," in IEEE Energy Conversion Congress and Exposition, ECCE, 2009, pp. 3343-3349.

[21] B. Zhao, W. Chen, J. Hu, Z. Qiu, Y. Qu, and B. Ge, "A thermal model for amorphous silicon photovoltaic integrated in ETFE cushion roofs," Energy Conversion and Management, vol. 100, pp. 440-448, 2015.

[22] D. Torres-Lobera, "Modeling and Analysis of the Operation of PV Power Generators under Varying Atmospheric Conditions," PhD thesis, Tampere University of Technology, Tampere, 2014.

[23] H. Assila, E. Essadiqi, M. Faqir, M. Meziane, F. Ghanameh and S. Ahzi, "Numerical simulation of photovoltaic panel thermal condition under wind convection," 2016 International Renewable and Sustainable Energy Conference (IRSEC), Marrakech, 2016, pp. 653-658.

[24] Republic of Turkey Ministry of Forestry and Water Affairs Meteorological Data Information Sales and Presentation System. [Online]. Available: https://mevbis.mgm.gov.tr/mevbis/ui/index.html#/Workspace. [Accessed on August 10, 2017].

[25] G. Mittelman, A. Alshare, and J. H. Davidson, "A model and heat transfer correlation for rooftop integrated photovoltaics with a passive air cooling channel," Solar Energy, vol. 83, no. 8, pp. 1150-1160, 2009.

[26] R. Tang, Y. Etzion, and I. A. Meir, "Estimates of clear night sky emissivity in the Negev Highlands, Israel," Energy Conversion and Management, vol. 45, no. 11-12, pp. 1831-1843, 2004.

[27] Martin, M., Berdahl, P., 1984. Characteristics of infrared sky radiation in the United States. Solar Energy 33 (3–4), 321–336.

[28] D. Torres-Lobera and S. Valkealahti, "Inclusive dynamic thermal and electric

simulation model of solar PV systems under varying atmospheric conditions," Solar Energy, vol. 105, pp. 632-647, 2014.

[29] Çengel, Y. (1998). Heat transfer : A practical approach (Schaum's outline series in mechanical engineering). Boston, Mass.: WBC McGraw-Hill.

[30] Jie Ji, Hua Yi, Wei He, Gang P, Jianping L, Bin J. Modeling of a novel Trombe wall with PV cells. Building and Environment 2007;42:1544–52.

[31] General Directorate of Renewable Energy, [Online]. Available: http://www.eie.gov.tr [Accessed on January 1,2018].

[32] Hanwha Q Cells Corporation, "QCELLS Q.PRO BFR-G4 265 Watt PV Module", 2013.

[33] Y. Mahmoud, W. Xiao and H. H. Zeineldin, "A Simple Approach to Modeling and Simulation of Photovoltaic Modules," in IEEE Transactions on Sustainable Energy, vol. 3, no. 1, pp. 185-186, Jan. 2012.

[34] H. Bellia, R. Youcef, M. Fatima, "A detailed modeling of photovoltaic module using MATLAB, NRIAG Journal of Astronomy And Geophysics, " vol. 3 n. 1, June 2014, pp. 53–61.

[35] S. Bal, A. Anurag and B. C. Babu, "Comparative analysis of mathematical modeling of Photo-Voltaic (PV) array," 2012 Annual IEEE India Conference (INDICON), Kochi, 2012, pp. 269-274.

[36] M. Azzouzi, D. Popescu, M. Bouchahdane. “Modeling of Electrical Characteristics of Photovoltaic Cell.” Journal of Clean Energy Technologies Vol.4, No.6, 414-419, 2016.

[37] S.Harb, "Single-Phase Inverter and Rectifier for High-Reliability Applications," PhD thesis, Texas A&M University, College Station, Texas, 2014.

[38] E. D. Dunlop, D. Halton and H. A. Ossenbrink, "20 years of life and more: where is the end of life of a PV module?," Conference Record of the Thirty-first IEEE Photovoltaic Specialists Conference, 2005., 2005, pp. 1593-1596.

[39] S. J. Castillo, R. S. Balog and P. Enjeti, "Predicting capacitor reliability in a module-integrated photovoltaic inverter using stress factors from an environmental usage model," North American Power Symposium 2010, Arlington, TX, 2010, pp. 1-6.

[40] S. Harb and R. S. Balog, "Reliability of Candidate Photovoltaic Module-Integrated-Inverter (PV-MII) Topologies—A Usage Model Approach," in IEEE Transactions on Power Electronics, vol. 28, no. 6, pp. 3019-3027, June 2013.

[41] M. Catelani, L. Ciani, G. Graditi, and G. Adinolfi, "Measurement and comparison of reliability performance of photovoltaic power optimizers for energy production," Metrol. Meas. Syst., vol. 17, no. 4, pp. 139–152, 2015.

[42] H. Hu, S. Harb, N. H. Kutkut, I. Batarseh, and Z. J. Shen, "A review of power decoupling techniques for microinverters with three different decoupling capacitor locations in PV systems," IEEE Trans. Power Electron., vol. 28, no. 6, pp. 2711–2726, Jun. 2013.

[43] M.Mirjafari, "Automated Synthesis Tool for Design Optimization of Power Electronic Converters," PhD thesis, Texas A&M University, College Station, Texas, 2013.

[44] S. Harb, H. Hu, N. Kutkut, I. Batarseh and Z. J. Shen, "A three-port Photovoltaic (PV) micro-inverter with power decoupling capability," 2011 Twenty-Sixth Annual IEEE Applied Power Electronics Conference and Exposition (APEC), Fort Worth, TX, 2011, pp. 203-208.

[45] S. B. Kjaer, J. K. Pedersen and F. Blaabjerg, "A review of single-phase grid-connected inverters for photovoltaic modules," in IEEE Transactions on Industry Applications, vol. 41, no. 5, pp. 1292-1306, Sept.-Oct. 2005.

[46] Q. Li and P. Wolfs, "A Review of the Single Phase Photovoltaic Module Integrated Converter Topologies With Three Different DC Link Configurations," in IEEE Transactions on Power Electronics, vol. 23, no. 3, pp. 1320-1333, May 2008.

[47] L. mol K Johny and T. K. Jose Sebastian, "A flyback DCM DC-AC converter for PV applications," 2013 Annual International Conference on Emerging Research Areas and 2013 International Conference on Microelectronics, Communications and Renewable Energy, Kanjirapally, 2013, pp. 1-6.

[48] A. C. Kyritsis, E. C. Tatakis and N. P. Papanikolaou, "Optimum Design of the Current-Source Flyback Inverter for Decentralized Grid-Connected Photovoltaic Systems," in IEEE Transactions on Energy Conversion, vol. 23, no. 1, pp. 281-293, March 2008.

[49] G. C. Christidis, A. C. Nanakos and E. C. Tatakis, "Analysis of a Flyback Current Source inverter under hybrid DCM-BCM operation," 2015 17th European Conference on Power Electronics and Applications (EPE'15 ECCE-Europe), Geneva, 2015, pp. 1 10.

[50] D. C. Martins and R. Demonti, "Grid connected PV system using two energy processing stages," Conference Record of the Twenty-Ninth IEEE Photovoltaic Specialists Conference, 2002., 2002, pp. 1649-1652.

[51] F. Shinjo, K. Wada and T. Shimizu, "A Single-Phase Grid-Connected Inverter with a Power Decoupling Function," 2007 IEEE Power Electronics Specialists Conference, Orlando, FL, 2007, pp. 1245-1249.

[52] Cornell Dubilier, Aluminum Electrolytic Capacitors, [Online]. Available: https://www.mouser.com/ds/2/88/SLPX-32478.pdf, [Accessed on January 8, 2018].

[53] Nichion, Aluminum Electrolytic Capacitors, [Online]. Available: https://www.mouser.com/ds/2/293/e-lgr-884112.pdf, [Accessed on January 8, 2018].

[54] Kemet Electronic Components, Film Capacitors [Online]. Available: https://www.mouser.com/ds/2/212/KEM_F3046_C4AE_RADIAL-1107630.pdf, [Accessed on January 8, 2018].

[55] S. Harb, M. Mirjafari and R. S. Balog, "Ripple-Port Module-Integrated Inverter for Grid-Connected PV Applications," in IEEE Transactions on Industry Applications, vol. 49, no. 6, pp. 2692-2698, Nov.-Dec. 2013.

# APPENDIX A

## THERMAL MODELING RESULTS

## SIMULATED RESULTS FOR CITY OF MUGLA

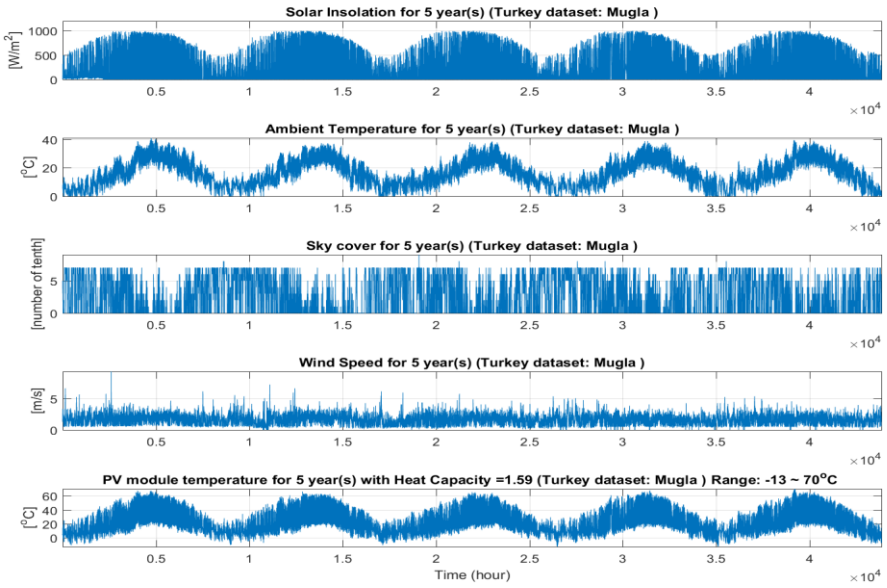


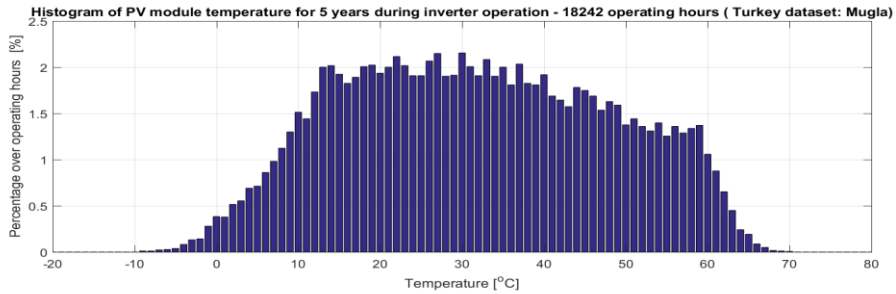


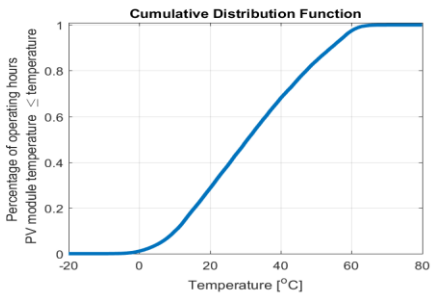


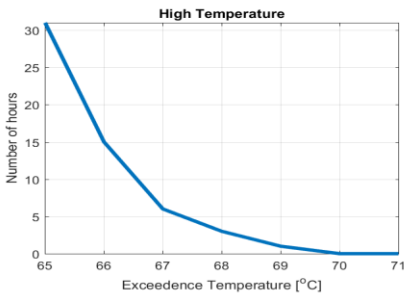

SIMULATED RESULTS FOR CITY OF ISPARTA

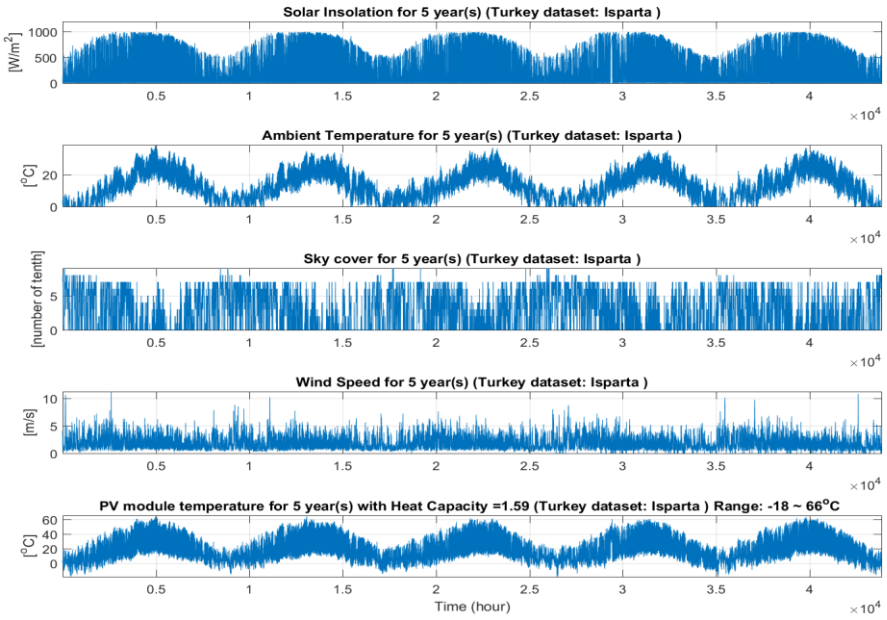


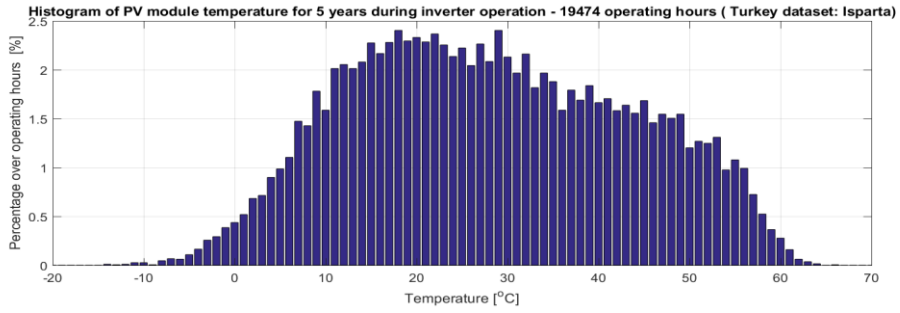


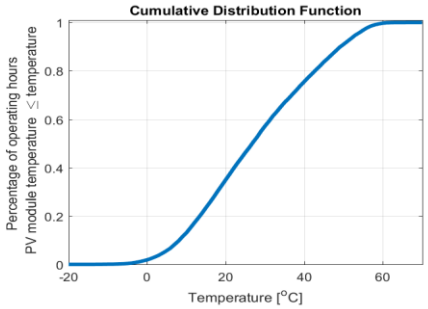


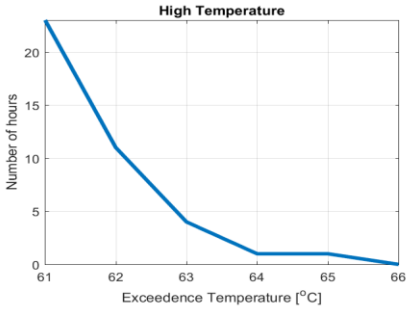

SIMULATED RESULTS FOR CITY OF TEKIRDAG

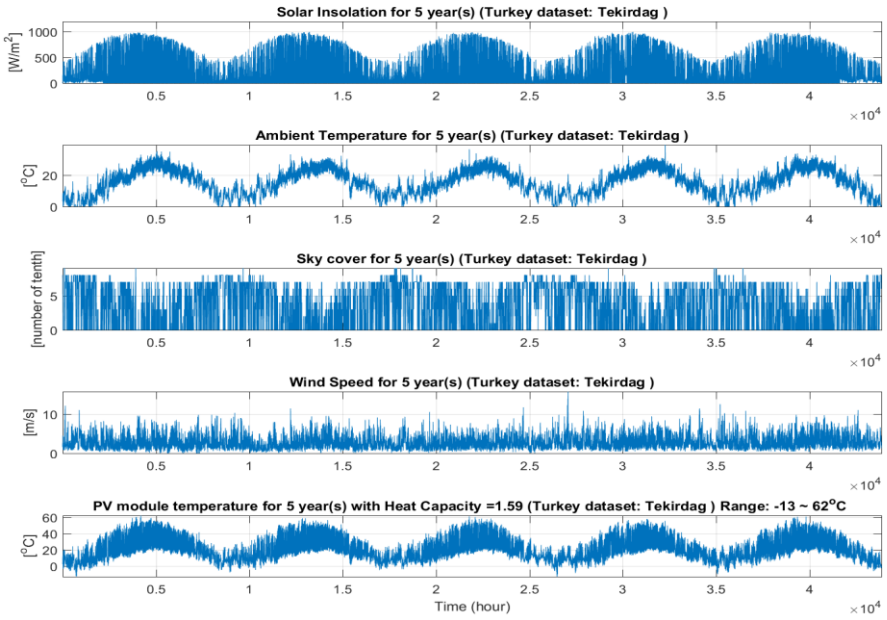


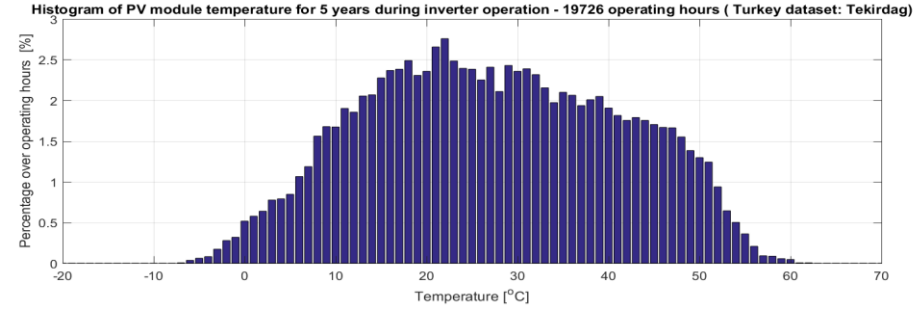


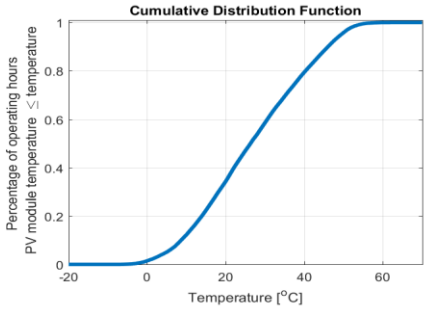


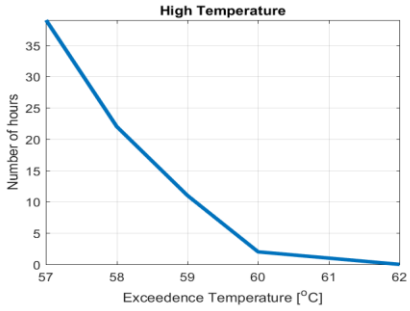

SIMULATED RESULTS FOR CITY OF KONYA

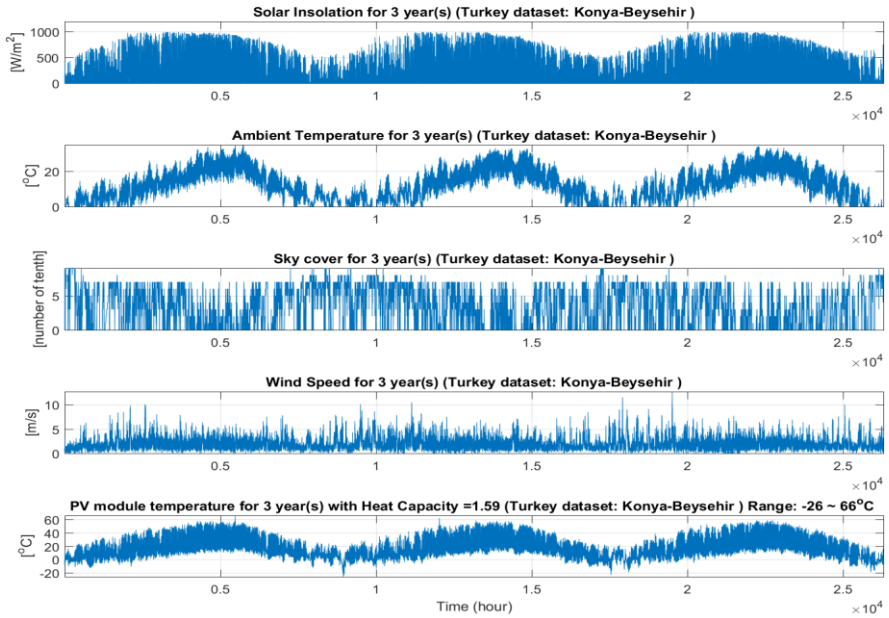


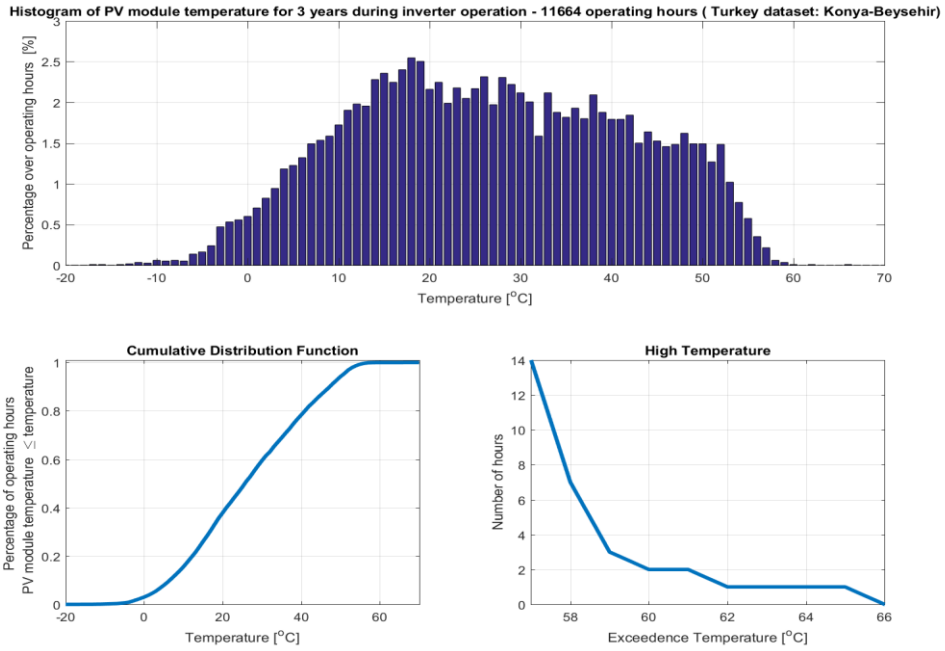

SIMULATED RESULTS FOR CITY OF BURSA

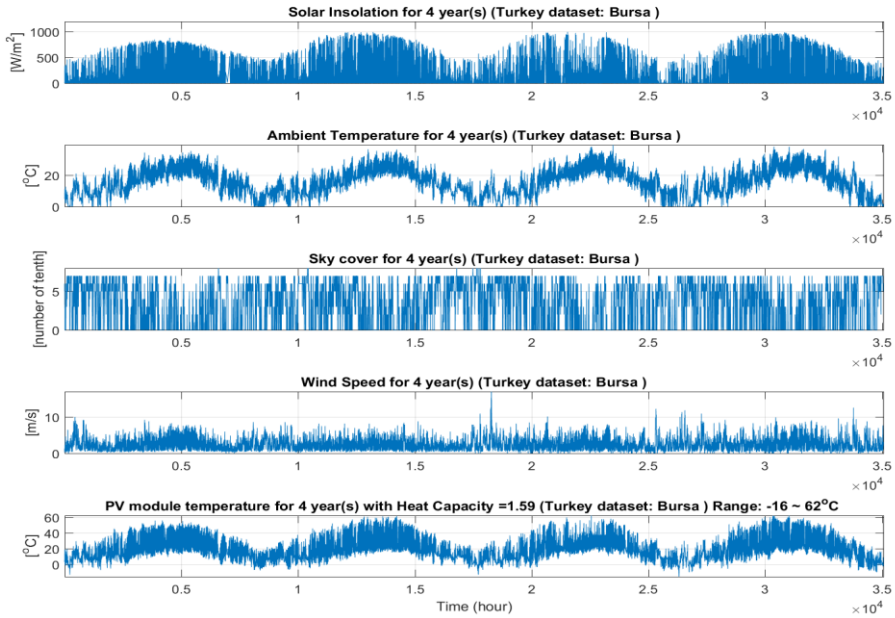


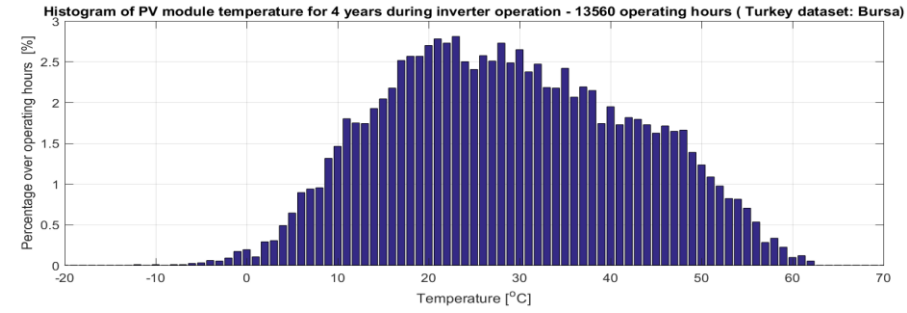


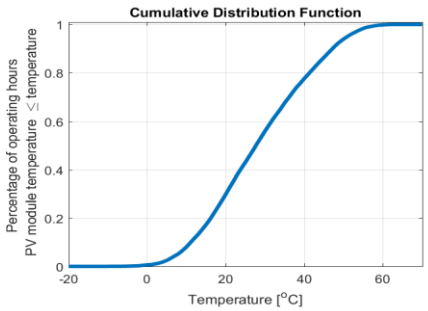


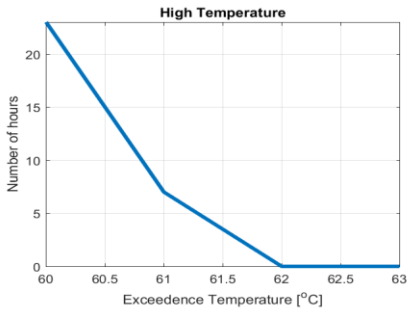

SIMULATED RESULTS FOR CITY OF AFYONKARAHISAR

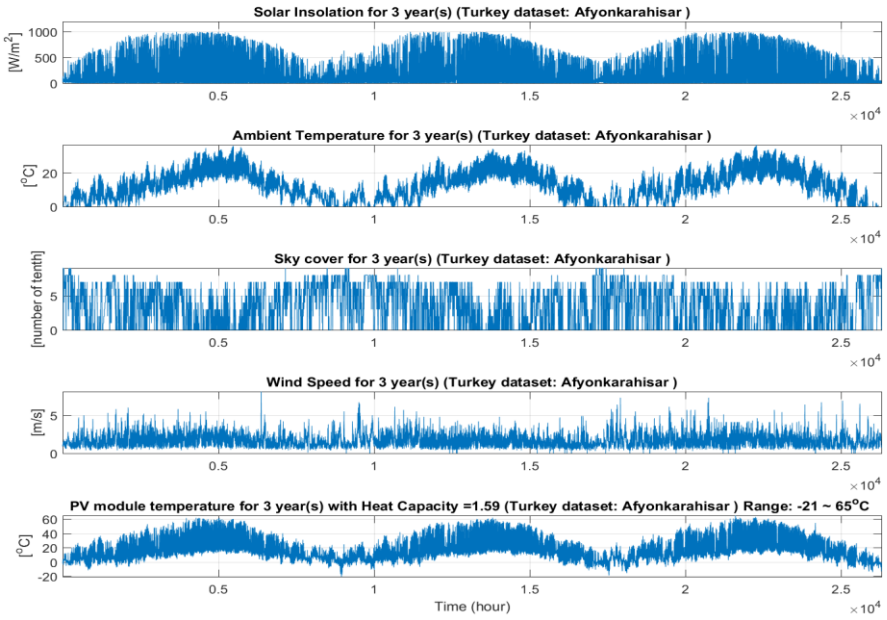


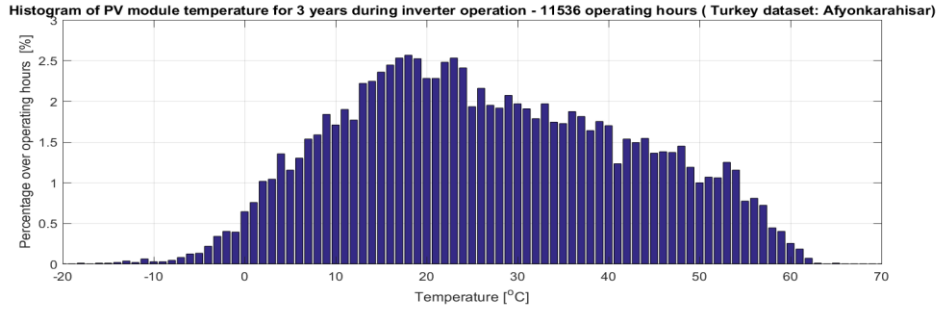


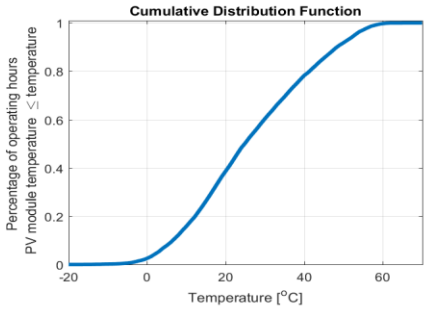


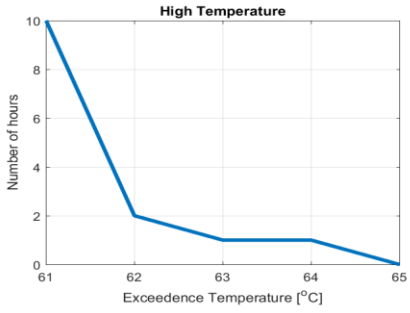

SIMULATED RESULTS FOR CITY OF NIGDE

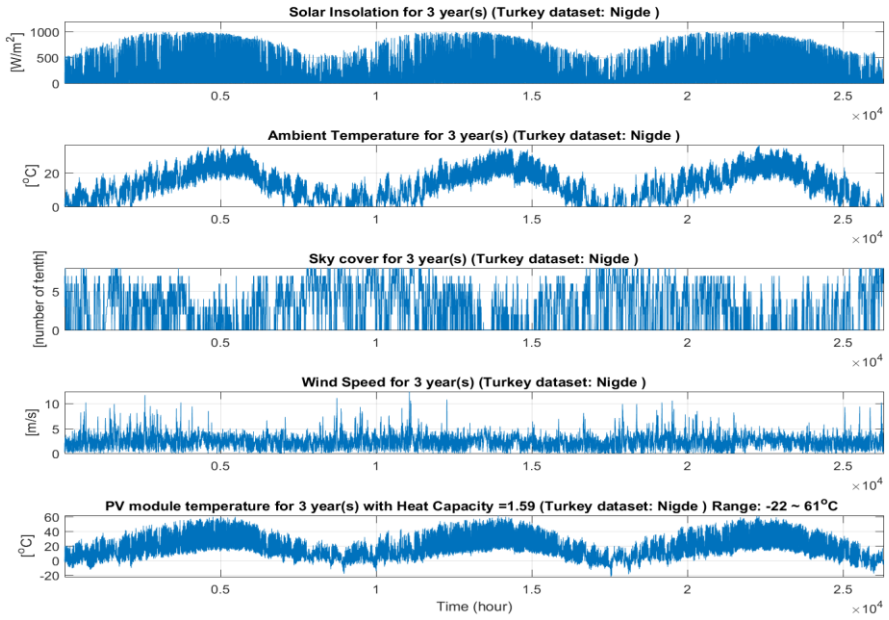


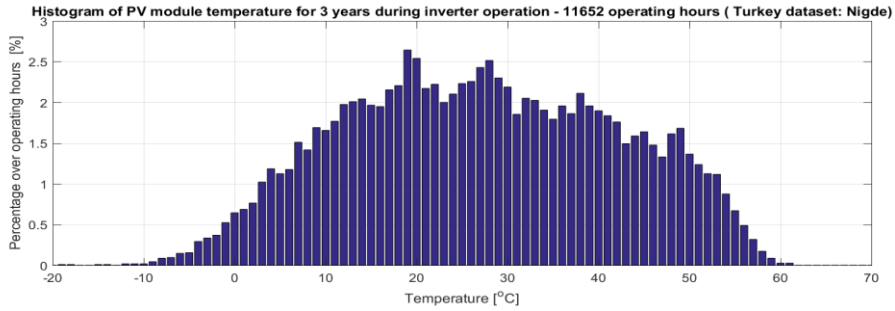


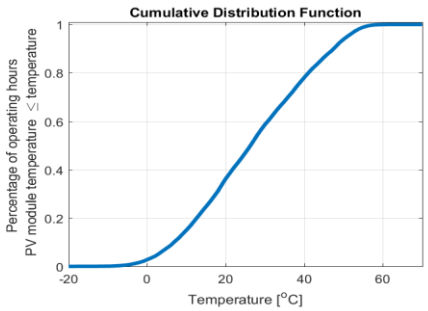


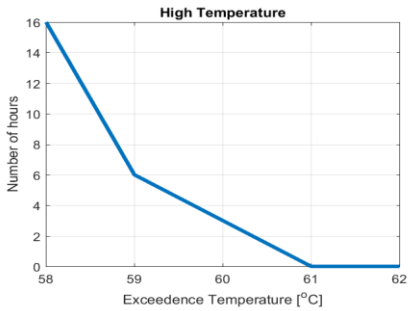

# APPENDIX B

## ELECTRICAL MODEL RESULTS

### OUTPUT VOLTAGE HISTOGRAM FOR CITY OF MUGLA

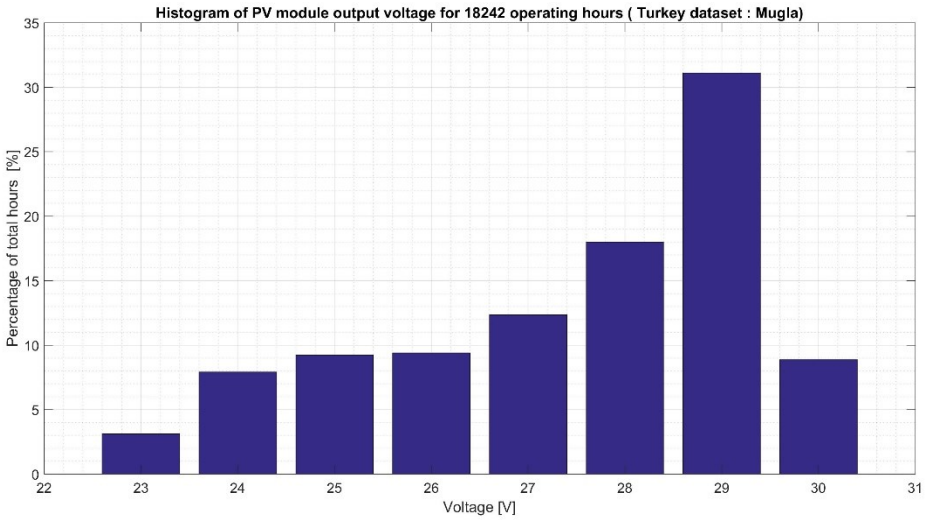


### OUTPUT VOLTAGE HISTOGRAM FOR CITY OF ISPARTA

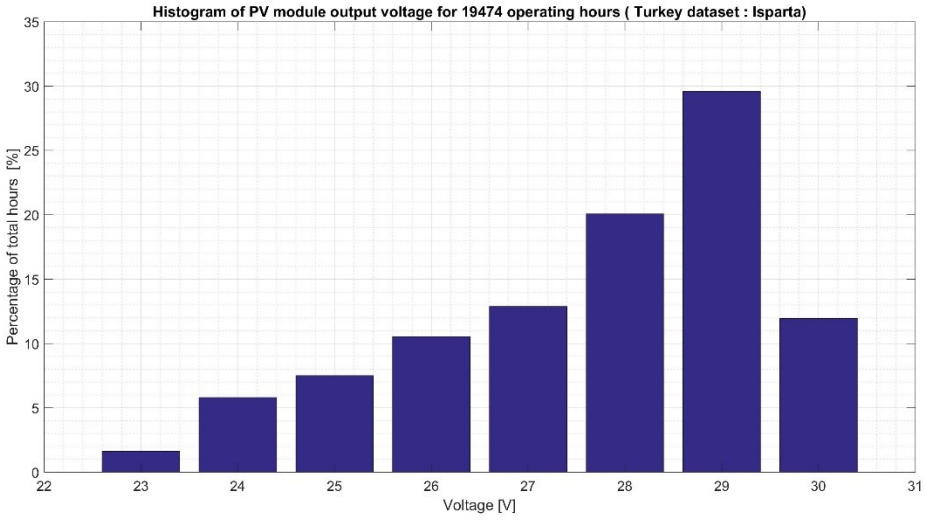

OUTPUT VOLTAGE HISTOGRAM FOR CITY OF TEKIRDAG

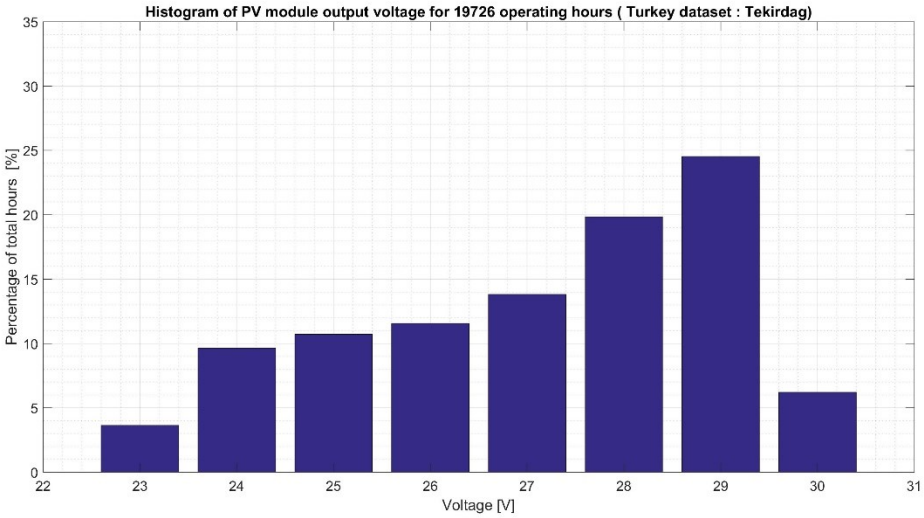


OUTPUT VOLTAGE HISTOGRAM FOR CITY OF KONYA

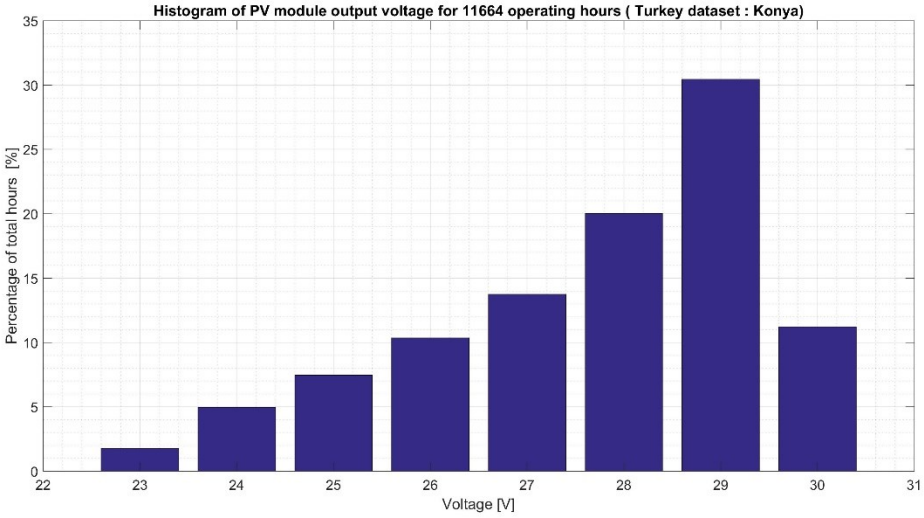

OUTPUT VOLTAGE HISTOGRAM FOR CITY OF BURSA

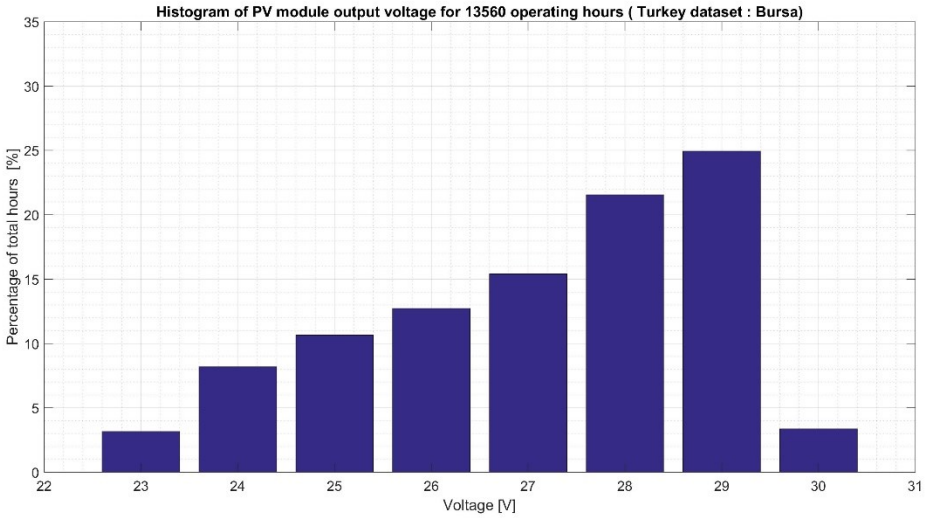


OUTPUT VOLTAGE HISTOGRAM FOR CITY OF AFYONKARAHISAR

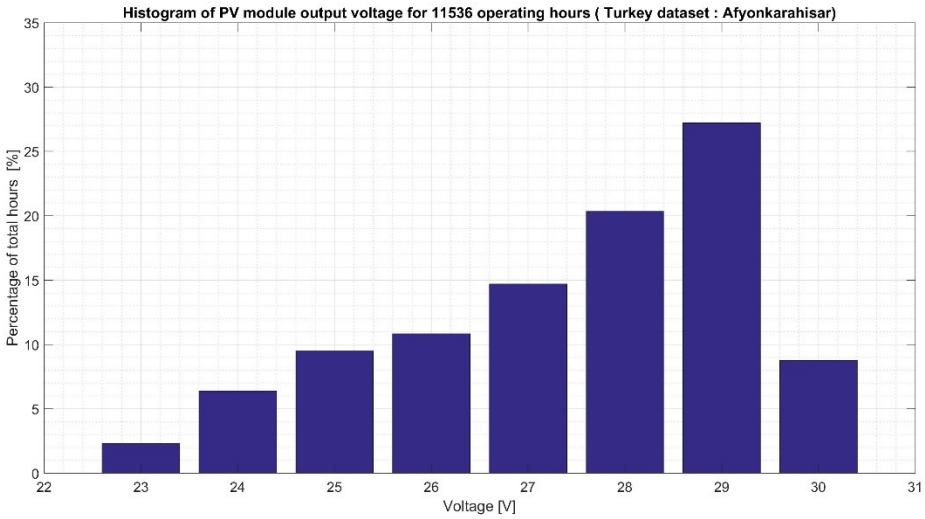

OUTPUT VOLTAGE HISTOGRAM FOR CITY OF NIGDE